JAERI-Research
2002-031

STUDY OF ULTRA-HIGH GRADIENT WAKEFIELD EXCITATION BY INTENSE ULTRASHORT LASER PULSES IN PLASMA

December 2002

Hideyuki KOTAKI

日本原子力研究所
Japan Atomic Energy Research Institute

本レポートは，日本原子力研究所が不定期に公刊している研究報告書です。
入手の問合わせは，日本原子力研究所研究情報部研究情報課（〒319－1195 茨城県那珂郡東海村）あて，お申し越しください。なお，このほかに財団法人原子力弘済会資料センター（〒319－1195 茨城県那珂郡東海村日本原子力研究所内）で複写による実費頒布をおこなっております。

This report is issued irregularly.
Inquiries about availability of the reports should be addressed to Research Information Division, Department of Intellectual Resources, Japan Atomic Energy Research Institute, Tokai-mura, Naka-gun, Ibaraki-ken 〒319－1195, Japan.

編集兼発行　日本原子力研究所

JAERI-Research 2002-031

Study of Ultra-high Gradient Wakefield Excitation by Intense Ultrashort Laser Pulses in Plasma

Hideyuki KOTAKI

Advanced Photon Research Center
Kansai Research Establishment
Japan Atomic Energy Research Institute
Kizu-cho, Souraku-gun, Kyoto

(Received October 11, 2002)

We investigate a mechanism of nonlinear phenomena in laser-plasma interaction, a laser wakefield excited by intense laser pulses, and the possibility of generating an intense bright electron source by an intense laser pulse. We need to understand and further employ some of these phenomena for our purposes. We measure self-focusing, filamentation, and the anomalous blueshift of the laser pulse. The ionization of gas with the self-focusing causes a broad continuous spectrum with blueshift. The normal blueshift depends on the laser intensity and the plasma density. We, however, have found different phenomenon. The laser spectrum shifts to fixed wavelength independent of the laser power and gas pressure above some critical power. We call the phenomenon "anomalous blueshift". The results are explained by the formation of filaments.

An intense laser pulse can excite a laser wakefield in plasma. The coherent wakefield excited by 2 TW, 50 fs laser pulses in a gas-jet plasma around 10^{18} cm^{-3} is measured with a time-resolved frequency domain interferometer (FDI). The density distribution of the helium gas is measured with a time-resolved Mach-Zehnder interferometer to search for the optimum laser focus position and timing in the gas-jet. The results show an accelerating wakefield excitation of 20 GeV/m with good coherency, which is useful for ultrahigh gradient particle acceleration in a compact system. This is the first time-resolved measurement of laser wakefield excitation in a gas-jet plasma. The experimental results are compared with a Particle-in-Cell (PIC) simulation.

The pump-probe interferometer system of FDI and the anomalous blueshift will be modified to the optical injection system as a relativistic electron beam injector. In 1D PIC simulation we obtain the results of high quality intense electron beam acceleration. These results illuminate the possibility of a high energy and a high quality electron beam acceleration.

Keywords : Laser-plasma Interaction, Wakefield, Anomalous Blueshift, Gas-jet,

Frequency Domain Interferometer, Electron Beam Injector

高強度超短パルスレーザーによる、プラズマ中のウェーク場励起に関する研究

日本原子力研究所関西研究所光量子科学研究センター
小瀧　秀行

(2002年10月11日受理)

レーザープラズマ相互作用の非線形現象、高強度レーザーによるウェーク場励起および高ピーク電流電子発生の可能性について調べた。目的達成のためには、これらの現象を理解していく必要がある。我々は、高強度レーザーの自己集束、フィラメント化、異常ブルーシフトについて調べた。自己集束をともなってのガスのイオン化によって、広い連続波長のブルーシフトが起こる。この通常ブルーシフトは、レーザー強度、プラズマ密度に依存する。しかし、これとは違う、レーザーのスペクトルがレーザー強度やプラズマ密度に無関係に一定の波長にシフトする現象を発見した。この現象を我々は「異常ブルーシフト」と呼んだ。

高強度レーザーはプラズマ中にウェーク場を励起する。2 TW, 50 fsのレーザーにより励起した密度10^{18} cm^{-3}付近のガスジェットプラズマ中のウェーク場の時間分解周波数干渉測定を行った。ヘリウムガスの密度分布は、マッハ-ツェンダー干渉計によって測定し、空間的および時間的に最適な場所を探し出した。このウェーク場の測定により、20 GeV/mという高エネルギー加速のための高いウェーク場が観測された。これは、ガスジェットプラズマ中のウェーク場の測定に初めて成功した結果である。シミュレーションとも比較し、一致した。

周波数干渉計によるポンプ-プローブシステムと異常ブルーシフトは、高エネルギー電子ビームのインジェクターとしてのオプティカルインジェクションに成り得る。1次元の粒子シミュレーションにより、高品質電子ビーム加速の結果を得、これによりレーザーウェーク場による、高品質高エネルギー電子加速の可能性を示すことができた。

関西研究所：〒619-0215 京都府相楽郡木津町梅美台8-1

Contents

目次

1. Introduction

Ultrashort intense laser pulses[1]-[4] have opened a new frontier of science so called high field physics. In particular, interactions of intense laser pulses with plasma manifest a large number of nonlinear optical phenomena; optical field ionization (OFI)[5][6], spectral frequency shifts[7]-[14], self-focusing effect[15], higher harmonics generation[16][17], generation of ultrafast X-ray radiation[18]-[20], X-ray lasers[21]-[24], excitation of large amplitude plasma waves[25]-[34] that associate with large electric fields called "laser wakefields", and generation of high energy particles[35]-[38].

Recently laser-driven plasma accelerators using laser wakefields have been conceived to be the next-generation particle accelerators, promising ultrahigh field particle acceleration and compact size compared with conventional accelerators[25]. For this purpose, it is first important to investigate the mechanism of the nonlinear optical phenomena in laser-plasma interactions; OFI, self-channeling, ionization induced spectral shift, and excitation of laser wakefield. These phenomena are deeply related to laser wakefield acceleration of particles. We investigate the laser wakefield excitation and acceleration of bright electron beams due to laser-plasma interactions to clarify the feasibility of a laser wakefield accelerator (LWFA). We present the study of ultra-high gradient wakefield excitation by intense ultrashort laser pulses in plasma according to a diagram as shown in Fig. 1.1.

In chapter 2, the excitation mechanism of wakefields are described. As an intense laser pulse propagates through an underdense plasma, the ponderomotive force expels electrons from the region of the laser pulse. This effect excites wakefields in plasma. The wakefield excitation is described by solving the Maxwell equation and the equation of motion of electrons based on the linear cold fluid model.

In chapter 3, generation of intense laser pulses and measurements of the nonlinear optical phenomena induced laser-plasma interactions are presented. Thanks to the advance of intense ultrashort pulse lasers with a chirped pulse amplification (CPA) technique, in recent years a large number of experiments have been devoted to the studies of the intense laser-matter interactions. OFI and self-focusing are observed in the measurement. Measurements of side and forward scattered radiations indicate self-channeling that causes filamentation and a long propagation of the intense laser pulse. The gradient of a refractive index in an ionization front causes a spectral frequency shift of the short pulse laser[15]-[10]. The spectral blueshift has been observed experimentally in the propagation of intense ultrashort laser pulses through a gas medium[11]-[14]. This generic blueshift strongly depends on the laser intensity and the gas density. In our experiments, a different type of blueshift has been discovered. In this blueshift, a whole spectrum of the laser pulse shifts to a fixed value without regard to the laser intensity and the gas density. We call this effect an "anomalous blueshift". We present a physical interpretation of this puzzling effect.

In chapter 4, the gas density measurements of the neutral gas and the laser wakefield measurement are presented. The gas-jet has been used for many applications to supply a plasma source in the vacuum chamber[39]-[42]. Since a gas adiabatically expands through a nozzle at a sound speed, the density distribution changes in space and time at the same rate as the sound velocity of the gas. Therefore it is necessary to measure the time-dependent spatial distribution of gas density for controlling the plasma precisely. For this purpose, we have made a time-resolved measurement of the gas density distribution produced by the gas-jet. These results visualize dynamics of a neutral gas ejected from the gas-jet nozzle.

Following the gas density measurements, a direct measurement of the plasma density oscillation can be performed by means of the ultrafast time-resolved frequency domain interferometry (FDI)[43]. The FDI measurement is based on the pump-probe technique consisting of an intense ultrafast pump pulse and two ultrafast probe laser pulses. In FDI, the plasma electron density oscillations excited

by the pump pulse can be detected as a phase shift of the frequency domain interferogram in the spectrum produced by two probe pulses. The measurement of the phase shift as a function of time gives direct information of the amplitude and phase of the wakefields. Several measurements have been made with FDI to demonstrate wakefield excitation by ultrashort laser pulses in an underdense plasma[33][34][44]-[46]. These measurements have been done for a relatively low density plasma in a gas filled chamber using laser pulse durations around 100 fs and pump peak powers less than 1 TW. In these measurements the probe pulse width limits the highest measurable density to $\sim 4 \times 10^{17}$ cm^{-3}, and the pump pulses were tightly focused to enhance the plasma wave excitation due to 2D effects. In the 2D dominant regime, where the pulse width is longer than the spot size, the radial wakefield is higher than the longitudinal one. Therefore a shorter pulse is preferable to generate a more 1D coherent planar wakefield at the higher resonant plasma density. The measurement of laser wakefields has been made in less 2D dominant regime[47]. The measured wakefield is compared with 1D Particle-in-Cell (PIC) simulation results.

In chapter 5, we present the application of the laser wakefield excitation to electron beam acceleration with a small emittance and a small energy spread. We make a numerical simulation of electron beam acceleration for parameters based on our experimental results ; i.e. the anomalous blueshift effect and the laser wakefield measurements.

The LWFA has been experimentally demonstrated and has great potential to produce ultrahigh field gradients of the order of $\sim$ 100 GeV/m[26]-[34]. The maximum energy gain has exceeded 100 MeV with an energy spread of $\sim$ 100% due to dephasing and wave-breaking effects in the self-modulated LWFA regime, where thermal plasma electrons are accelerated[32]. The highest energy gain acceleration which exceeded 200 MeV was observed with the injection of an electron beam at an energy matched to the wakefield phase velocity in a fairly underdense plasma[33][34].

Hence, from the point of view of applications for particle accelerators, it is crucial that an ultrashort particle bunch with an energy higher than the trapping threshold should be injected with respect to the correct acceleration phase of the wakefield to produce a high quality beam with small momentum spread and good pulse-to-pulse energy stability. The trapped phase space of the wakefield accelerations are typically less than 100 fs temporally and 10 μm spatially, respectively. Therefore it is essential to inject a very short pulse and a low emittance electron beam into the wakefield. Electron beam injection triggered by an intense ultrashort laser is proposed to an injector of ultrashort electron beams as "optical injection"[35]-[38]. We present the numerical simulation an optical injection scheme based on the FDI system and the anomalous blueshift.

In conclusion we have investigated the extraordinary nonlinear phenomena manifested via interactions of intense ultrashort laser pulses with gas and plasma; optical field ionization, ionization induced self-focusing and filamentation, an anomalous spectral shift and a large amplitude wakefield excitation. On the basis of direct observations of ultrafast phenomena from different aspects, this thesis reveals that these phenomena occur in a consecutive strong field process through mutually correlated mechanism generated above a certain threshold intensity and that they can be controlled with femtosecond optical pulse technique in order to generate a relativistic bright electron beam with high quality in a laboratory table-top scale. A consecutive process of nonlinear phenomena is initiated by direct optical field ionization of gaseous matter due to interaction between an atomic bound Coulomb field and a strong laser field in a non-perturbed quantum regime as well as the self-focusing effect caused by a generic nonlinear optical property of medium. This ultrafast ionization through the OFI mechanism creates plasma in the duration of laser pulse, which has completely deferent optical and dynamic properties compared with a neutral gas state. The ultrafast refractive index change strongly affects propagation of laser pulses to cause a complex filamentation and a spectral blueshift of coherent radiation. The fast electro dynamic motion of plasma electrons excites large amplitude coherent wakefields in plasma due to ponderomotive force of intense laser pulses.

In this thesis we present particular observations of nonlinear optical phenomena related to ionization induced self-focusing with filamentation and anomalous spectral blueshift. The anomalous

blueshift is a puzzling phenomenon that shows a coherent frequency upshift of the whole laser pulse to a fixed frequency independent of the plasma density and the laser power. We clarify that this phenomenon results from a complex mechanism of the ultrafast optical field ionization and filamentation to cause acceleration of the whole laser photons due to a steep gradient of the refractive index change from neutral gas to plasma. The thesis is focused on wakefield excitation driven by a ponderomotive force of intense ultrashort pulse lasers, of which tremendous recent progress has demonstrated generation and acceleration of relativistic particle beams. Reported is the first direct measurement of coherent excitation of ultrahigh gradient wakefields of 20 GeV/m in a gas jet plasma, made by using the pump-probe femtosecond time-resolved diagnostic on plasma density as well as precise measurements of gas density distribution. In the numerical simulations based on the results of these measurements, we confirm generation of a relativistic electron beam accelerated by laser wakefields to be optically controlled with two colliding injection pulses of which one pulse can utilize a frequency up-shifted pulse due to the anomalous blueshift effect. We propose a design of all-laser-based particle accelerator capable of producing a high quality relativistic electron beam with a small emittance and a narrow energy spread. This synthetic study on laser wakefield excitation illuminates physical mechanisms of complex ultrafast nonlinear phenomena generated by interaction of ultraintense laser pulses with plasma and gives prospects for the development of next generation particle accelerators based on laser wakefield acceleration concept.

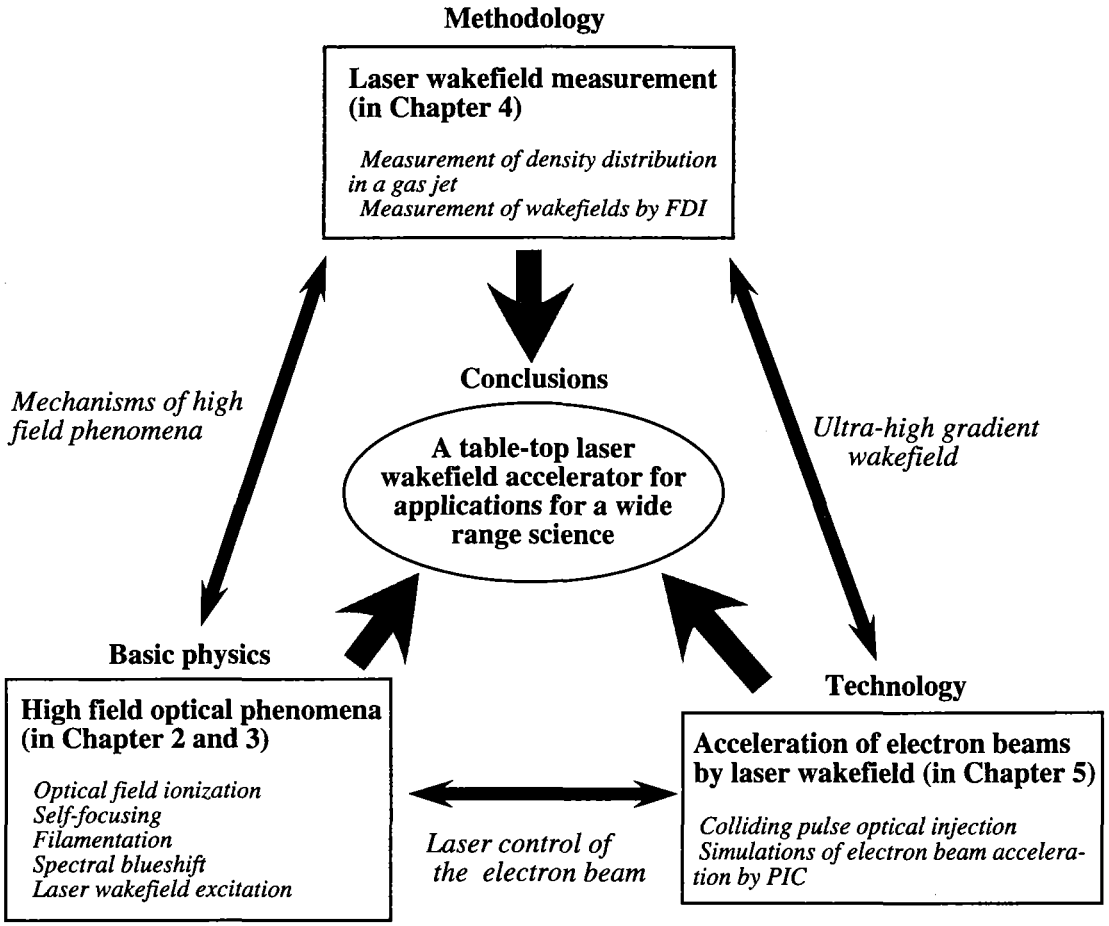

Figure 1.1: A configuration of the dissertation research.

2. Laser Wakefield Excitation by an Intense Laser Pulse

2.1 Laser Strength Parameter

The laser fields are expressed in term of the vector potential $\mathbf{A}$, which in turn is expressed in the dimensionless form $\mathbf{a_0} = e\mathbf{A}/m_e c^2$, and we assume the condition $\nabla \cdot \mathbf{A} = 0$; where c is the speed of light, m_e is the rest mass of the electron and e is the electron charge. When $\mathbf{A}$ is a plane wave for the function of $\exp(i\omega_0 t)$, the laser strength parameter a_0 is

$$a_0 = \frac{eE_L}{m_e c^2 k_0}, \tag{2.1}$$

where ω_0 and k_0 are the frequency and the wave number of the laser, and E_L is electric field of the laser. For the resistance Ω_0 in vacuum of 377 Ω and the relation of potential $E_L = \sqrt{2\Omega_0 I}$ in a linear polarization, the equation (2.1) is rewritten by

$$a_0 = \frac{e\lambda_0\sqrt{\Omega_0 I}}{\sqrt{2}\pi m_e c^2} = 8.5 \times 10^{-10}\lambda_0[\mu\mathrm{m}]\sqrt{I[\mathrm{W/cm^2}]}, \tag{2.2}$$

where λ_0 is the wavelength of the laser and I is the laser intensity. The laser electric field E_L is given by

$$E_L[\mathrm{TV/m}] = \frac{m_e c^2 k_0}{e} a_0 = 2.7 \times 10^{-9}\sqrt{I[\mathrm{W/cm^2}]}. \tag{2.3}$$

2.2 Ponderomotive Force in Pasma

The equation of motion of an electron in the electric field of the laser is

$$m_e \frac{d\mathbf{v}}{dt} = e(\mathbf{E} + \mathbf{v} \times \mathbf{B}), \tag{2.4}$$

where B is the magnetic field of the laser. We assume the electric field $\mathbf{E}$ is

$$\mathbf{E} = \mathbf{E_s}\cos(\omega_0 t). \tag{2.5}$$

The position vector $\mathbf{r}$ is expanded as $\mathbf{r} = \mathbf{r_0} + \delta\mathbf{r_1} + \delta\mathbf{r_2} + \cdots$, where $\delta\mathbf{r_1}$ and $\delta\mathbf{r_2}$ are due to first and second order perturbations, respectively. The velocity and the electric field are

$$\mathbf{v} = \frac{d\mathbf{r}}{dt} = \frac{d\delta\mathbf{r_1}}{dt} + \frac{d\delta\mathbf{r_2}}{dt} + \cdots = \mathbf{v_0} + \mathbf{v_1} + \mathbf{v_2} + \cdots, \tag{2.6}$$

$$\mathbf{E} = \mathbf{E}|_{r=r_0} + (\delta\mathbf{r_1} \cdot \nabla)\mathbf{E}|_{r=r_0} + \cdots = \mathbf{E_1} + \mathbf{E_2} + \cdots, \tag{2.7}$$

To first order, $\mathbf{v} \times \mathbf{B}$ is 0 in Eq. (2.4).

$$m_e \frac{d\mathbf{v_1}}{dt} = e\mathbf{E}|_{r=r_0} = eE_s\cos(\omega_0 t), \tag{2.8}$$

From the integral of Eq. (2.8), $\mathbf{v_1}$ and $\delta\mathbf{r_1}$ are given by

$$\mathbf{v_1} = \frac{e}{m_e\omega_0} E_s \sin(\omega_0 t), \tag{2.9}$$

$$\delta \mathbf{r_1} = -\frac{e}{m_e \omega_0^2} E_s \cos(\omega_0 t). \tag{2.10}$$

No longitudinal wave is generated to first order for the side wave of the laser pulse. The equation of motion to second order we have

$$m_e \frac{d\mathbf{v_2}}{dt} = e[(\delta \mathbf{r_1} \cdot \nabla)\mathbf{E}|_{r=r_0} + \mathbf{v_1} \times \mathbf{B_1}]. \tag{2.11}$$

B_1 can be calculated from the Maxwell equation $\nabla \times \mathbf{E} = -d\mathbf{B}/dt$.

$$\mathbf{B_1} = -\frac{1}{\omega_0} \nabla \times \mathbf{E_s}|_{r=r_0} \sin(\omega_0 t). \tag{2.12}$$

The equation of motion is given by

$$m_e \frac{d\mathbf{v_2}}{dt} = \frac{e^2}{m_e \omega_0^2} [\cos^2(\omega_0 t)(\mathbf{E_s} \cdot \nabla) E_s + \sin^2(\omega_0 t) \mathbf{E_s} \times (\nabla \times \mathbf{E_s})]. \tag{2.13}$$

For the average of time $\langle \sin^2(\omega_0 t) \rangle = \langle \cos^2(\omega_0 t) \rangle = 1/2$, the equation of motion is

$$m_e \langle \frac{d\mathbf{v_2}}{dt} \rangle = \frac{e^2}{2m_e \omega_0^2} [(\mathbf{E_s} \cdot \nabla)\mathbf{E_s} + \mathbf{E_s} \times (\nabla \times)\mathbf{E_s}] = \frac{e^2}{2m_e \omega_0^2} \nabla \langle E_s^2 \rangle. \tag{2.14}$$

The right side of the equation of motion to second order shows the ponderomotive potential. For $E_s^2 = 2\langle E^2 \rangle$, the ponderomotive force $\mathbf{f_{pond}}$ is

$$\mathbf{f_{pond}} = \frac{e^2}{m_e \omega_0^2} \nabla \langle E^2 \rangle. \tag{2.15}$$

We introduce the relation of $f_{pond} = -e\nabla\phi_{pond}$. For the electric field in Eq. (2.15) of the averaged one, the ponderomotive potential is given by

$$\phi_{pond} = -\frac{m_e c^2}{2e} a^2. \tag{2.16}$$

2.3 Laser Wakefield Excited by an Intense Laser Pulse

Plasma provides some advantages as an accelerating medium in laser-driven accelerators. Plasma can sustain ultrahigh electric fields as well as optically guide the laser beam and the particle beam under appropriate conditions. For a nonrelativistic plasma wave, the acceleration gradients are limited to the order of the wave-breaking field E_0 given by

$$E_0[\mathrm{eV/cm}] = m_e c \omega_p \simeq 0.96 n_e^{1/2} [\mathrm{cm}^{-3}], \tag{2.17}$$

where $\omega_p = (4\pi n_e e^2/m_e)^{1/2}$ is the electron plasma frequency and n_e is the ambient electron plasma density. It means that a plasma density of $n_e = 10^{18}$ cm^{-3} can sustain an acceleration gradient of 100 GeV/m.

As an intense laser pulse propagates through an underdense plasma, the ponderomotive force expels electrons from the region of the laser pulse. This effect excites a large amplitude plasma wave (wakefield) with a phase velocity approximately equal to the group velocity of laser pulse, given by $v_p = c(1 - \omega_p^2/\omega_0^2)^{-1/2}$, where ω_0 is the laser frequency. Figure 2.1 presents an overview of the laser wakefield excitation. An intense laser pulse creating plasma and subsequently exciting

a longitudinal plasma oscillation. The electron motion in plasma is calculated by solving the cold fluid equation, the equation of continuity and Poisson's equation.

$$m_e \frac{d\mathbf{v}}{dt} = e(\mathbf{E} + \mathbf{v} \times \mathbf{B}), \tag{2.18}$$

$$\frac{\partial n_e}{\partial t} + \nabla \cdot \mathbf{v} = 0, \tag{2.19}$$

$$\nabla^2 \Phi = 4\pi e n_e, \tag{2.20}$$

where $\mathbf{v}$ is the electron velocity, Φ is the potential and ϵ_0 is the dielectric constant in vacuum. The perturbative expansions of $\mathbf{v}$、 n、 Φ are performed for $|a_0| < 1$. The first order motion is just the quiver motion of the electrons. The perturbative solution of Eqs. (2.18)-(2.20), to second order we have

$$m_e \frac{d\delta\mathbf{v}}{dt} = e(\delta\phi + \phi_{pond}), \tag{2.21}$$

$$\frac{\partial \delta n_e}{\partial t} + \nabla \cdot \delta\mathbf{v} = 0, \tag{2.22}$$

$$\nabla^2 \delta\phi = 4\pi e \delta n_e, \tag{2.23}$$

where $\delta\mathbf{v}$ is the electron velocity of second order, δn_e is the electron density of second order, $\delta\phi$ is the potential of second order and ϕ_{pond} is the ponderomotive potential(Eq. (2.16)). The second order equations for δn_e, $\delta\phi$ and $\delta\mathbf{v}$ are

$$\left(\frac{\partial^2}{\partial t^2} + \omega_p^2\right) \delta n_e = -\frac{\omega_p^2}{4\pi e} \nabla^2 \phi_{pond}, \tag{2.24}$$

$$\left(\frac{\partial^2}{\partial t^2} + \omega_p^2\right) \delta\phi = -\omega_p^2 \phi_{pond}, \tag{2.25}$$

$$\left(\frac{\partial^2}{\partial t^2} + \omega_p^2\right) \delta\mathbf{v} = \frac{e}{m} \frac{\partial}{\partial t} \nabla \phi_{pond}. \tag{2.26}$$

The general solution to these linearized from a convolution, nonrelativistic 2D fluid equations has been given by

$$\delta\phi(r,\zeta) = k_p \int_\zeta^\infty \sin[k_p(\zeta - \zeta')] \phi_{pond}(r,\zeta') d\zeta', \tag{2.27}$$

where, $\zeta = z - v_p t$ is the longitudinal speed-of-light-frame coordinate, $k_p = \omega_p / c$ is the wave number of the plasma. The electron density perturbation is rewritten by

$$\delta n_e = -\frac{1}{4\pi e} \Delta \delta\phi = -\frac{1}{4\pi e} \left(\frac{\partial^2}{\partial z^2} + \frac{1}{r} \frac{\partial}{\partial r} r \frac{\partial}{\partial r}\right) \delta\phi, \tag{2.28}$$

and

$$\begin{aligned} \frac{\delta n_e}{n_e} &= \frac{a^2(r,\zeta)}{2} + \frac{k_p}{2} \int_\zeta^\infty \sin[k_p(\zeta - \zeta')] a^2(r,\zeta) d\zeta' \\ &\quad - \frac{1}{k_p} \int_\zeta^\infty \sin[k_p(\zeta - \zeta')] \left[\frac{1}{r} \frac{\partial}{\partial r} r \frac{\partial}{\partial r} \frac{a^2(r,\zeta)}{2}\right] d\zeta'. \end{aligned} \tag{2.29}$$

We make an assumption that the laser pulse is a Gaussian beam in the radial direction and $f(\zeta)$ in the longitudinal direction as

$$a(r,\zeta) = a_0 \, f(\zeta) \exp\left(-\frac{r^2}{2\sigma_r^2}\right), \tag{2.30}$$

where σ_r is the rms-width of the laser pulse in the radial direction. The electron density perturbation is given by

$$\begin{aligned}\frac{\delta n_e}{n_e} &= \frac{a^2(r,\zeta)}{2} \\ &+k_p\frac{a_0^2}{2}\exp\left(-\frac{r^2}{\sigma_r^2}\right)\left[1+\frac{4}{k_p^2\sigma_r^2}\left(1-\frac{r^2}{\sigma_r^2}\right)\right] \\ &\times\int_\zeta^\infty g(\zeta')\sin[k_p(\zeta-\zeta')]d\zeta',\end{aligned} \tag{2.31}$$

where $g(\zeta)=f^2(\zeta)$. The laser pulse $a(r,\zeta)$ and $g(\zeta)$ become 0 for the localization of the laser pulse when $\zeta\to-\infty$.

$$\int_{-\infty}^\infty g(\zeta')\sin[k_p(\zeta-\zeta')]d\zeta' = A\sin(k_p\zeta+\delta), \tag{2.32}$$

$$\int_{-\infty}^\infty g(\zeta')\cos[k_p(\zeta-\zeta')]d\zeta' = A\sin(k_p\zeta-\delta), \tag{2.33}$$

$$A^2=\left[\int_{-\infty}^\infty g(\zeta')\cos(k_p\zeta')d\zeta'\right]^2+\left[\int_{-\infty}^\infty g(\zeta')\sin(k_p\zeta')d\zeta'\right]^2, \tag{2.34}$$

$$tan\ \delta=\left[\int_{-\infty}^\infty g(\zeta')\cos(k_p\zeta')d\zeta'\right]/\left[\int_{-\infty}^\infty g(\zeta')\sin(k_p\zeta')d\zeta'\right]. \tag{2.35}$$

A is rewritten by a Fourier transform $\mathcal{F}$

$$A^2=|\mathcal{F}\{g(\zeta)\}|^2. \tag{2.36}$$

It should be noted that A can be uniquely obtained in the laboratory from the 2nd order background free autocorrelation of the laser pulse. The electron density perturbation is given by

$$\frac{\delta n_e}{n_e}=\frac{k_pa_0^2}{2}\exp\left(-\frac{r^2}{\sigma_r^2}\right)\left[1+\frac{4}{k_p^2\sigma_r^2}\left(1-\frac{r^2}{\sigma_r^2}\right)\right]\ A\ \sin(\omega_pt+\delta). \tag{2.37}$$

The longitudinal and radial electric fields can also be obtained from Eq. (2.27)

$$\mathbf{E}=-\nabla\delta\phi, \tag{2.38}$$

$$eE_z(r,\zeta)=e\frac{\partial}{\partial z}\delta\phi=\frac{m_ec^2k_p^2a_0^2}{2}\ \exp\left(-\frac{r^2}{\sigma_r^2}\right)\ A\ \cos(\omega_pt-\delta), \tag{2.39}$$

$$eE_r(r,\zeta)=e\frac{\partial}{\partial r}\delta\phi=-\frac{m_ec^2k_pa_0^2r}{\sigma_r^2}\ \exp\left(-\frac{r^2}{\sigma_r^2}\right)\ A\ \sin(\omega_pt+\delta). \tag{2.40}$$

Here, we make an assumption that the laser pulse is also a Gaussian beam in the longitudinal direction as $f(\zeta)=\exp(-\zeta^2/2\sigma_z^2)$, where σ_z is the rms-widths of the laser pulse in the longitudinal direction. The electron density perturbation, the longitudinal electric field and the radial electric field in the linear regime are rewritten from Eqs. (2.37), (2.39) and (2.40)

$$A=\sqrt{\pi}\sigma_z\exp\left(-\frac{k_p^2\sigma_z^2}{4}\right), \tag{2.41}$$

$$\frac{\delta n_e}{n_e}=\frac{\sqrt{\pi}k_p\sigma_za_0^2}{2}\left[1+\frac{4}{k_p^2\sigma_r^2}\left(1-\frac{r^2}{\sigma_r^2}\right)\right]\exp\left(-\frac{r^2}{\sigma_r^2}-\frac{k_p^2\sigma_z^2}{4}\right)\ \sin(k_p\zeta), \tag{2.42}$$

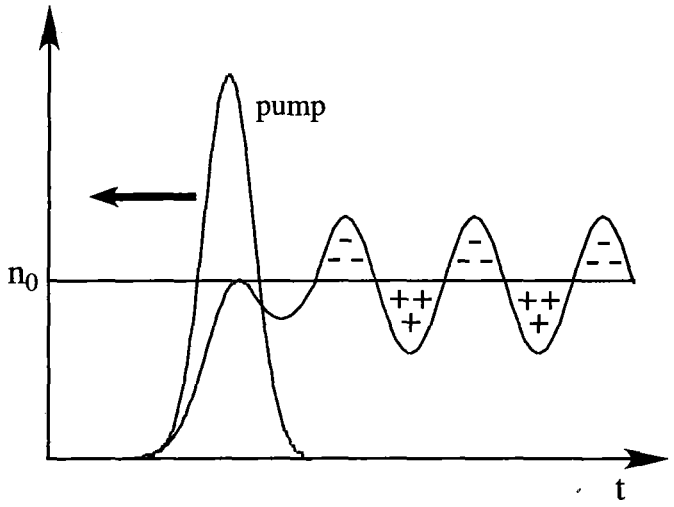

Figure 2.1: An intense laser pulse creating plasma and subsequently exciting a longitudinal plasma oscillation. The horizontal axis, denoted t in the figure, is in a frame moving with the laser pulse and the ionization front/wakefield. The arrow denotes the direction of propagation.

$$eE_z(r,\zeta) = \frac{\sqrt{\pi} m_e c^2 k_p^2 \sigma_z a_0^2}{2} \exp\left(-\frac{r^2}{\sigma_r^2} - \frac{k_p^2 \sigma_z^2}{4}\right) \cos(k_p \zeta), \tag{2.43}$$

$$eE_r(r,\zeta) = -\frac{\sqrt{\pi} m_e c^2 k_p \sigma_z a_0^2 r}{\sigma_r^2} \exp\left(-\frac{r^2}{\sigma_r^2} - \frac{k_p^2 \sigma_z^2}{4}\right) \sin(k_p \zeta). \tag{2.44}$$

The normalized electric fields are shown in Fig. 2.2. The figure indicates that the electron beam is accelerated in the phase of $\pi/2$ to $3\pi/2$, and the electron beam is focused in the phase of π to 2π. In order to accelerate the electron beam, the electron beam has to be injected in the phase of π to $3\pi/2$. Figure 2.3 shows the electric fields excited by a 50 fs laser pulse. The laser strength parameter a_0 is 0.7.

The maximum accelerating gradient is achieved on the propagation axis of the laser pulse at the plasma wavelength $\lambda_p = \pi\sigma_z$ i.e. $(eE_z)_{\max} = 2\sqrt{\pi} e^{-1} m_e c^2 a_0^2/\sigma_z$. The amplitude of the longitudinal wakefield at $r = 0$ is given in terms of the amplitude of the plasma density oscillation as

$$\left(\frac{|eE_z|}{m_e c \omega_p}\right)_{r=0} = \left(\frac{|\delta n_e|}{n_e}\right)_{r=0} \left[1 + \frac{4}{k_p^2 \sigma_r^2}\right]^{-1}, \tag{2.45}$$

This means that measurements of the plasma density oscillation provide a direct mapping of the wakefields excited by laser pulses as long as the wake is coherent in the linear regime.

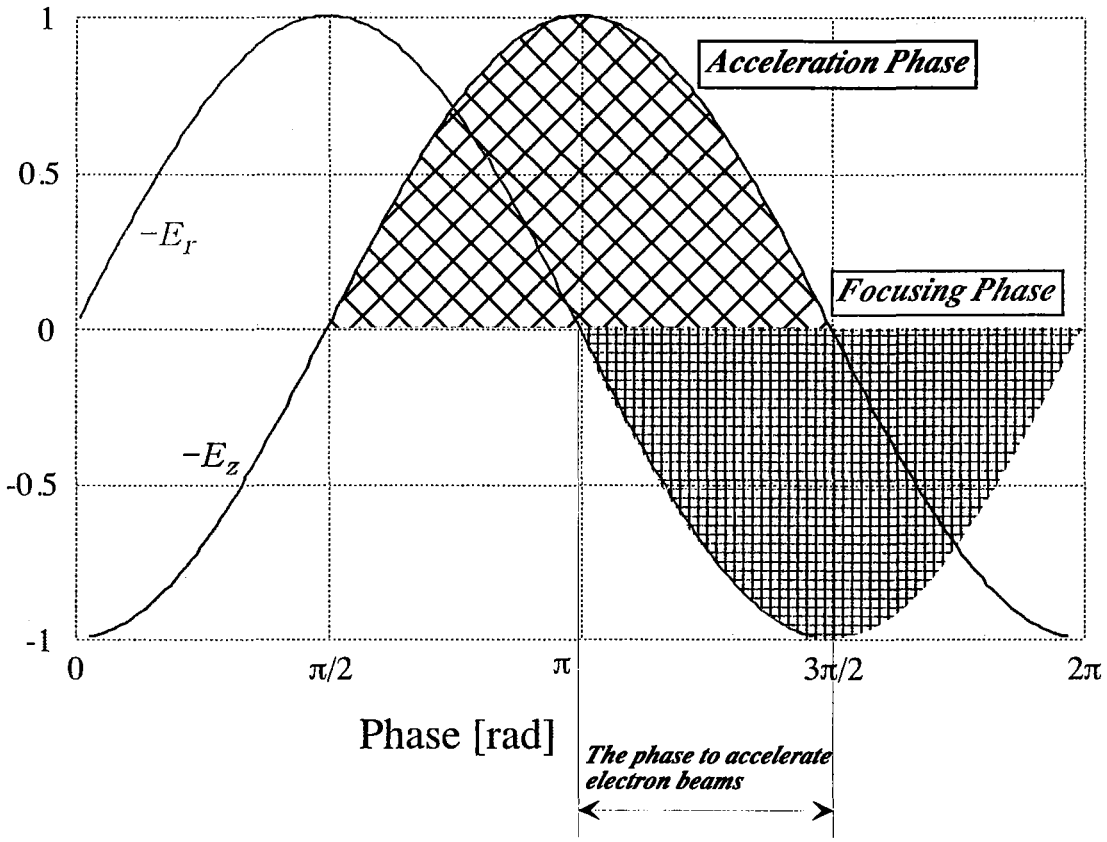

Figure 2.2: The longitudinal electric field and the radial electric field in the linear regime.

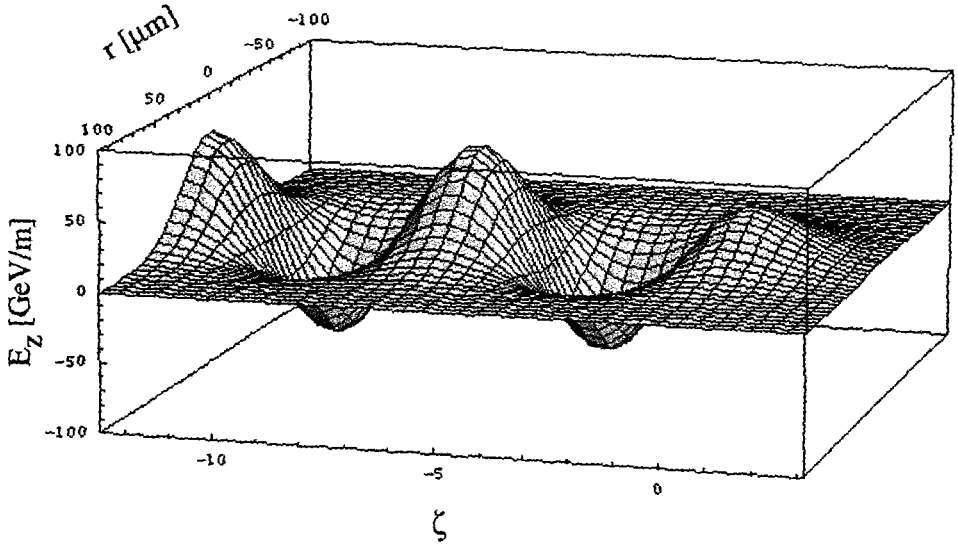

(a)

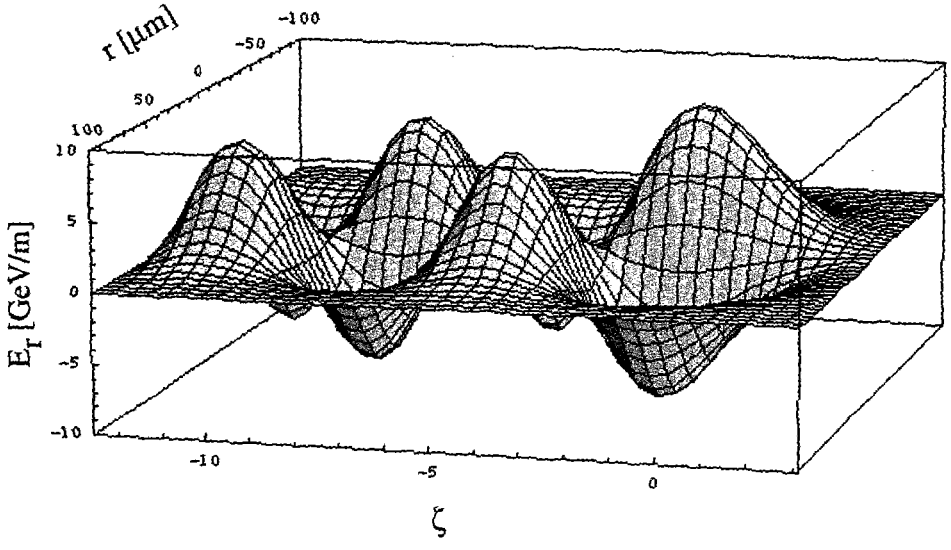

(b)

Figure 2.3: (a) The longitudinal electric field and (b) the radial electric field in the linear regime for the laser pulse width of 50 fs and the laser strength parameter a_0 of 0.7.

3. High Field Optical Phenomena

3.1 Generation of Intense Ultrashort Laser Pulses

The combination of chirped pulse amplification (CPA)[1] and ultra-broadband solid-state laser medium has made it possible to produce multi-terawatt femtosecond pulses. Figure 3.1 shows a schematic of CPA system for an intense ultrashort laser pulse. An ultrashort pulse generated by a mode-locked oscillator is temporally stretched from the femtosecond to the nanosecond regime with an antiparallel diffraction grating pair pulse stretcher to decrease the peak power (see Fig. 3.2(a)). The low-energy and long duration chirped pulse is then amplified to a high energy commensurate with the saturation fluence of the laser amplifiers. For the Ti:sapphire laser, the medium of the laser amplifier is excited by a second harmonics of a Nd:YAG laser at the repetition rate of 10 Hz. The amplified pulse is then compressed to an initial ultrashort pulse of high peak power with a parallel grating pair compressor(see Fig. 3.2(b)). In the experiments of nonlinear optical phenomena, the compressed pulse duration is 90 fs and the maximum pulse energy is 300 mJ at the repetition rate of 10 Hz.

3.2 Ionization of Atoms

At intensities greater than 10^{18} W/cm^2, the field of the laser is much larger than Coulomb field binding the ground state electron in the hydrogen atom, $E_{at} = 5 \times 10^9$ V/cm. At 10^{19} W/cm^2, the laser electric field is close to 10^{11} V/cm, 20 times E_{at}.

The sum of the photon energy over the ionization potential causes multi-photon ionization. When the absorbed photon number is N, the frequency of the light is ω_0 and $N\hbar\omega_0/2\pi > U_i$; $A^{n+} + N\hbar\omega_0/2\pi \rightarrow A^{(n+1)+} + e^-$. When the ionization cross section is σ_i[W^{-N} cm^{2N} s^{-1}], the ionization rate is

$$W = \sigma_i I^N. \tag{3.1}$$

Agostini et al.[48] discovered that the ejected electron could absorb photons in excess of the minimum required for ionization to occur. The study of this excess-photon ionization, known as "above threshold ionization" (ATI), has been one of the central themes of multiphoton physics. Figure 3.3 shows the schematic diagram of energy levels for multiphoton ionization at threshold and above, together with the energy spectrum of the emitted electrons. As the intensity I, peaks at higher energies appear, whose intensity dependence does not follow the lowest order perturbation theory prediction according to which the ionization rate for an N-photon process is proportional to I^N.

Photoionization of materials is determines by the Keldysh tunneling parameter κ[5].

$$\kappa = \omega_0 \frac{\sqrt{2m_e U_i}}{eE_0} = \sqrt{\frac{U_i}{2\phi_p}}, \tag{3.2}$$

where U_i is the ionization potential, ω_0 is the laser frequency, E_0 is the electric field of the laser and ϕ_p is the ponderomotive potential.

$$\phi_p = \frac{e^2 E_0^2}{4m_e\omega^2} = 9.33 \times 10^{-14} I[\mathrm{W/cm^2}]\lambda_0^2[\mu\mathrm{m}]. \tag{3.3}$$

Multi-photon ionization dominates for $\kappa > 1$.

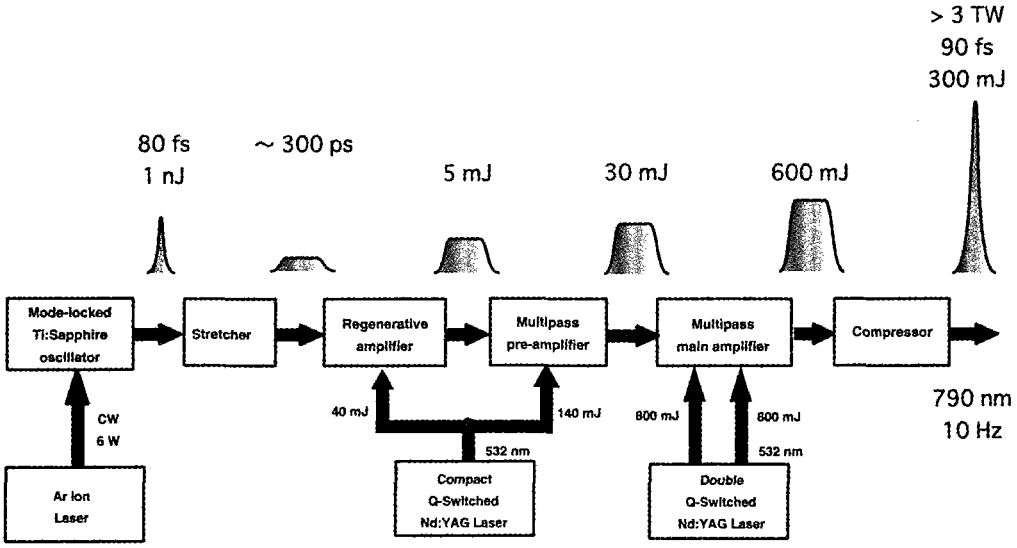

Figure 3.1: A schematic of chirped pulse amplification system used for the blueshift measurement.

Optical field ionization (OFI) causes the electric field of laser for $\kappa < 1$. A schematic of OFI is shown in Fig. 3.4. Figure 3.4(a) shows the tunneling ionization and Figure 3.4(b) shows the barrier suppression ionization. The red lines correspond to the Coulomb potential. The blue lines correspond to the contribution to the potential energy due to the instantaneous laser electric field. The green lines correspond to the total effective potential energy. The characteristic time scale for the electron velocity to change in the atom by the electric field, τ, has to be shorter than the inverse frequency of the laser for direct ionization by the electric field of the laser.

$$\tau = \frac{\sqrt{2m_e U_i}}{eE_0} < \frac{1}{\omega_0}. \tag{3.4}$$

In addition, the electron passes through the potential wall when the Coulomb potential decreases due to the strong electric field of the laser. The Coulomb potential in the electric field is

$$V(x) = -\frac{Ze^2}{x} - eE_0 x. \tag{3.5}$$

The tunneling ionization starts when the potential is same as the ionization potential, the minimum electric field of the tunneling ionization is

$$E_0 = \frac{U_i^2}{4e^3 Z}, \tag{3.6}$$

and the threshold of the laser intensity for tunneling ionization is

$$I_{th}[\mathrm{W/cm^2}] = \frac{cU_i^4}{128\pi e^6 Z^2} = \frac{2.2 \times 10^{15}}{Z^2}\left(\frac{U_i[eV]}{27.21}\right)^4. \tag{3.7}$$

In order to ionize helium gas perfectly, the threshold of the laser intensity is 3.9×10^{16} W/cm^2 for the ionization potential of 78.9 eV.

This is a blank page.

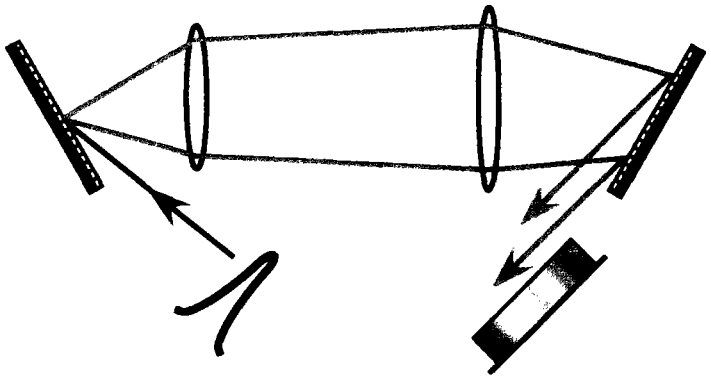

(a)

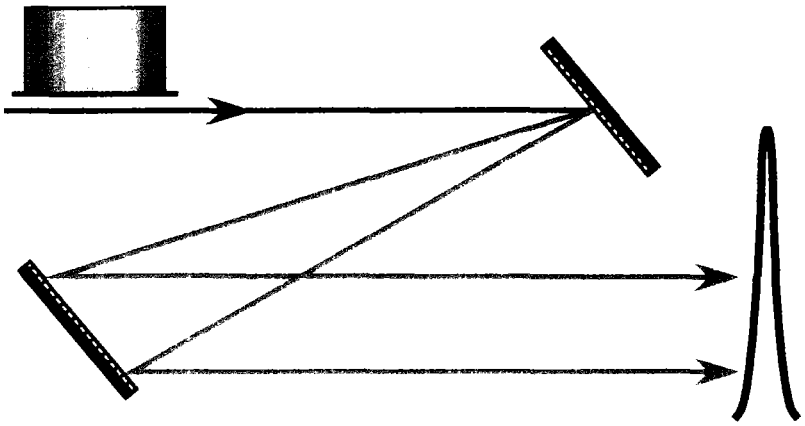

(b)

Figure 3.2: The matched stretcher and compressor. The stretcher (a) is composed of a telescope of magnification 1 two antiparallel diffraction gratings. The compressor (b) is composed of a pair of parallel gratings in which the optical length for the blue is shorter than that for the red.

This is a blank page.

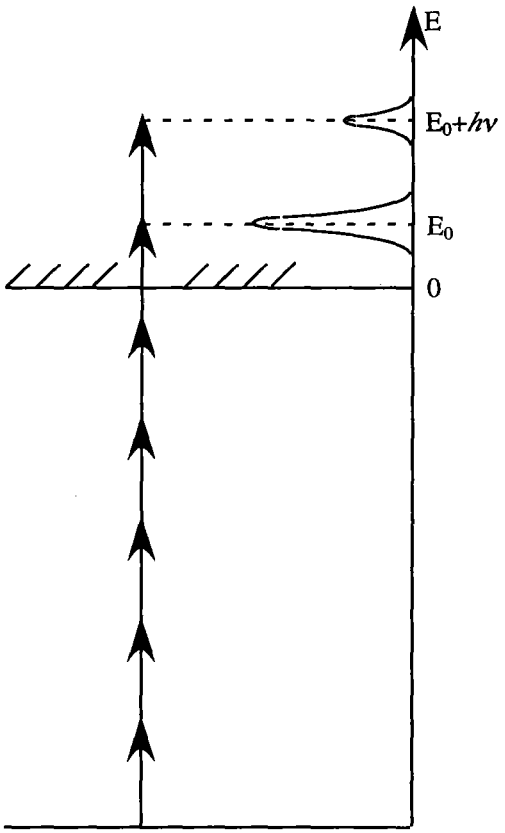

Figure 3.3: A schematic diagram of energy levels for multiphoton ionization at threshold and above, together with the energy spectrum of the emitted electrons.

In our calculations we choose the tunneling formula of Ammosov *et al.*[6] to calculate the OFI rate. The Ammosov *et al.* formula is in better agreement with the experimental data[49]. The ionization rate W is given by

$$W[\mathrm{s}^{-1}] = 1.61\omega_{au}\frac{Z^2}{n_{eff}^{4.5}}\left[10.87\frac{Z^3}{n_{eff}^4}\frac{E_{au}}{E_L}\right]\exp\left[-\frac{2}{3}\frac{Z^3}{n_{eff}^3}\frac{E_{au}}{E_L}\right], \tag{3.8}$$

where ω_{au} of 4.1×10^{16} s^{-1} is the atomic unit of frequency, E_{au} of 0.51 TV/m is the atomic field strength, E_L is the laser electric field, the effective quantum number $n_{eff} = Z/\sqrt{U_i/U_H}$, Z is the charge of the ion, and U_H of 13.6 eV is the hydrogen ionization potential. To obtain estimation for the ionization threshold of gases the barrier suppression ionization model is conveniently used, where the strong external electric field of the laser is superimposed to the Coulomb potential of the atom or ion.

This is a blank page.

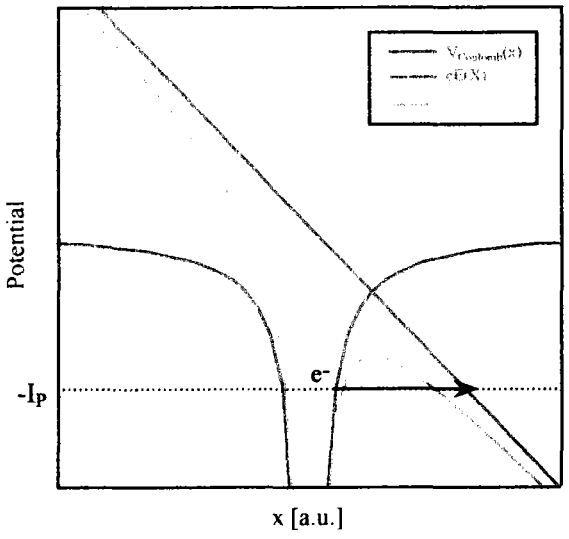

(a)

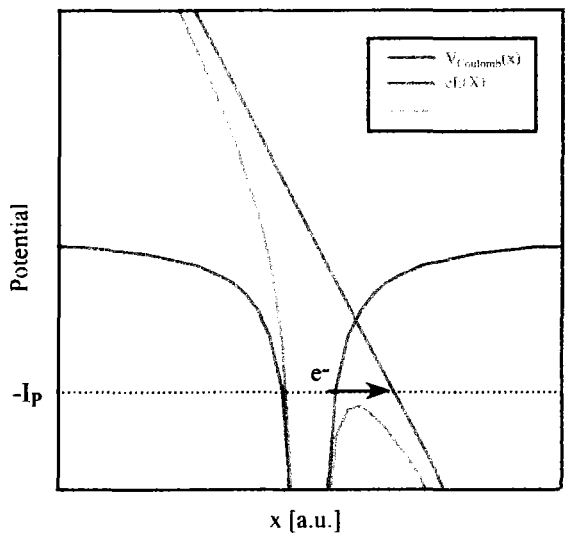

(b)

Figure 3.4: A schematic diagram showing (a) tunneling ionization and (b) barrier suppression ionization. The red lines corresponds to the Coulomb potential. The blue lines corresponds to the contribution to the potential energy due to the instantaneous laser electric field. The green lines corresponds to the total effective potential energy.

This is a blank page.

3.3 Self-focusing of an Intense Laser Pulse

3.3.1 Principle of Self-focusing

Self-focusing occurs due to the nonlinear index of refraction when an intense laser pulse propagates in materials. The refractive index N_g is

$$N_g = N_0 + N_2 I, \tag{3.9}$$

where N_0 is the usual index of refraction, N_2 is the nonlinear index of refraction in units of cm^2/W, and I is the intensity of the laser in units of W/cm^2. For helium gas, the usual refractive index N_{He} is

$$N_{He} = 1 + 35 \times 10^{-6} \times p, \tag{3.10}$$

where p is the gas pressure in units of atm. Using the experimentally determined value for the nonlinear susceptibility $\chi^{(3)} = 2.3 \times 10^{-39}$[esu][50] for helium gas and the formula for the nonlinear index of refraction from the nonlinear susceptibility[51]

$$N_2[\mathrm{cm}^2/\mathrm{W}] = \frac{96\pi^2 n_g}{N_0 c} 10^7 \chi^{(3)}[\mathrm{esu}], \tag{3.11}$$

where n_g is the gas density in cm^{-3}. The refractive index N varies with the laser intensity I. We make an assumption that the laser pulse is a Gaussian beam of which central intensity is stronger than the outerward intensity. The self-focusing results from the light bent toward the part with the high refractive index.

The refractive index of plasma N_e is given by

$$N_e = \sqrt{1 - \frac{n_e}{n_c}}, \tag{3.12}$$

where $n_e[\mathrm{cm}^{-3}] = 2.69 \times 10^{19} \times p$ is the plasma density, $n_c = \pi / r_e \lambda_0^2$ is the critical density, and r_e is the classical electron radius.

It is known that when a laser pulse with sufficient power propagates in a gas, it can self-focus due to the effects of the nonlinear index of refraction of the gas. Figure 3.5 shows a schematic of the self-focusing with filamentation of the intense laser pulse in a gas. The self-focused laser pulse produces plasma. The laser pulse is defocused and makes filaments due to the small refractive index in plasma. Each filament is propagating with intensity near the threshold intensity for the ionization of the gas.

3.3.2 Measurement of Self-focusing and Filamentation

Figure 3.6 shows a schematic of the experimental setup for the measurement of nonlinear laser-plasma phenomena. The maximum pulse power was 2.4 TW with a repetition rate of 10 Hz. The 100 fs laser pulse with an initial spot size of 45 mm was focused using an f/10 off-axis parabolic mirror (OAP) in a gas chamber to a spot size in vacuum of 13 μm with the focal length of 44.3 cm.

Figure 3.7 shows the plasma recombination fluorescence measured by a charge-coupled-device (CCD) camera (see the bottom of Fig. 3.6) using a blue-pass filter with a bandwidth between 410 and 532 nm full width at half maximum (FWHM) for a single laser shot with energy of 165 mJ at helium gas pressures of (a) 1 Torr, (b) 20 Torr, (c) 400 Torr and (d) 760 Torr. The figures on the right side in Fig. 3.7 are lineouts of the corresponding CCD image integrated across the pulse propagation direction. These images are interpreted as approximately representing the plasma density. The exposure time is 100 ms. At 1 Torr the intensity of the scattered radiation increases

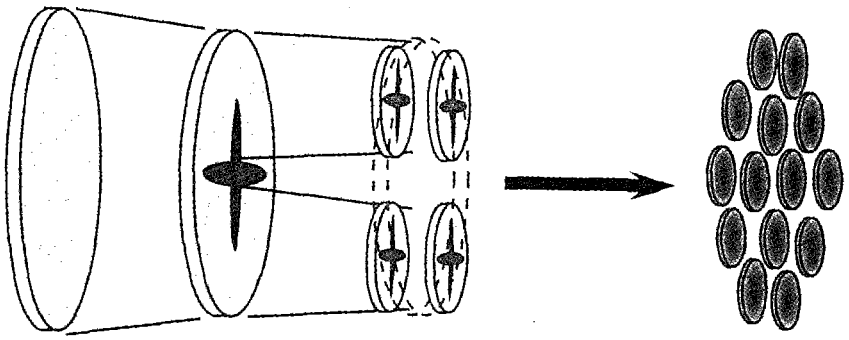

Figure 3.5: A schematic of self-focusing and filamentation of an intense laser pulse in gas.

as the pulse focuses. There is a dip in the intensity at the focus point. This is due to geometric effects since we are observing a line integration of the intensity. At the focus the ionized plasma is narrower. This agrees with the propagation of a Gaussian pulse. Over 20 Torr the dip is not apparent indicating non-Gaussian pulse propagation. Also, the peak intensity is shifted towards the laser injection direction indicating that the focus point of the pulse has moved backwards with increasing the gas pressure.

Figure 3.8 shows the Thomson scattering measured by a CCD camera shown at the bottom of Fig. 3.6 using an interferential filter centered at the laser wavelength of 793 nm with a width of 10 nm FWHM for a single laser shot with energy of 165 mJ for helium gas pressures of 1, 20, 400, and 760 Torr. These images represent the laser intensity multiplied by the plasma density. The figures on the right side in Fig. 3.8 are lineouts of the corresponding CCD image integrated across the pulse propagation direction. The exposure time is 100 ms which corresponds to the time between injected laser pulses. In all the figures the laser propagates from the right to the left. A clear transition can be seen between Fig. 3.8(a) at the pressure of 1 Torr emission and Fig. 3.8(b) at the pressure of 20 Torr emission. In the low pressure case the intensity profile of the scattered radiation smoothly varies from the right to the left at the intensity peak near the focus point. In the higher pressure case spikes in the intensity can be seen. At 20 Torr both spikes and a smoothly varying portion in the light intensity can be seen whereas at 400 and 760 Torr only spikes are observed. In the case of 20 Torr this seems to indicate that some portion of the pulse is self-focused while other parts of the pulse are not.

Figure 3.9 also shows the Thomson scattering measured by a CCD camera using an interferential filter centered at the laser wavelength of 793 nm with a width of 10 nm FWHM for the helium gas pressure of 20 Torr for a single laser shot with energies of 22, 66, and 165 mJ. The intensity of Thomson scattering increases with the laser energy.

Figure 3.10 shows the forward scattered radiation image for the laser energy of 230 mJ at a helium gas pressure of (a) 23 Torr and (b) 760 Torr measured by a CCD camera focused approximately at the vacuum focus point. At the gas pressure of 760 Torr more filaments appear than those at the pressure of 23 Torr. This is a result of the difference of the nonlinear refractive index between 23 Torr and 760 Torr. The number of spikes in Fig. 3.8 and the number of filaments in Fig. 3.10 are correlated. It has been known that filamentation of the laser pulse in the gas can occur[52] for $\mathcal{P} > \mathcal{P}_{cr}$, and that the each filament has a power comparable to $\mathcal{P}_{cr}$. The critical power $\mathcal{P}_{cr}$ at which self-focusing occurs is given by[53]

$$\mathcal{P}_{cr} = \frac{\pi(0.6\lambda_0)^2}{8N_0N_2}. \tag{3.13}$$

where λ_0 is the laser wavelength. The number of filaments is roughly given by $N \simeq \mathcal{P}/\mathcal{P}_{cr}$. The

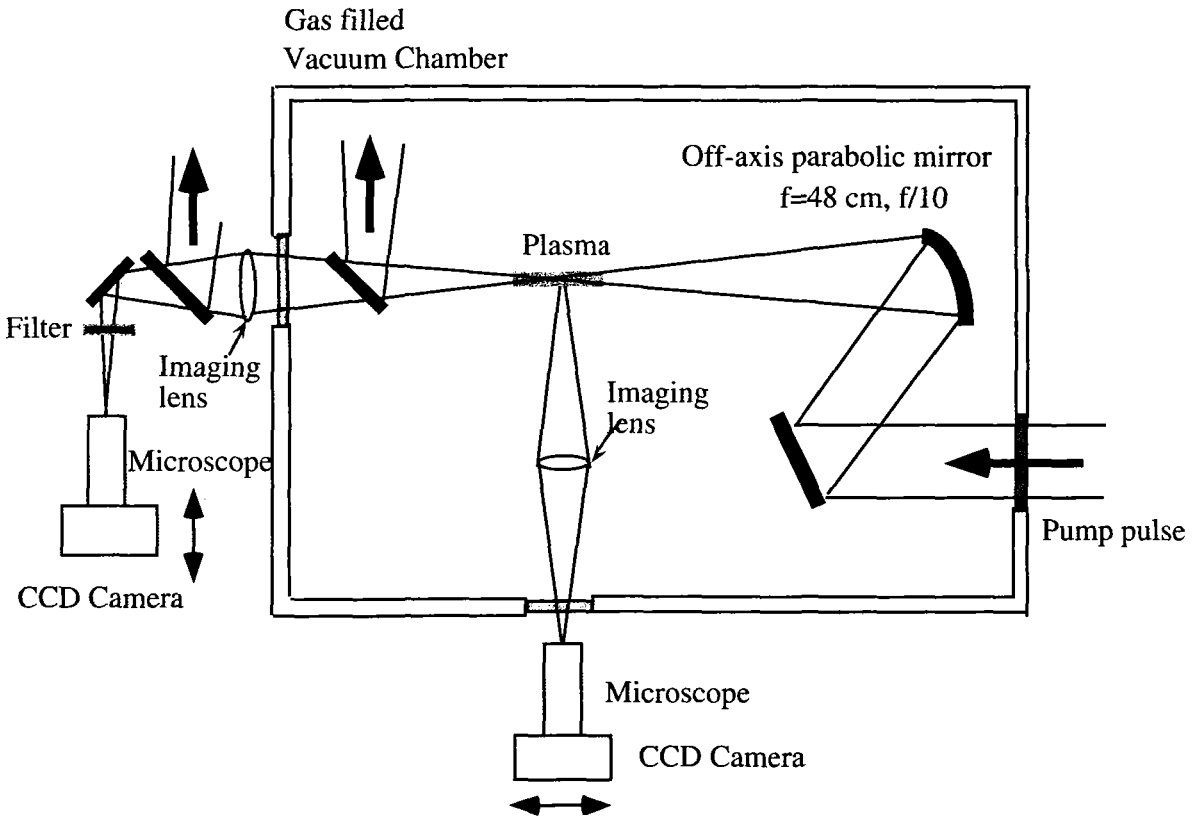

Figure 3.6: The experimental setup for the measurement of nonlinear laser-plasma phenomena.

critical power decreases with increasing the gas density, and the number of filaments is inversely proportional to the gas density form Eqs. (3.11) and (3.13). The critical power is 46 GW for 760 Torr. With a laser power of 2.4 TW there should be approximately 50 filaments for 760 Torr. A large number of filaments appears to occur in the experiment, although the exact filament number is difficult to determine.

The saturation intensity of the individual filament is the ionization threshold intensity of gas, the diameter d of the filament can be calculated by[54]

$$d = \frac{\lambda_0}{4E_0}\left(\frac{N_0}{N_2}\right)^{1/2}, \tag{3.14}$$

where E_0 is the breakdown or ionization threshold field of the gas. We can obtain an estimate of the size of the filaments by using the threshold intensity for singly ionizing helium of 1.47×10^{15} W/cm^2 in Eq. (3.14) and the corresponding values for the nonlinear index of refraction. For 760 Torr the filament size is 36 μm. If we look at the scale size of the bright spots which can be distinguished, they range between 10 and 50 μm in size. This is in rough agreement with the theoretical prediction.

This is a blank page.

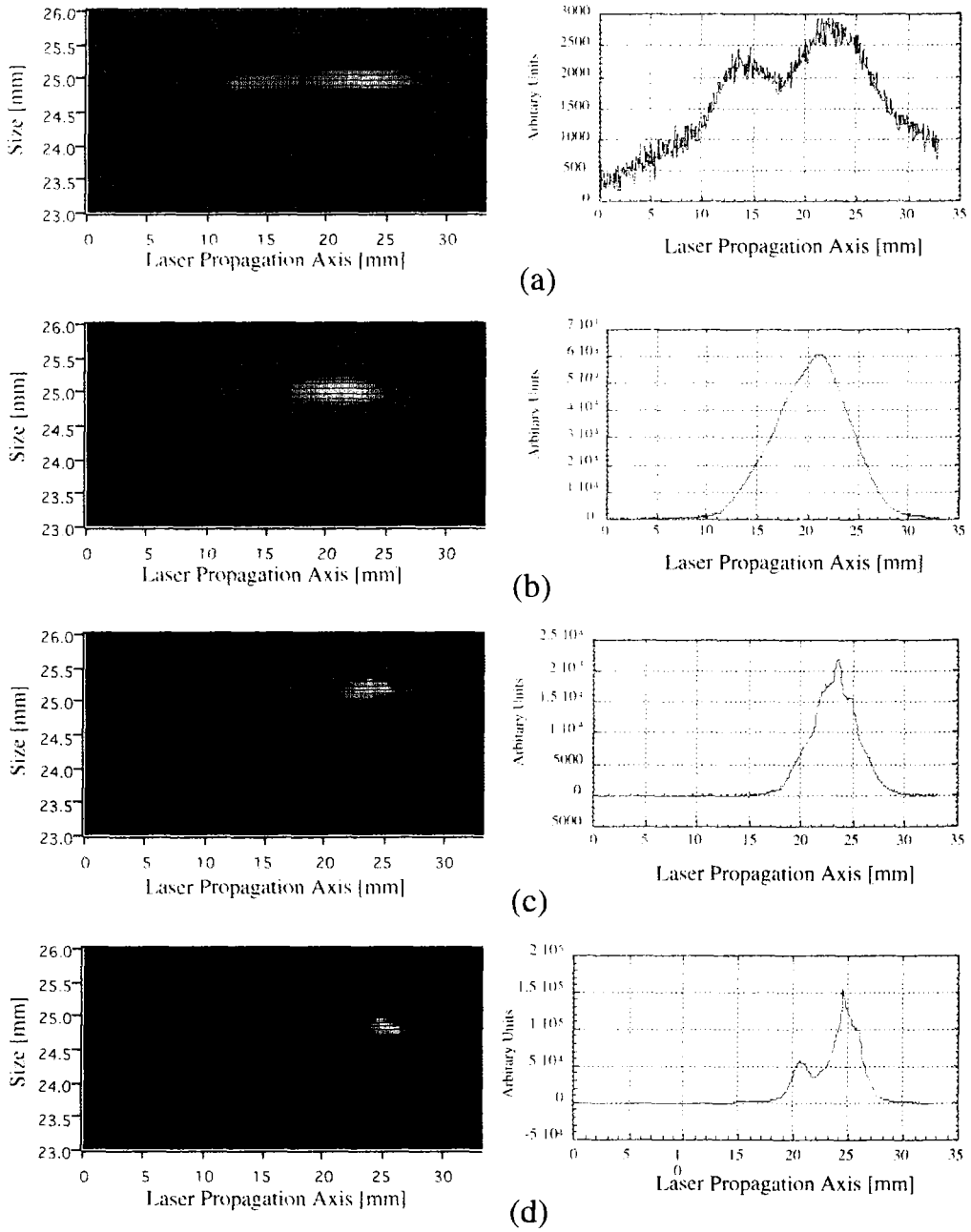

Figure 3.7: Side scattered radiation observed through a blue pass filter with a bandwidth between 410 and 532 nm FWHM at (a) 1 Torr, (b) 20 Torr, (c) 400 Torr, and (d) 760 Torr for a laser energy of 165 mJ.

This is a blank page.

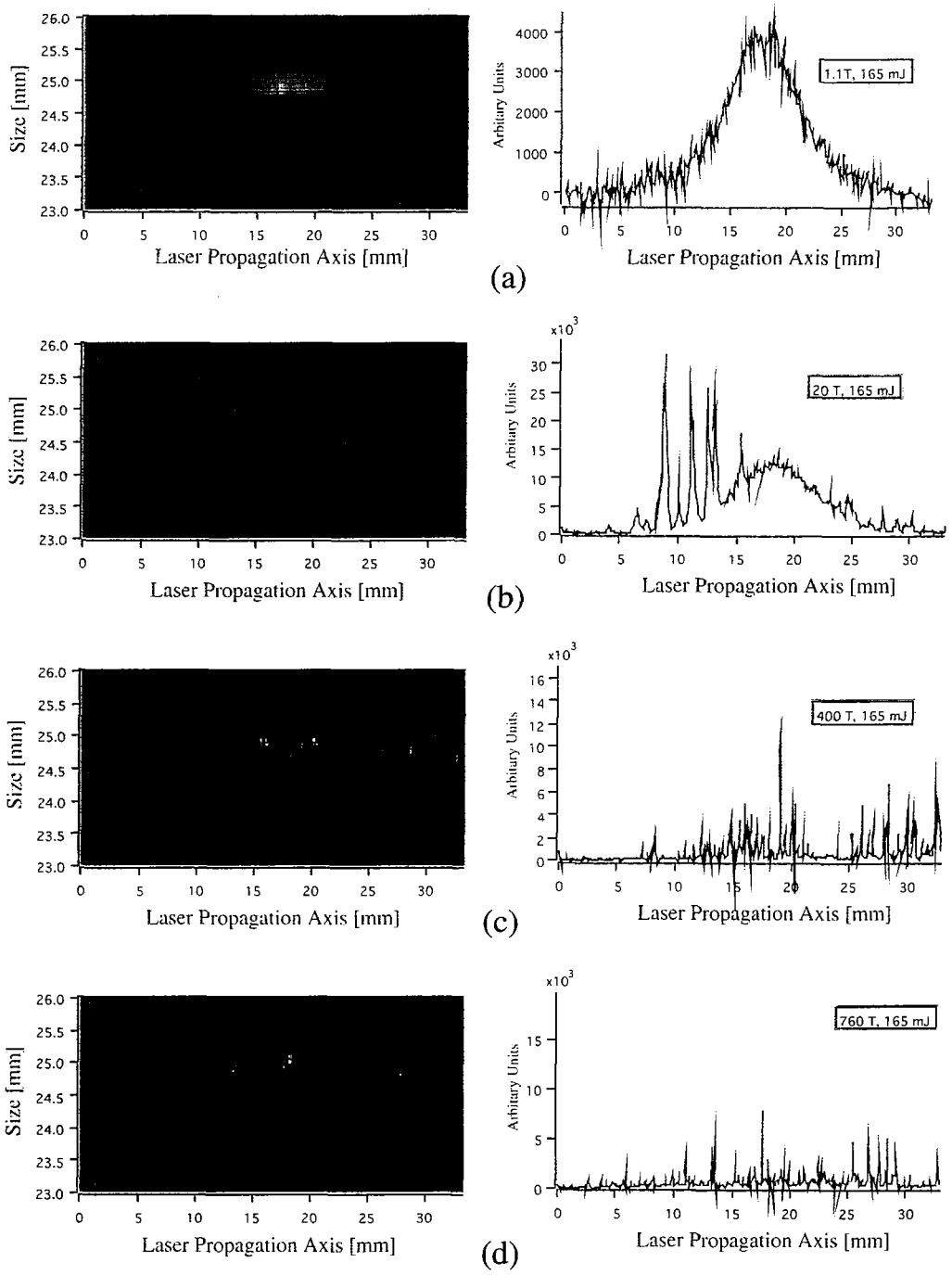

Figure 3.8: Side scattered radiation observed through an interferential filter centered at 793 nm with a width of 10 nm FWHM at (a) 1 Torr, (b) 20 Torr, (c) 400 Torr, and (d) 760 Torr for a laser energy of 165 mJ.

This is a blank page.

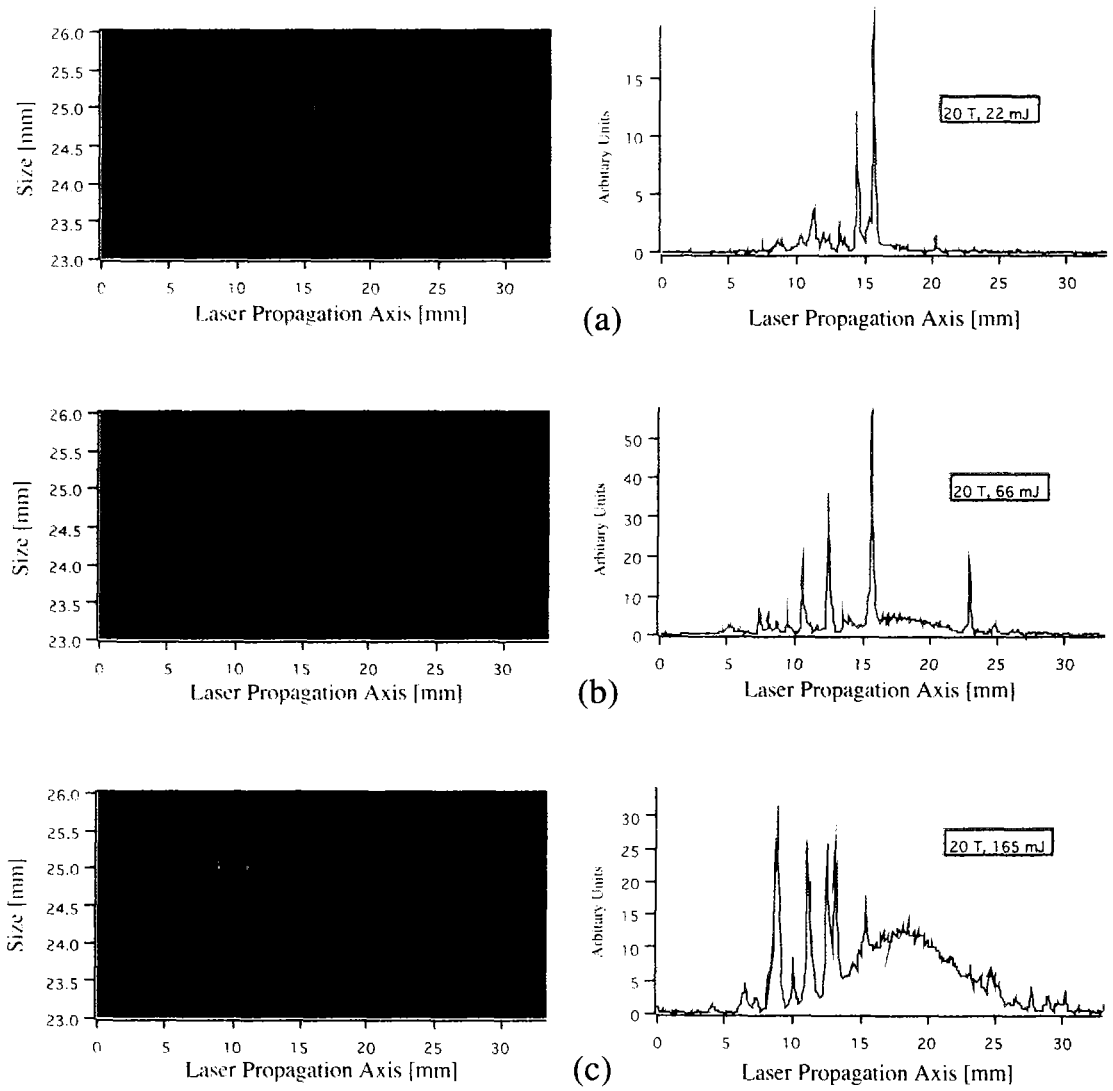

Figure 3.9: Side scattered radiation observed through an interferential filter centered at 793 nm with a width of 10 nm FWHM at 20 Torr for a laser energy of (a) 22 mJ, (b) 66 mJ, and (c) 165 mJ.

This is a blank page.

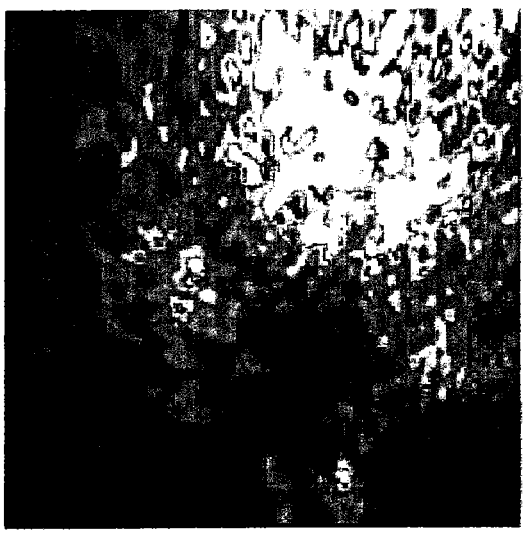

Figure 3.10: Forward scattered radiation image at the focus point for a laser energy of 230 mJ, and helium gas pressure of (a) 23 Torr, and (b) 760 Torr.

This is a blank page.

3.4 Blueshift of an Intense Laser Pulse

3.4.1 Principle of Blueshift

Since each filament is propagating with intensity near the threshold intensity for ionization of the gas, each filament is copropagating with density gradient. Normal blueshifted femtosecond laser pulses have been observed experimentally and a shift has been attributed to ionization[11]-[13]. It has been shown theoretically and numerically that a laser pulse which is propagating in copropagating ionization front will up-shift in frequency[7].

A phase shift $\Delta\phi$ can be expressed as the gradient of a refractive index along the propagation direction,

$$\Delta\phi = \int \Delta N \frac{\omega_0}{c} dz, \tag{3.15}$$

where ΔN is the defference of the refractive index and ω_0 is the frequency of the laser pulse. The frequency shift $\Delta\omega$ is given by

$$\Delta\omega = -\partial\frac{\Delta\phi}{\partial t} = -\frac{\omega_0}{c}\int_0^{c\tau} \frac{\partial\Delta N(z,t)}{\partial t} dz, \tag{3.16}$$

where $c\tau$ is the interaction length. The refractive index in an underdense plasma, i.e. $n_e \ll n_c$, is given by

$$N_e = \left(1 - \frac{n_e}{n_c}\right)^{1/2} \simeq 1 - \frac{1}{2}\frac{n_e}{n_c}, \tag{3.17}$$

where n_e is the plasma electron density, $n_c = \pi/r_e\lambda_0^2$ is the critical density, $r_e = e^2/m_e c^2$ is the classical electron radius, and λ_0 is the wavelength of the laser pulse. The gradient of the refractive index is

$$\frac{\partial\Delta N(z,t)}{\partial t} = \frac{(1 - n_e(z)/2n_c) - 1}{L(z)/c} = -\frac{n_e(z)}{2n_c}\frac{c}{L(z)}, \tag{3.18}$$

where $L(z)$ is the length of the ionization front. The frequency shift is given by

$$\Delta\omega = \frac{\omega_0}{2n_c}\int_0^{c\tau} \frac{n_e(z)}{L(z)} dz, \tag{3.19}$$

where $c\tau$ is the laser-ionization-front propagating distance. Assuming a linear density gradient this shift is given by

$$\Delta\omega = \omega_0\frac{c\tau}{2L_0}\frac{n_e}{n_c} = \omega_0\frac{c\tau}{2L_0}\frac{\omega_p^2}{\omega_0^2}, \tag{3.20}$$

where L_0 is the length of the ionization front for the linear density gradient and ω_p is the plasma frequency.

Here, we consider a laser pulse in the ionization front. The dispersion relation is

$$\omega_0^2 = \omega_p^2 + c^2k^2, \tag{3.21}$$

where k is the wave number of light. The phase velocity of the pulse is $v_p = \omega_0/k$. If the frequency shift remains small compared to ω_0, the local phase velocity of the pulse is

$$\frac{v_p}{c} = \left(1 - \frac{\omega_p^2}{\omega_0^2}\right)^{-1/2} \tag{3.22}$$

For $\omega_0 \gg \omega_p$ the local phase velocity of the pulse is approximately

$$\frac{v_p}{c} = 1 + \frac{\omega_{p0}^2}{2\omega_0^2}\frac{\omega_p^2}{\omega_{p0}^2} = 1 + \frac{\omega_{p0}^2}{2\omega_0^2}\frac{n_e}{n_0}, \tag{3.23}$$

where ω_{p0} and n_0 are the plasma frequency and the plasma density after ionization, respectively. Assuming a linear density gradient a frequency shift is given as photon acceleration by

$$\frac{\Delta\omega}{\omega_0} = \frac{dv_p}{d\zeta}\tau, \tag{3.24}$$

where $\zeta = z - ct$. The phase velocity gradient is given by

$$\frac{dv_p}{d\zeta} = \frac{\omega_{p0}^2}{2\omega_0^2}\frac{c}{n_0}\frac{dn_e}{d\zeta} = \frac{\omega_{p0}^2}{2\omega_0^2}\frac{c}{L_0}, \tag{3.25}$$

The frequency shift is rewritten in the form

$$\frac{\Delta\omega}{\omega_0} = \frac{c\tau}{2L_0}\frac{\omega_{p0}^2}{\omega_0^2}, \tag{3.26}$$

The equation of the frequency shift calculated from photon acceleration is the same as the equation of the frequency shift calculated from gradient of the refractive index. In other word, blueshift is photon acceleration.

Here, we rewrite the plasma frequency ω_{p0} to ω_p. We obtain the same equation as Eq. (3.20). The shifted laser frequency ω_s is

$$\omega_s = \omega_0\left(1 + \frac{c\tau}{2L_0}\frac{\omega_p^2}{\omega_0^2}\right). \tag{3.27}$$

For $c\tau \ll L_0\omega_0^2/\omega_p^2$ we can rewrite the equation to

$$\omega_s = \omega_0\left(1 + \frac{c\tau}{L_0}\frac{\omega_p^2}{\omega_0^2}\right)^{1/2} \tag{3.28}$$

3.4.2 Measurement of Anomalous Blueshift

In Fig. 3.6 the CCD camera replaced to a spectrometer to measure the forward scattered radiation spectrum.

Figure 3.11 shows the forward scattered radiation spectrum for various pulse energies after the laser pulse has traveled through the gas chamber filled with helium gas at (a) 1 Torr, (b) 20 Torr, (c) 400 Torr, and (d) 760 Torr. In Fig. 3.11(a) the spectrum at 1 Torr remains centered near the initial laser wavelength of 793 nm with shoulders at the laser wavelength of 787 nm independent of the energy of the laser pulse. At 20 Torr in Fig. 3.11(b) a blue-shifted peak in the spectrum can be seen above about 50 mJ (0.5 TW) of laser peak power. The peak in the blue-shifted component of the radiation remains centered around 746 nm independent of the laser peak power. At higher power the whole spectrum shifts to this value. The amount of blueshift remains fixed above specific pressures and laser powers. We call the phenomenon "anomalous blueshift". The anomalous blueshift of the laser pulse is observed to be about $\Delta\lambda/\lambda_0 \approx 5.9\%$ at the higher pressure than 20 Torr.

We compare Fig. 3.8 and Fig. 3.11. At 1 Torr we can observe no filamentation and no anomalous blueshift. At 760 Torr a whole laser pulses are blue-shifted and self-focused with filaments. At 20 Torr these are between the 1 Torr case and 760 Torr case in both figures. The fact implies that the anomalous blueshift occurs due to the filamentation.

When different gases are used in the chamber, the same blueshift phenomenon occurs. In the case of argon gas at 26 Torr and laser energy of 38 mJ (0.4 TW) a complete blueshift of the laser pulse appears at 749nm (see Fig. 3.12(a)). This is at lower pressure and power than in the case of helium. Figure 3.12(b) shows the spectra for the case of nitrogen gas. It can be seen that the complete blueshift to 742 nm is observed even at 10 Torr for a laser energy of 206 mJ (2 TW). The anomalous blueshift of the laser pulse for argon and nitrogen are observed to be about $\Delta\lambda/\lambda_0 \approx 5.6\%$ and $\Delta\lambda/\lambda_0 \approx 6.4\%$, respectively. For these gases the amount of blueshift is also independent of the laser power and the density of gas.

3.4.3 Analysis of Anomalous Blueshift

For $\mathcal{P} > \mathcal{P}_{cr}$ the gradient scale length becomes constant. Assuming a linear density gradient this shift is given by[7]

$$\omega_s = \omega_0\sqrt{1 + \frac{c\tau}{L_0}\frac{\omega_p^2}{\omega_0^2}} = \omega_0\sqrt{1 + \frac{c\tau}{L_0}\frac{n_e}{n_c}}, \tag{3.29}$$

where τ is the propagation time, L_0 is the gradient scale length, ω_p is the plasma frequency, and ω_0 is the initial laser frequency.

Figure 3.13 shows a schematic of the laser propagation due to balancing the plasma refraction and natural diffraction against the self-focusing. Figure 3.13(a) shows a profile of a laser with self-focusing. Figure 3.13(b) shows a lineout of Thomson scattering. Figure 3.13(c) shows the Thomson scattered radiation at 20 Torr for a laser energy of 165 mJ. The propagation of the laser pulses is based on the refraction and the self-focusing with filamentation. We can estimate the propagation time τ to be the depletion time of the filament. Here we assume that the main depletion mechanism is due to refraction of light. The depletion distance is approximately equal to the refraction distance. So, the propagation distance $c\tau$ is roughly equal to the refraction distance. This is based on recent simulations of the propagation of high intensity lasers in air where the main arrest mechanism was attributed to the refraction of the light in the plasma[55]. The refraction distance l_D is roughly given by[56]

$$l_D = \frac{\lambda_0}{2}\frac{n_c}{n_e}, \tag{3.30}$$

where n_e is the plasma density, n_c is the critical plasma density, and λ_0 is the laser wavelength. The refraction and the self-focusing cause the spike in Fig. 3.13(b). This refraction distance is roughly equal to the spike distance. The distance is measured from the Thomson side scattered images in Figs. 3.8 and 3.9. The distances of the spikes ranged between 0.5 and 1.5 mm at 20 Torr. The calculated refraction distance is about 1 mm. The spike distance decreases with increasing pressure of the gas. Substituting Eq. (3.30) into Eq. (3.29), then we obtain

$$\omega_s = \omega_0\sqrt{1 + \frac{\lambda_0}{2L_0}}, \tag{3.31}$$

which indicates that the frequency shift is independent of the plasma density, type of gas, and laser intensity. The amount of shift just depends on λ_0 and L_0. L_0 is roughly constant due to the filamentation that fixes the maximum intensity at the ionization threshold of the gas.

For $\mathcal{P} > \mathcal{P}_{cr}$ the intensity is given by

$$I_i = \frac{\mathcal{P}_{cr}}{\pi(d/2)^2}, \tag{3.32}$$

where d is the diameter of the filament. The intensity ca be rewritten by Eqs. (3.13)(3.11) and (3.14). We can obtain

$$I_i = \frac{2.88E_0^2}{N_0^2 c}. \tag{3.33}$$

This is a blank page.

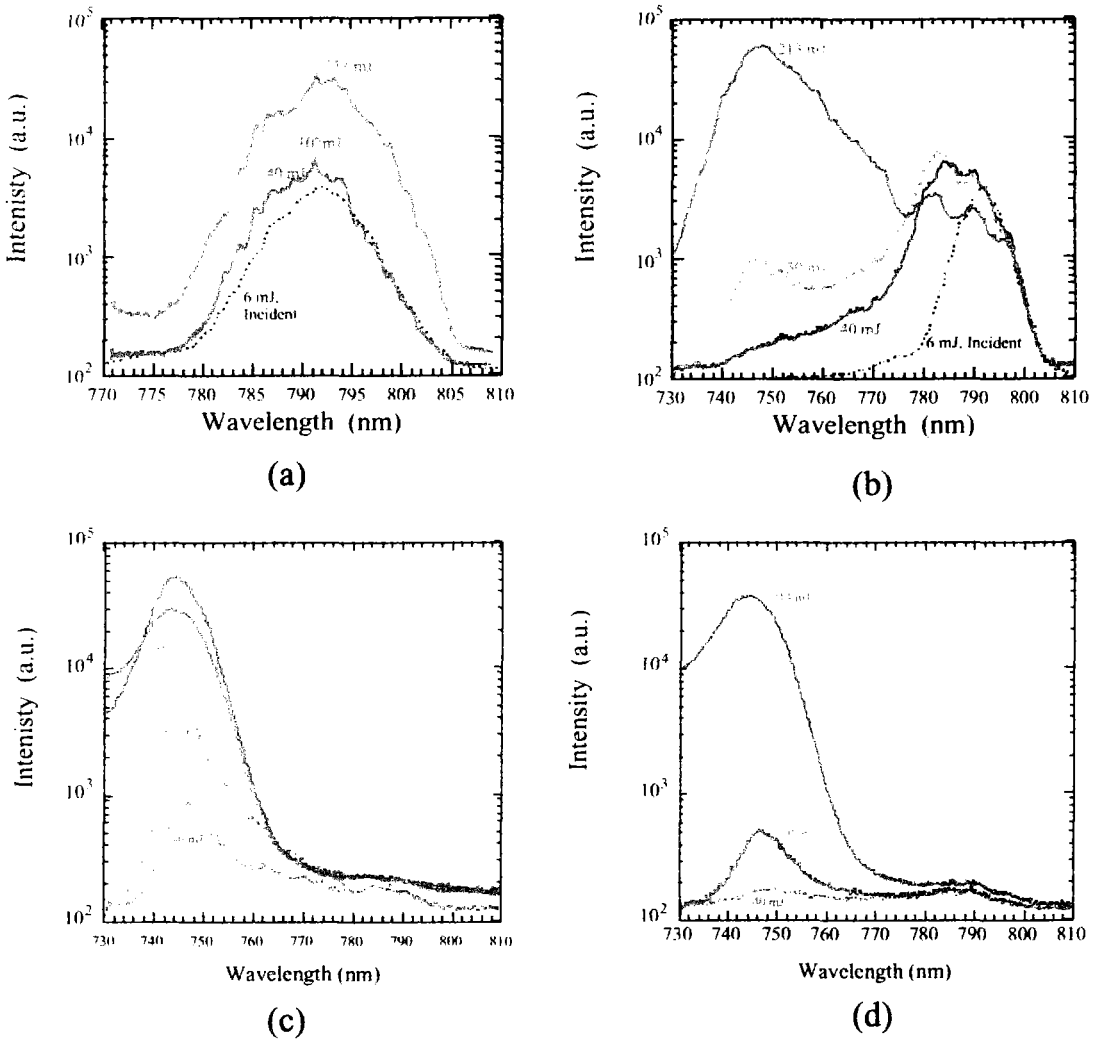

Figure 3.11: Forward scattered radiation spectrum after the laser pulse has through the chamber in helium gas at (a) 1 Torr, (b) 20 Torr, (c) 400 Torr, and (d) 760 Torr for various laser energies.

This is a blank page.

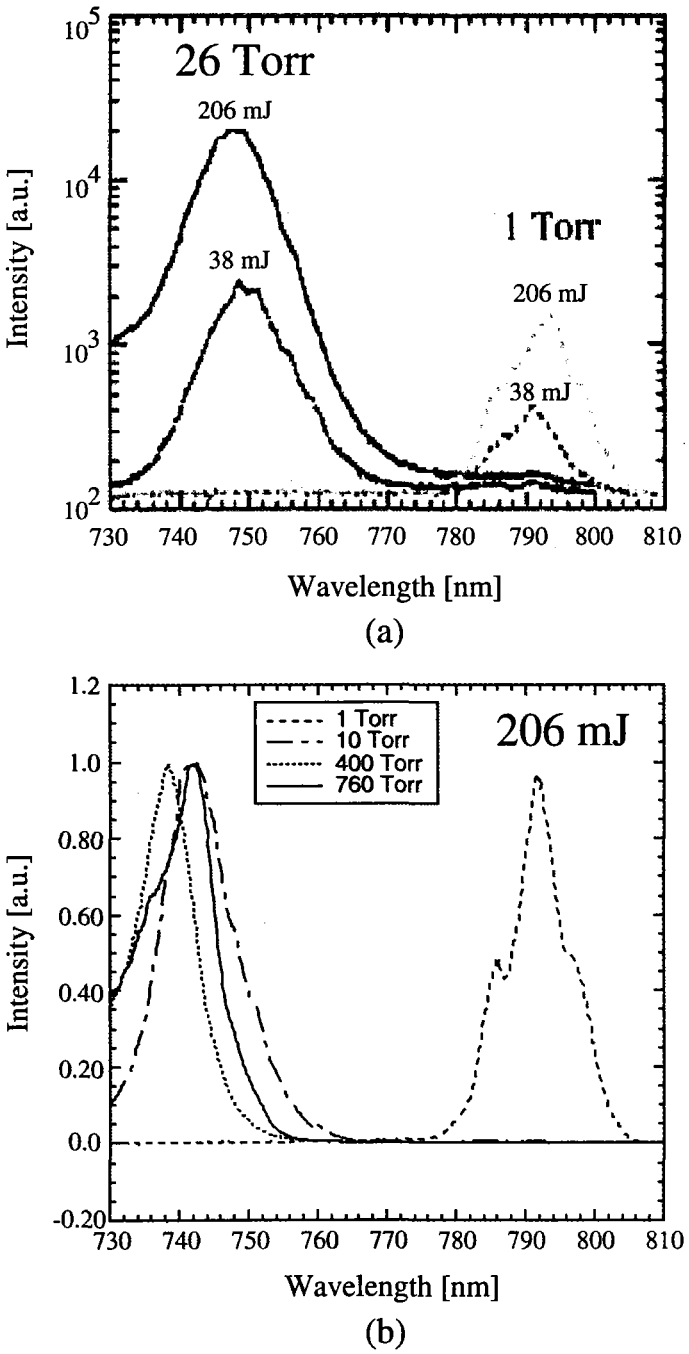

Figure 3.12: Forward scattered radiation spectrum after the laser pulse has through the chamber in (a) argon gas and (b) nitrogen gas at various pressures and laser energies.

Table 3.1: The amount of blueshift for various gases.

Gas	Experimental results [%]	Theoretical value [%]
He^+	5.9	6.0
N^{3+}	6.4	6.6
Ar^{3+}	5.6	5.4

The usual refractive index of gas is nearly equal to 1 (see Eq. (3.10)). The laser intensity is independent of the gas density and the laser power. In other words, the laser intensity is nearly equal to the intensity of the ionization threshold, since each filament is propagating with intensity near the threshold intensity for ionization of the gas. The minimum threshold of the laser intensity is 1.47×10^{15} W/cm^2 for the ionization potential of 24.6 eV (see Eq. (3.7)). The laser intensity become higher than the ionization threshold intensity like a Fig. 3.13(a). Approximately, we make an assumption that the laser intensity I_i is slightly higher than the ionization threshold intensity I_{th}, i.e.

$$I_i = 1.0004 I_{th}. \tag{3.34}$$

For helium gas L_0 is 3.2 μm (10.7 fs) from Eqs. (2.3) and (3.8). We obtain the frequency shift $\Delta\lambda/\lambda_0 = 6.0\%$ from Eq. (3.31). In addition, the ionization thresholds for nitrogen and argon are lower than the ionization thresholds for helium. We make an assumption that the nitrogen and argon are ionized to N^{3+} and Ar^{3+} for the pre-focusing with the OAP. Table 3.1 shows the experimental results and the theoretical amount of blueshift for various gases. The experimental results are in good agreement with the theoretical predictions.

In the anomalous blueshift, the whole spectrum shifts to a fixed wavelength. This mechanism is illustrated in Fig. 3.14. The leading front of the laser pulse ionizes gas with blueshift, and the retarding part behind the ionization front of the laser pulse propagates in plasma without blueshift as shown in Fig. 3.14(a). Since the phase velocity of a laser pulse in the ionization front is slower than that in plasma due to the difference of refractive indexes between gas and plasma, the leading part with blueshift moves behind the retarding part as shown in Fig. 3.14(b). Eventually, the whole spectrum shifts to the fixed wavelength by repeating ionization with blueshift and filamentation in a distance of spikes as shown in Fig. 3.13.

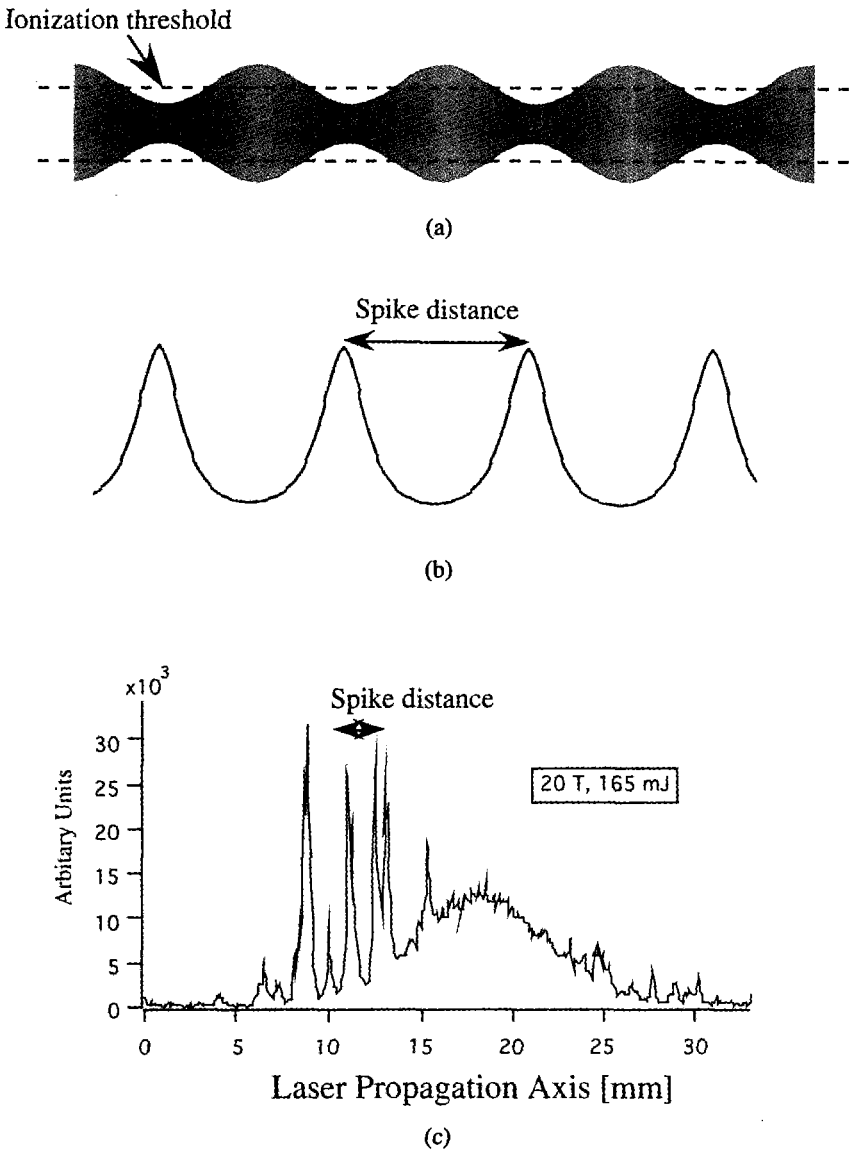

Figure 3.13: A scheme for the self-focusing and side scattering. (a) shows a profile of a laser with self-focusing, (b) shows a lineout of laser intensities, and (c) shows spike distance measured by side scattered radiation using an interferential filter centered at 793 nm with a width of 10 nm FWHM at 20 Torr for a laser energy of 165 mJ. The spike distance is a separation of the self-focusing.

This is a blank page.

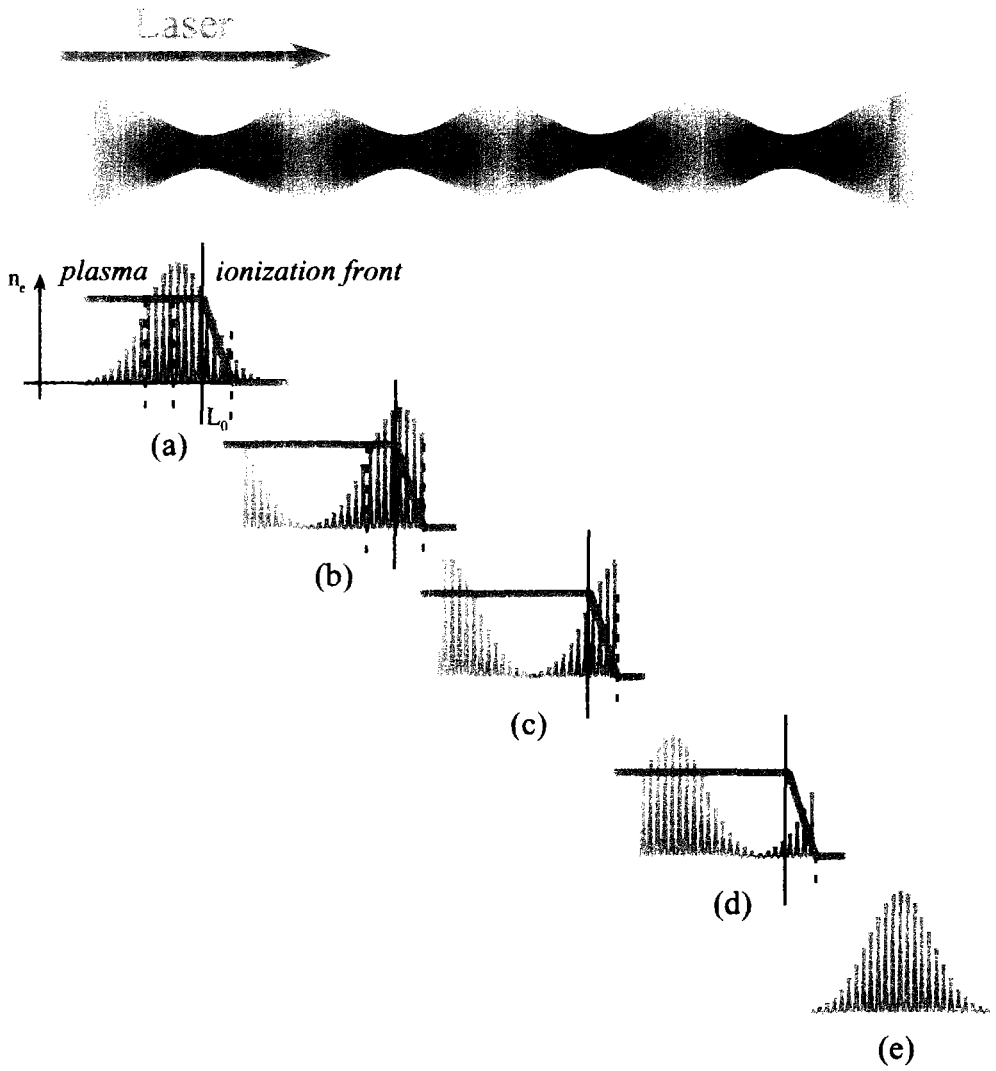

Figure 3.14: A schematic of the mechanism for the anomalous blueshift. The solid line shows evolution of the plasma density n_e. The red lines show the original laser pulse and the blue lines show the blue-shifted laser pulse. The blueshift proceed from (a) to (e).

This is a blank page.

4. Observation of Laser Wakefield

4.1 Measurement of Gas Density Distribution

4.1.1 Principle of Gas Density Measurement

We measure the gas density distribution shown in Fig. 4.1. In the Mach-Zehnder interferometer, a change of the optical path length due to the difference of the speed of light in the material produces a fringe phase shift due to the variation of the refractivity for the two optical paths. The phase shift $\Delta\phi$ is given by

$$\Delta\phi = \int (N_2 - N_1)\frac{\omega}{c} dL, \tag{4.1}$$

where N_1 is the refractive index in vacuum, i.e. $N_1 = 1$, N_2 is the refractive index of the gas, ω is the frequency of the probe laser, c is the speed of light in vacuum, and L is the interaction distance of the probe beam with the gas. Assuming adiabatic expansion of the gas for the pressure p [atm] at the temperature T [K], the refractive index difference is given by

$$\Delta N = N_2 - N_1 = (N_g - 1)p\frac{273}{T}. \tag{4.2}$$

where N_g is the refractive index at 0 °C and 1 atm. The phase shift is obtained as

$$\frac{\Delta\phi}{2\pi} = 3.74 \times 10^{-14}(N_g - 1)\frac{d \cdot L}{\lambda}, \tag{4.3}$$

where L is the interaction length in mm, λ is the wavelength of the probe laser in nm, and d is the gas density in cm^{-3}. Table 4.1 shows the refractive index of various gases.

For helium gas ($N_g = 1.000\,035$) at 24 °C, the gas density is given by

$$d = 7.65 \times 10^{17}\frac{\lambda}{L}\frac{\Delta\phi}{2\pi}. \tag{4.4}$$

The gas density can be calculated by Eq. (4.4) for a gas target with uniform thickness. For a gas target with an arbitrary shape, we must correct the interaction distance along the path of each ray of the probe beam. Assuming that the gas density distribution with respect to radial position r from the nozzle center has axial symmetry as $d = f(r)$, the phase shift is

$$\frac{\Delta\phi}{2\pi} = C\int f(r)dy, \tag{4.5}$$

where C is a constant. The gas density distribution can be calculated from the Abel inversion technique as follows. Let us consider a cylindrically sliced gas target with thickness Δr shown in Fig. 4.2. The phase shift along the line k can be calculated as

$$\frac{\Delta\phi}{2\pi}(k) = C \cdot \sum_{i=1}^{k} d(i) \cdot L_k(i), \tag{4.6}$$

Here

$$L_k(i)_{i=1,k-1} = \sqrt{(r - (i-1)\Delta r)^2 - x^2(k)} - \sqrt{(r - i\Delta r)^2 - x^2(k)}, \tag{4.7}$$

Table 4.1: The refractive index of various gases

Gas	$(N_g - 1) \times 10^6$
He	35
Ne	67
Ar	283
Xe	707
H_2	140
N_2	298

$$L_k(k) = \sqrt{(r - (k-1)\Delta r)^2 - x^2(k)}, \tag{4.8}$$

$$x(k) = r + \frac{\Delta r}{2} - k\Delta r, \tag{4.9}$$

where $d(k)$ is the density at the kth sliced cylinder, $L_k(i)$ is the ith length of line k and the $x(k)$ is the distance of the line k from the nozzle axis. The gas densities $d(i)$ can be obtained from a set of simultaneous linear equations (4.6).

4.1.2 Time-resolved Gas Density Measurements

The gas density was measured with the Mach-Zehnder interferometer consisting of a He-Ne laser ($\lambda = 632.8$ nm), two mirrors, and two beam splitters, shown in Fig. 4.1. The laser beam expanded to 1 cm in diameter is split into two beams which travel along separate paths. The gas-jet nozzle with an orifice diameter of 0.8 mm is placed inside a vacuum chamber evacuated to 10^{-5} Torr. One of the two beams travels through the gas-jet in the vacuum chamber. The two laser beams are merged to make an interferogram on a screen as shown in Fig. 4.3. The interferogram is captured with a charge-coupled-device (CCD) camera with an image intensifier. The time-resolved measurement can be made by gating the CCD camera triggered with some delay between the CCD camera and the gas-jet. The room temperature was controlled at 24 °C within 0.3 °C during this measurement. The opening duration of the gas-jet valve was 2 ms and the gate time of the CCD camera was 5 μs. The distribution of the gas density can be calculated from the phase shift and Eq. (4.4).

Figures 4.4(a)-(f) show contour plots of the gas density distribution of N_2 gas at a backing pressure of 25 atm with a delay time of (a) 1.0, (b) 1.2, (c) 1.4, (d) 1.6, (e) 1.8 and (f) 2.0 ms. Figures 4.5(a)-(f) show contour plots of the gas density distribution of N_2 gas with a delay time of 1.6 ms at a backing pressure of (a) 5, (b) 10, (c) 15, (d) 20, (e) 25, and (f) 30 atm. The gas flows from bottom to the top starting at $y = 0$. The position $x = 0$ is the center of the gas-jet nozzle. The gas expands to up and sides like a cone and the gas density becomes stable at the distance 1.5 mm from the nozzle.

Figure 4.6 shows a contour plot of the He gas density distribution at a backing pressure of 30 atm with a 1.6 ms delay. Figure 4.7(a) shows the radial distribution 0.7 mm below the end of the gas-jet nozzle and (b) shows the axial distribution along the nozzle axis. The time-resolved measurements show that the gas density builds up quickly to a constant value in 0.8 ms as shown in Fig. 4.8. From measurements of nitrogen gas, it is found that the gas density distribution is uniform at the point of 1.5 mm away from the gas-jet nozzle. From these measurements, we find the optimum laser focus position at 1.5 mm off the gas-jet and a delay of 1.6 ms to provide an appropriate gas density for wakefield excitation. Since the gas density is inversely proportional to the square of the distance from the nozzle and linearly proportional to the backing pressure, the neutral gas density of He gas is $\approx 3.6 \times 10^{17}$ cm^{-3} at the pump laser focus with a backing pressure of 10 atm.

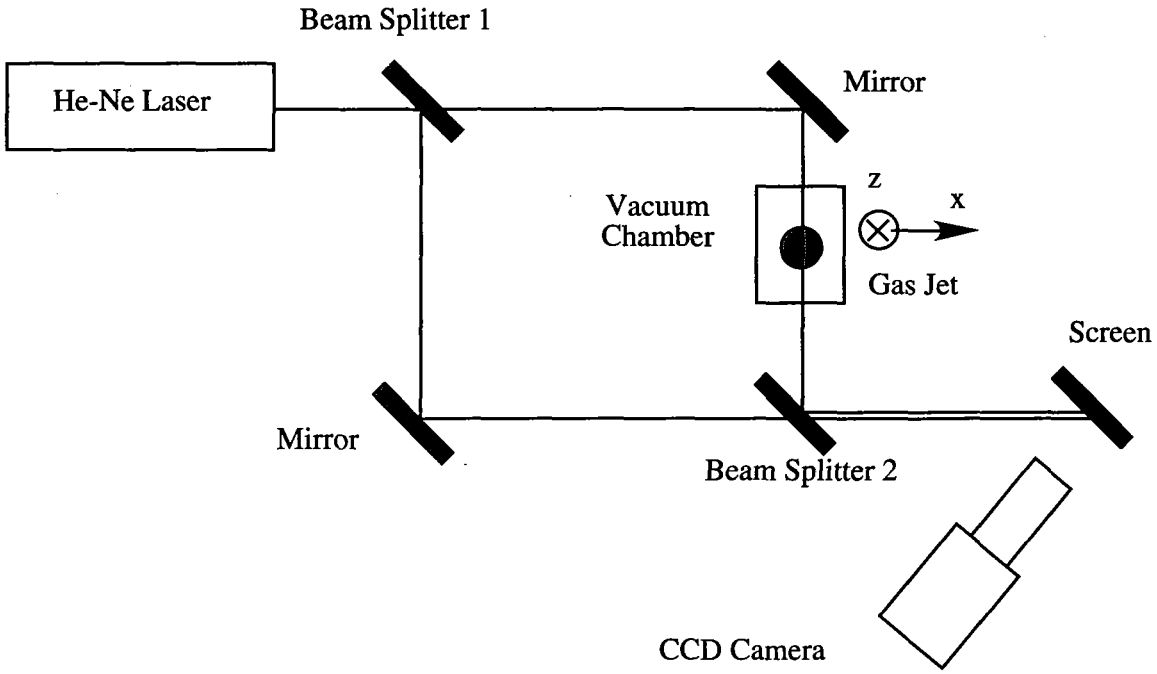

Figure 4.1: A schematic of the Mach-Zehnder interferometer for measurement of the gas density distribution of the gas-jet.

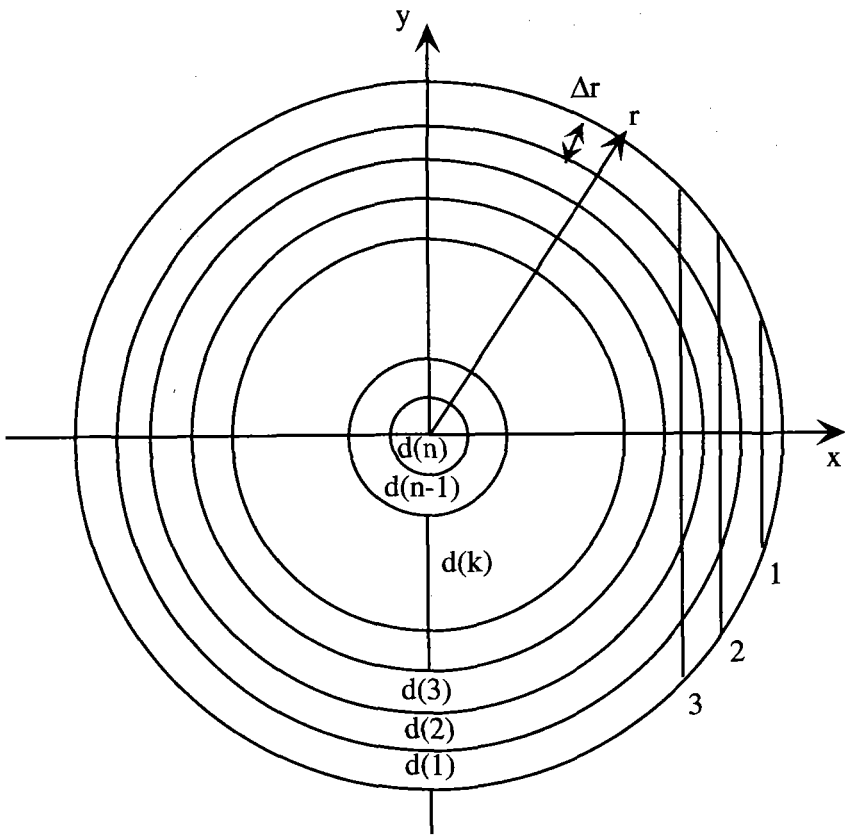

Figure 4.2: An illustration of the reconstruction of the gas density distribution of the gas-jet with axial symmetry by the Abel inversion technique.

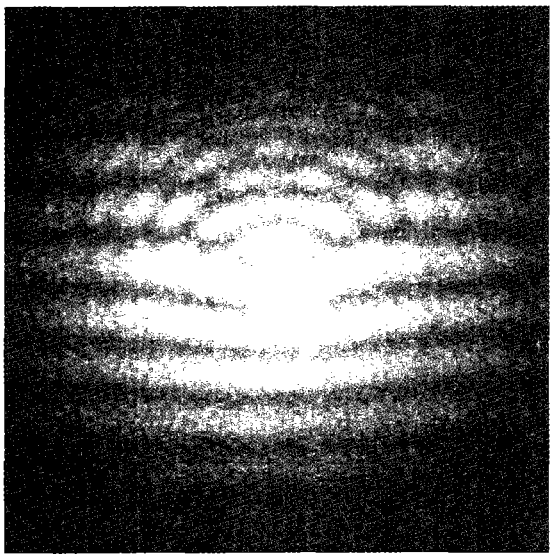

(a)

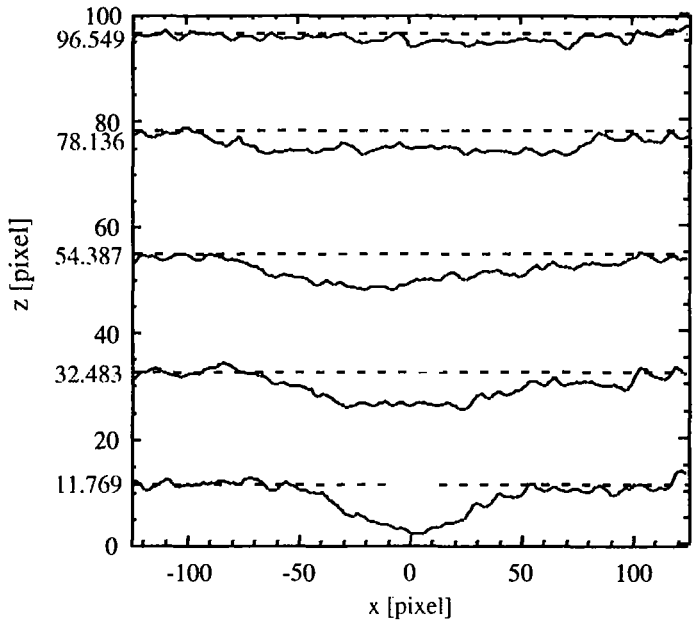

(b)

Figure 4.3: The interferogram of nitrogen gas ejected from the gas-jet at a backing pressure 25 atm. (a) shows a typical image taken by the CCD camera and (b) its 2D projection of the fringe phase shifts at the transverse distance x and the axial distance z from the center of the gas-jet nozzle.

This is a blank page.

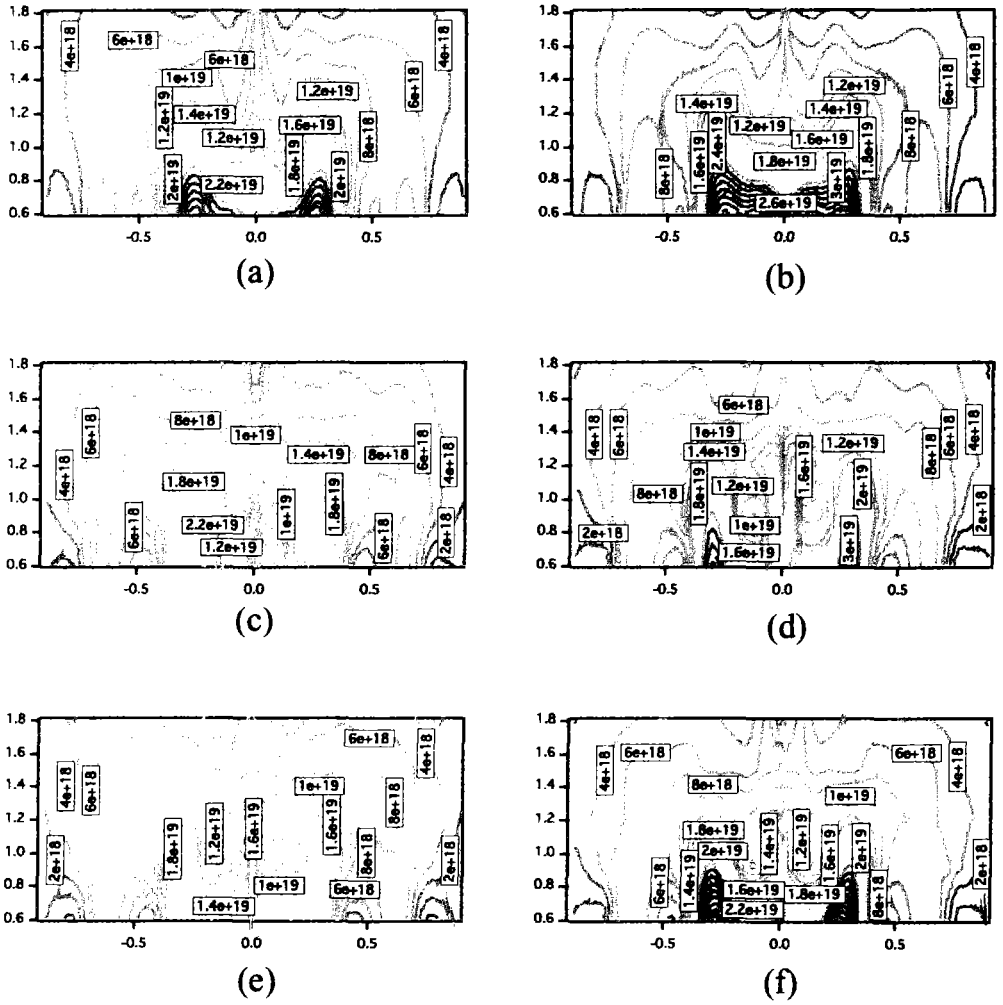

Figure 4.4: Contour maps of the gas density distribution of N_2 gas at a backing pressure of 25 atm with a delay time of (a) 1.0 ms, (b) 1.2 ms, (c) 1.4 ms, (d) 1.6 ms, (e) 1.8 ms and (f) 2.0 ms.

This is a blank page.

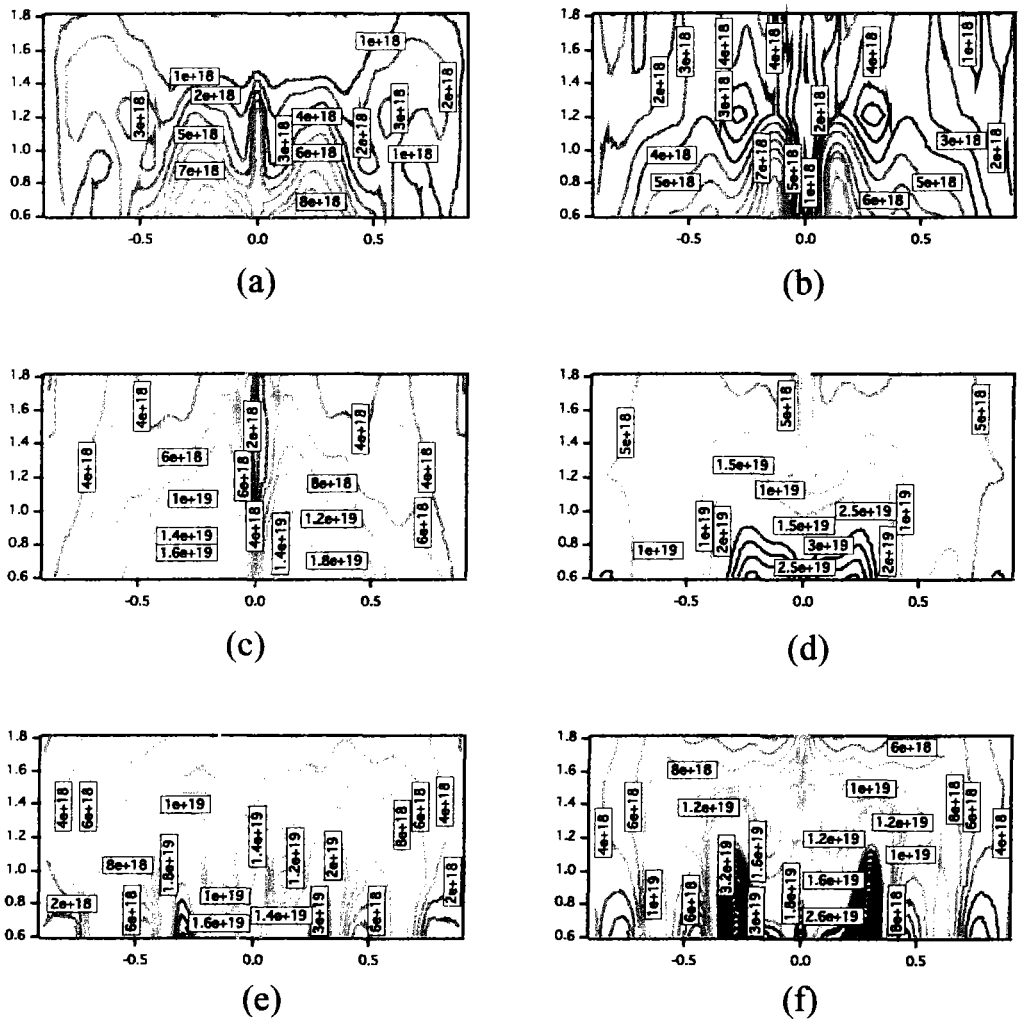

Figure 4.5: Contour maps of the gas density distribution of N_2 gas at a backing pressure of (a) 5 atm, (b) 10 atm, (c) 15 atm, (d) 20 atm, (e) 25 atm and (f) 30 atm with a delay time of1.6 ms.

This is a blank page.

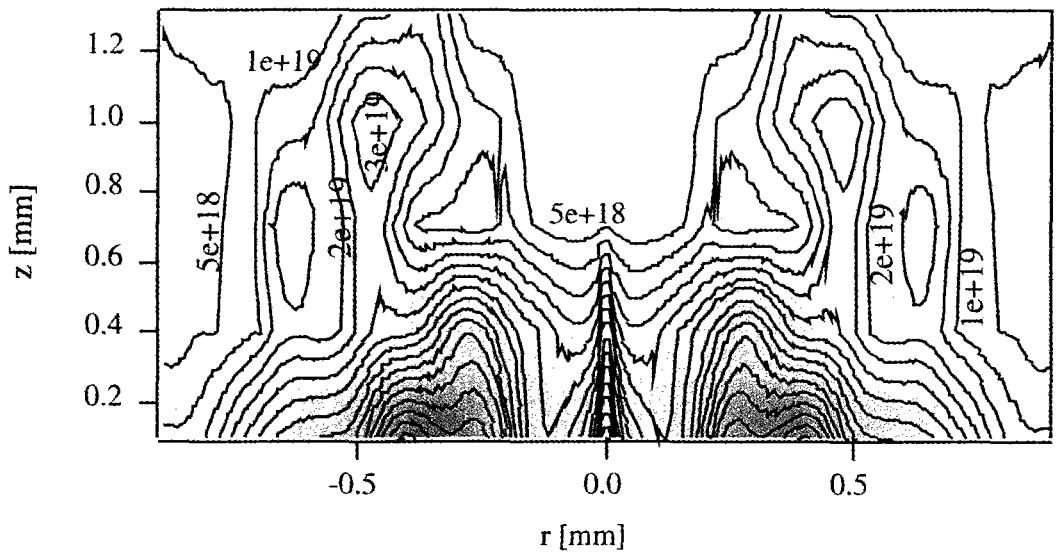

Figure 4.6: A contour map of the gas density distribution of He gas at a backing pressure of 30 atm with a delay time of 1.6 ms.

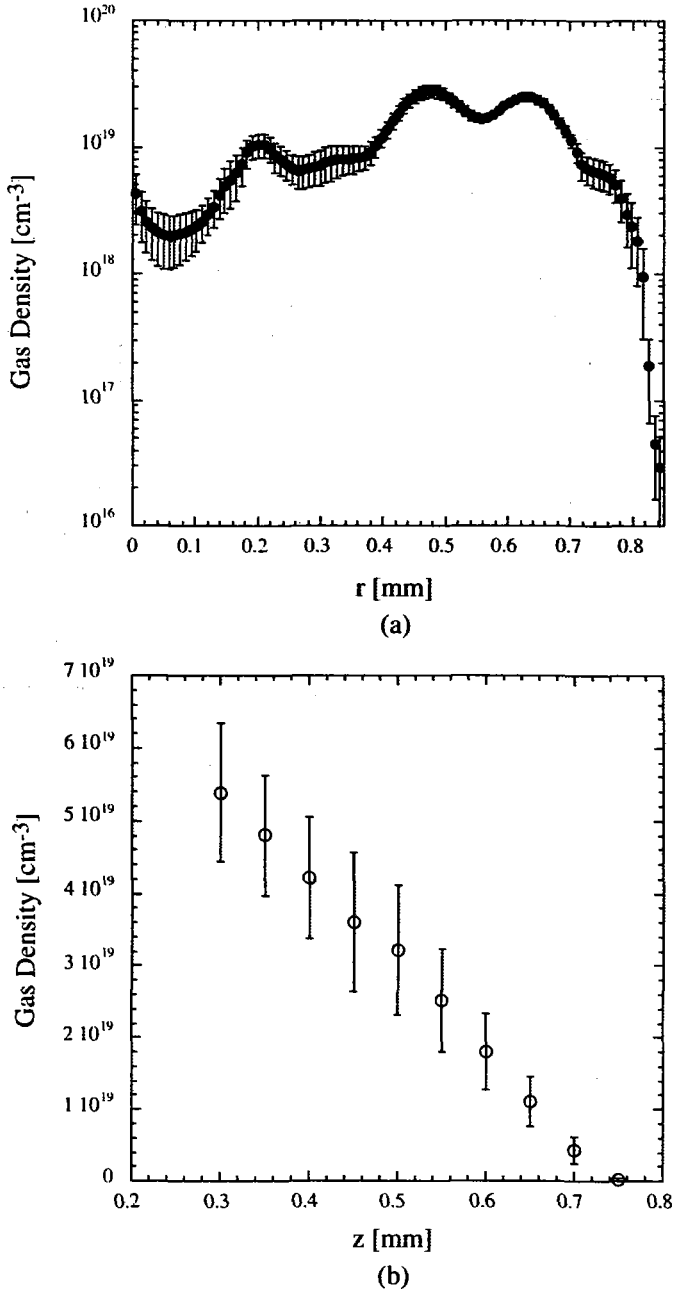

Figure 4.7: The gas density distribution measured for He gas at a backing pressure of 30 atm with a delay time of 1.6 ms: (a) is the radial distribution 0.7 mm below the end of the gas-jet nozzle and (b) the axial distribution along the nozzle axis.

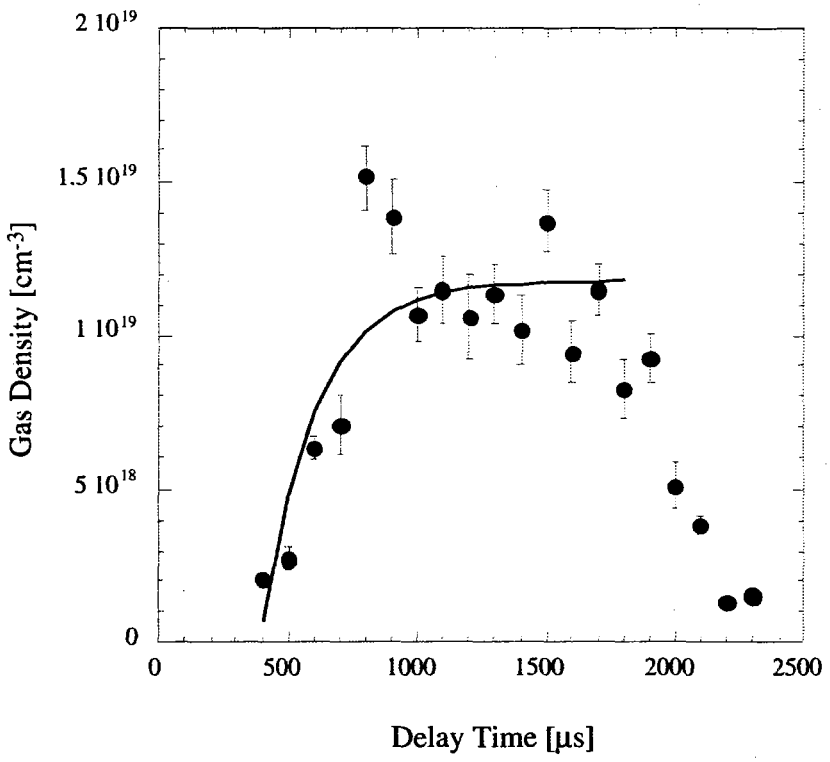

Figure 4.8: The gas density distribution of He gas 0.7 mm below the end of the gas-jet for the backing pressure of 30 atm as a function of the delay time between the gas-jet opening time and the CCD camera gating time.

4.2 Measurement of Wakefields

4.2.1 Frequency Domain Interferometry

Let us consider two probe pulses displaced temporally by a time T with a phase shift $\Delta\phi$ induced by a change in the medium between the two pulses, where the electric fields are given by

$$E_1(t) = E(t)\exp(i\omega_0 t), \tag{4.10}$$

$$E_2(t) = E(t-T)\exp(i\omega_0(t-T)+\Delta\phi), \tag{4.11}$$

and ω_0 is the laser frequency. The power spectrum $I(\omega)$ measured by the spectrometer is obtained from the Fourier transform of the sum of the two fields:

$$I(\omega) = |\mathcal{F}[E_1(t)+E_2(t)]|^2 = 2|E(\omega-\omega_0)|^2(1+\cos(\omega T+\Delta\phi)). \tag{4.12}$$

Thus we have frequency-domain fringes separated by $2\pi/T$ with a phase shift $\Delta\phi$ in the spectrum. The phase difference of the two pulses traveling through different refractive index materials is

$$\Delta\phi = \int (N_2 - N_1)\frac{\omega_{pr}}{c}dL, \tag{4.13}$$

where N_1 is the refractive index of the first probe pulse, N_2 is the refractive index of the second probe pulse, ω_{pr} is the frequency of the probe pulses, c is the speed of light, and L is the interaction length. The refractive index in an underdense plasma, i.e. $n_e \ll n_c$, is given by

$$N_e = \left(1-\frac{n_e}{n_c}\right)^{1/2} \simeq 1 - \frac{1}{2}\frac{n_e}{n_c}, \tag{4.14}$$

where n_e is the plasma electron density, $n_c = \pi/r_e\lambda_{pr}^2$ is the critical density, $r_e = e^2/m_e c^2$ is the classical electron radius, and λ_{pr} is the wavelength of the probe laser. Assuming that the interaction length is approximately a plasma length L_p produced in the gas-jet, the phase difference is calculated as

$$\Delta\phi \simeq -\pi\frac{L_p}{\lambda_{pr}}\frac{\delta n}{n_c}, \tag{4.15}$$

where $\delta n = n(t+T) - n(t)$ is the density difference between the time t and $t+T$ at the focus point.

Since the density perturbation oscillates as

$$\sin[\omega_p(t+T)] - \sin(\omega_p t) = 2\sin(\omega_p T)\sin\left(\omega_p t + \frac{\omega_p T}{2} + \frac{\pi}{2}\right), \tag{4.16}$$

the measured phase difference is maximized in the case where the time separation of the two probe pulses is $T = nT_p/2, n = 1,3,\cdots$, where $T_p = 2\pi/\omega_p$ is the period of the electron plasma wave. Thus the amplitude sensitivity factor[44][45] due to the mismatch of the time separation is

$$S_t = 2\sin(\omega_p T) = 2\sin(2\pi T/T_p). \tag{4.17}$$

The finite temporal and spatial widths of the probe pulses cause averaging of the phase shift reducing the amplitude. Estimates of the sensitivity factors due to averaging effects can be obtained for a Gaussian intensity profile of the probe pulse with a temporal rms width σ_{zpr}/c and a radial rms width σ_{rpr}. The temporal sensitivity factor is

$$S_z = \frac{\int \cos(\omega_p t)\exp(-c^2t^2/2\sigma_{zpr}^2)dt}{\int \exp(-c^2t^2/2\sigma_{zpr}^2)dt} = \exp\left(-\frac{\sigma_{zpr}k_p}{2}\right), \tag{4.18}$$

and the spatial sensitivity is

$$S_r = \frac{\int (1-\frac{r^2}{\sigma_r^2})\exp(-\frac{r^2}{\sigma_r^2})\exp(-\frac{r^2}{2\sigma_{rpr}^2})dr}{\int \exp(-\frac{r^2}{2\sigma_{rpr}^2})dr} = \frac{1+(\sigma_{rpr}/\sigma_r)^2}{(1+2(\sigma_{rpr}/\sigma_r)^2)^{3/2}}, \tag{4.19}$$

where σ_r is the rms radius of the pump pulse. Thus the measured phase difference is given by

$$(\Delta\phi)_m = -\pi S_t S_z S_r \frac{L_p}{\lambda_{pr}} \frac{\delta n}{n_c}. \tag{4.20}$$

4.2.2 Measurement of the Plasma Electron Oscillation and the Phase of the Plasma Wave

The experimental setup of the FDI is shown in Fig. 4.9. The 2.6 TW 10 Hz Ti:sapphire laser pulse at a wavelength of 800 nm with a maximum energy of 135 mJ and a duration of 52 fs (FWHM) is split into two beams. The reflected beam (80%) is used as the pump pulse and the transmitted beam as the probe beam, which is frequency doubled with a BBO crystal and transported into a Michelson-interferometer to make two collinear pulses with an adjustable time delay. The time delay between the pump and the probe pulses is adjusted with a delay line. The probe beam is combined collinearly with the pump beam by transmission through a dichroic beam splitter reflecting the pump beam. The pump and probe pulses are focused by an off-axis parabolic mirror with a focal length of 15 cm. The focal spot images taken with a CCD camera show that the pump focused intensity profile is approximately a Gaussian distribution with a rms radius (at $1/e$) $\sigma_r = 8.9$ μm, while the probe beam radius is $\sigma_{rpr} = 3$ μm and centered on the pump beam. The peak pump intensity is 8.4×10^{17} W/cm^2 ($a_0 \simeq 0.6$), producing fully ionized He gas in the focal region. The probe beam is separated from the pump beam with a dichroic beam splitter after passing through the plasma and guided through an optical fiber into the spectrometer to analyze the interferograms. A part of the probe beam is sent directly to the spectrometer to make the reference fringes. The spectrometer is a Czerny-Turner type with a focal length of 1.33 m and a grating of 1800 gr/mm. The spectral resolution is 0.06 Å.

The phase shift $\Delta\phi$ is obtained from the difference of the peak position between the interferograms of the probe and the reference, shown in Fig. 4.10. The phase shift is calculated from the peak of the correlation function between the probe and reference spectrum using a spectral analysis technique[57]. The correlation function $C(Y_1, Y_2)$ between two spectra $Y_1 = f(\omega)$ and $Y_2 = g(\omega)$ is defined as

$$C(Y_1, Y_2)(\omega') = \int_{-\infty}^{\infty} f(\omega+\omega')g(\omega)d\omega. \tag{4.21}$$

The function $C(Y_1, Y_2)$ becomes a maximum for the frequency $\omega' = \Delta\phi/T$. The correlation function is calculated using the Fourier transform:

$$C(Y_1, Y_2)(\omega') = \mathcal{F}^{-1}[\mathcal{F}[f]\mathcal{F}[g]], \tag{4.22}$$

where $\mathcal{F}$ denotes the Fourier-transform. Figure 4.11 shows the correlation function for the two spectra of the probe and the reference interferograms. We obtain the phase difference $(\Delta\phi)_m$ from the peak frequency ω'_{pk} of the correlation function.

In this experiment, the time separation was adjusted to 720 fs ($\sim 5.5T_p$), which was obtained from the fringe period of the frequency-domain interferogram shown in Fig. 4.10. The time separation T is given by $T = \lambda_{pr}^2/(c\Delta\lambda)$, where $\lambda_{pr} = 400$ nm is the wavelength of the probe laser and $\Delta\lambda = 0.74$ nm is the fringe period of the reference interferogram in the spectrum. The time delay between the pump and the probe pulses was varied from -1.5 ps to 3.1 ps with a time step of 6.7 fs to scan the

density oscillation of the wake excited by the pump pulse. The phase shift at each position was obtained by averaging 50 shots of the phase shift data to reduce pulse-to-pulse fluctuations. The gas-jet was operated at a backing pressure of 10 atm for He gas. The pump pulse was focused 1.5 mm below the end of the nozzle where a fully ionized plasma was expected with an electron density of 7.2×10^{17} cm^{-3} from the neutral gas density measurements.

In Fig. 4.12 (a), no phase shift was observed for the region where the two probe pulses were located before the pump pulse. This means that no wakefield is excited before the pump pulse passes through the gas-jet. In the region where the probe pulse was delayed after the pump pulse, a large amplitude density perturbation excited by the pump pulse was detected as indicated by the phase shifts shown in Fig. 4.12 (b) to (g). In the measurement shown in Fig. 4.12 (b) and (c), the first probe pulse traveled before the pump pulse and the second one after it. For this measurement, the sensitivity factor S_t is a half of that for the measurements shown in (d) to (g) in the region where both probe pulses travel after the pump pulse. From these phase shift data, the period and the amplitude of the electron density oscillation and the amplitude of the longitudinal wakefield are obtained as a function of time delay between the pump and probe pulses

Figure 4.13 shows the plasma density that is calculated from the oscillation periods of the plasma waves. The oscillation period of the electron plasma wave is 130 ± 3.4 fs behind the pump. This plasma wave period corresponds to the electron density of $7 \times 10^{17} \pm 8.5 \times 10^{15}$ cm^{-3} in linear wakefield theory, which is in good agreement with the electron density for the fully ionized He gas expected from the neutral gas density measurements.

The wakefield can be calculated from the sensitivity factor and the plasma density oscillation. The sensitivity factor $S_t \cdot S_z \cdot S_r$ is 0.46 for the measurements shown in Fig. 4.12 (b), (c), and 0.92 for those in Fig. 4.12 (d) - (g), with $k_p\sigma_z = k_p\sigma_{zpr} = 1.06$, $k_p\sigma_r = 1.44$, and $k_p\sigma_{rpr} = 0.48$. Figure 4.14 shows the amplitude of the electron density oscillation and the amplitude of the longitudinal wakefield as a function of a time between the pump and probe pulses. The amplitudes of the density perturbation and the longitudinal wakefield quickly damp in a time of $1.7T_p$ just after the pump pulse. Afterward their amplitudes attenuate slowly with a damping time of $8T_p$. The fast damping of the wakefields may be caused by the trapping and loading of electrons from the plasma. The slow damping may be induced by the non-uniformity of the plasma density distribution in the gas-jet. The measured density perturbation before damping is $(\delta n/n_e)_m \simeq 0.74$ with the plasma length $L_p = 1$ mm. The maximum longitudinal wakefield of 20 GV/m is deduced by Eq. (2.45). These estimates are in good agreement with the density perturbation $(\delta n/n_e)_{th} = 0.75$ and the longitudinal wakefield of 21 GV/m calculated by linear wakefield theory. Figure 4.15 shows the electric field of Fig. 4.12(b).

We compare the experimental and 1D Particle-in-Cell (PIC)[58] simulation results. The result of PIC simulation is obtained by solving the Maxwell equation, the equation of motion, the plasma fluid equation and the integral of difference equations (see appendix A). Figure 4.16(a) shows the simulation result on the longitudinal wakefield as a function of time for a_0=1, the laser pulse width of 50 fs, the laser wavelength of 800 nm, and the plasma density distribution of Fig. 4.16(b). The wakefield decreases with time in Fig. 4.16(a). The damping time of 11 T_p corresponds the experimental result. It is shown that the damping of wakefields results from the non-uniformity of the plasma density distribution.

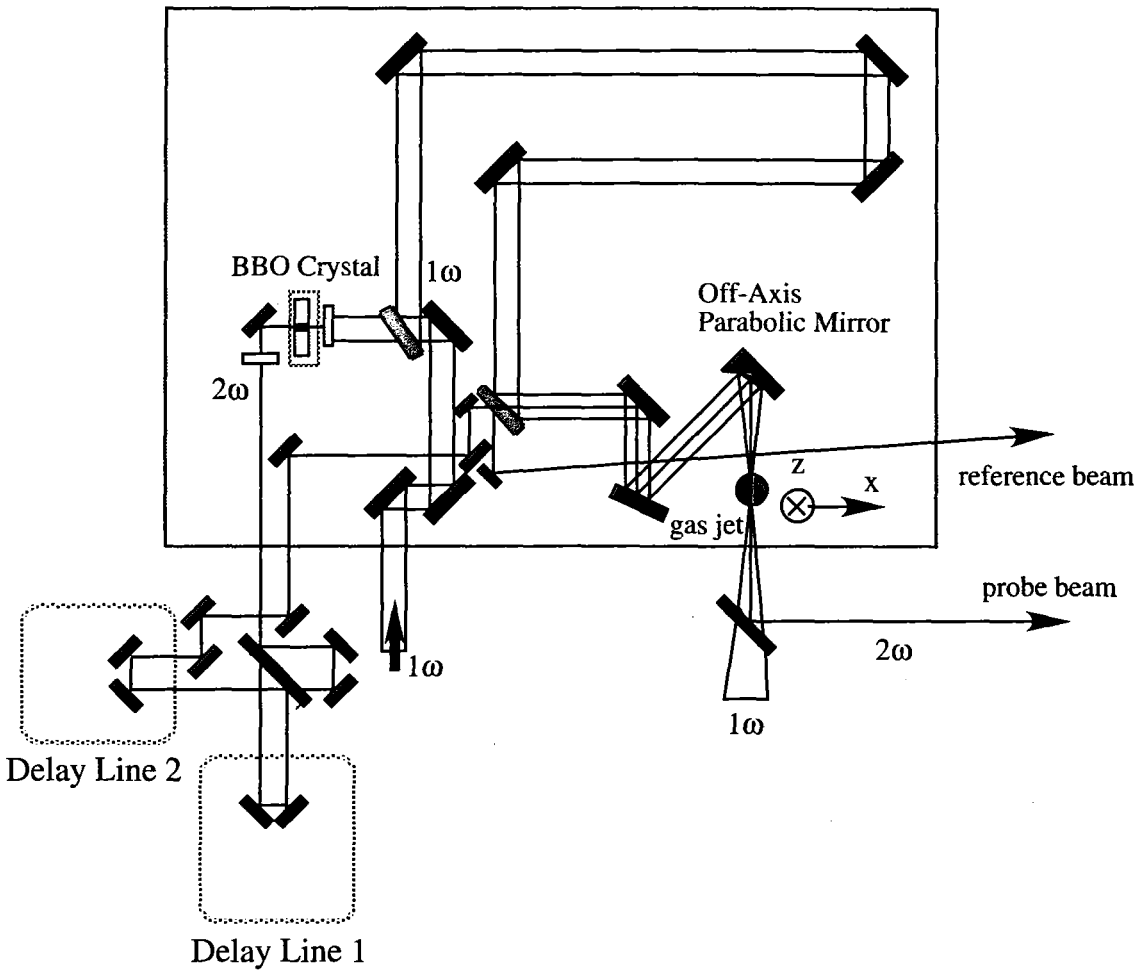

Figure 4.9: Experimental setup of the frequency domain interferometry. The delay line 1 adjusts the time delay between two collinear probe pulses and the delay line 2 the time delay between the pump and probe pulses.

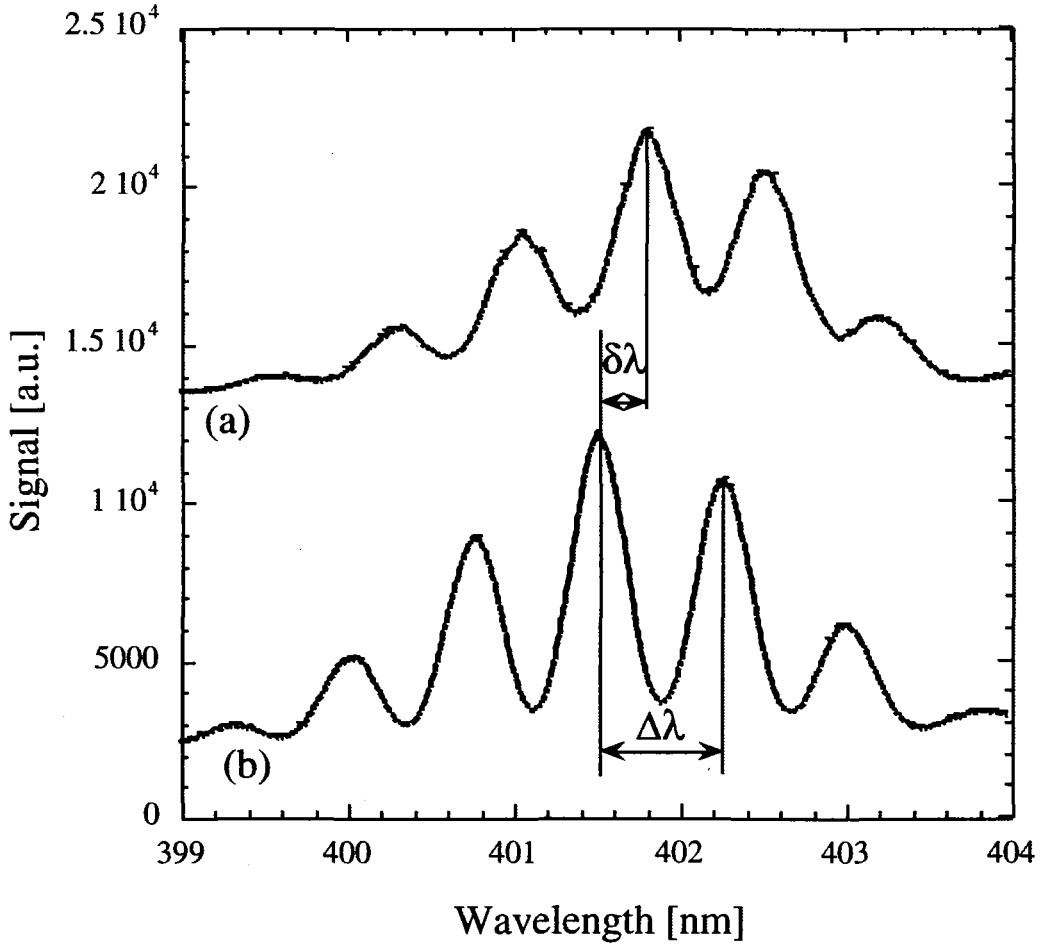

Figure 4.10: The interferograms obtained from (a) the probe pulses and (b) the reference pulses. The fringe separation is given by $\Delta\lambda = \lambda^2/(cT)$, where T is the time separation between the two probe pulses. The phase difference between the probe and the reference interferograms is calculated by $\Delta\phi = 2\pi\delta\lambda/\Delta\lambda$.

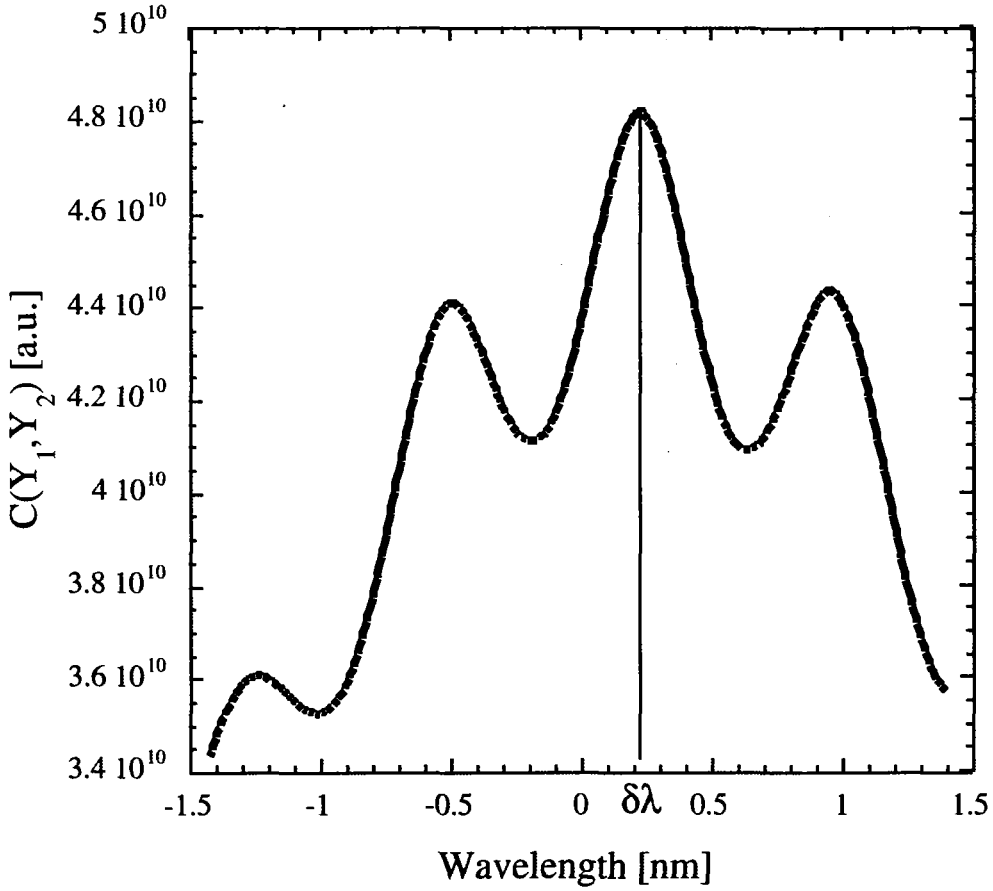

Figure 4.11: The correlation function calculated from the two spectra of the probe and the reference interferograms. The correlation function peaks at the frequency corresponding to the phase shift between the two spectra.

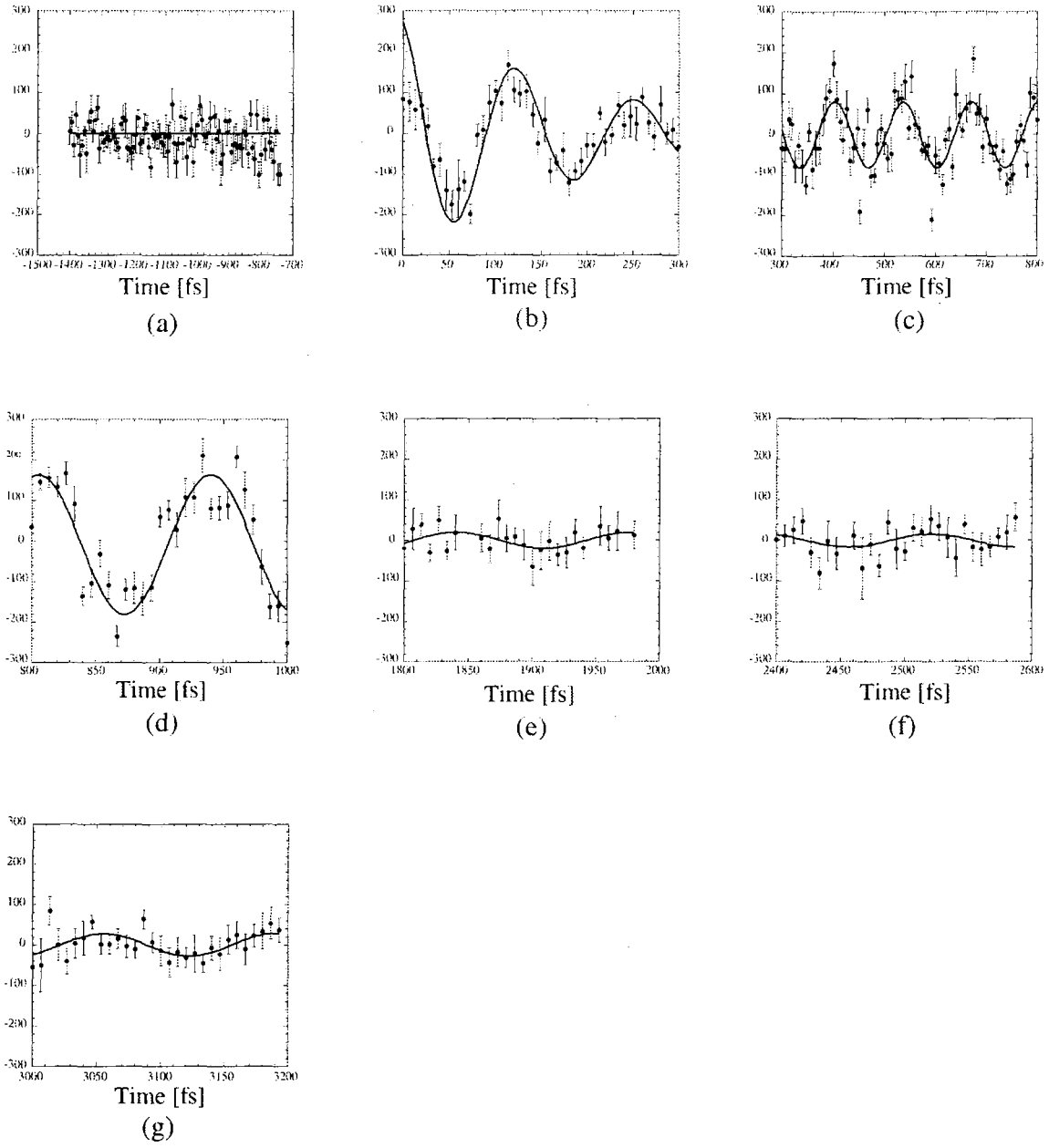

Figure 4.12: The relative phase shift as a function of the time delay for the measurement of the plasma density oscillation in the gas-jet operated at a backing pressure of 10 atm. (a) is measured in the case of the two probe pulses before the pump, (b) and (c) in the case of the first probe pulse before the pump and the second after the pump, and (d) to (g) in the the case of the two probe pulses after the pump.

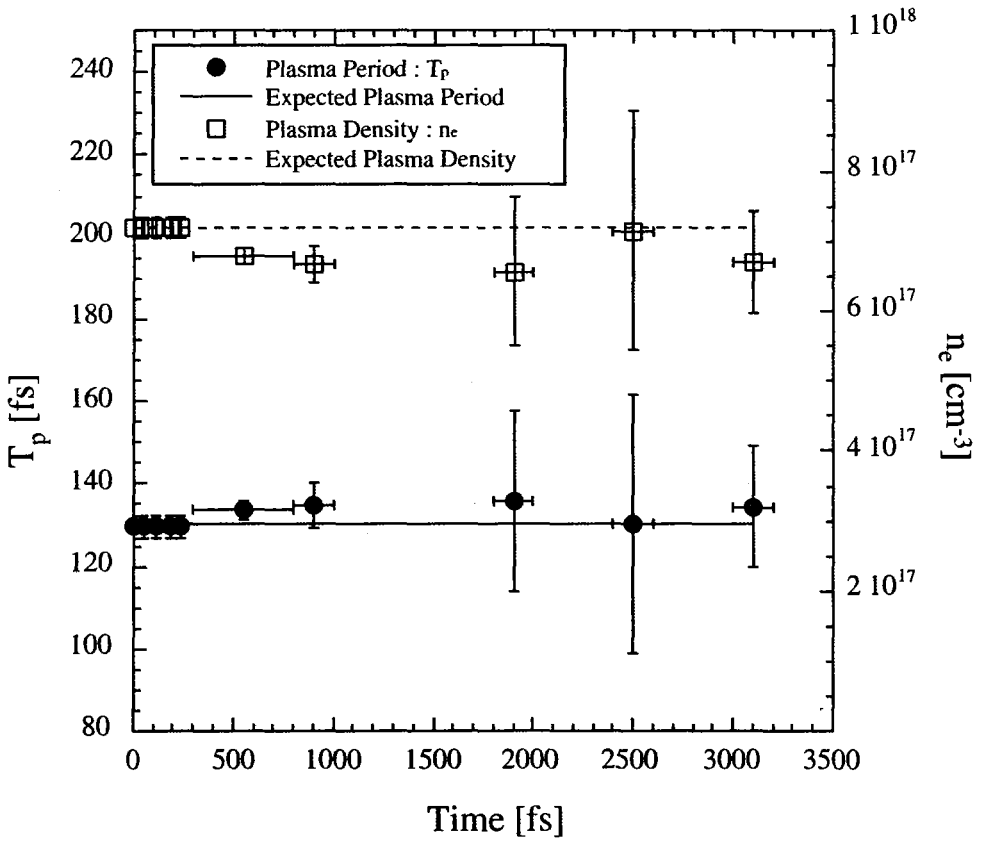

Figure 4.13: The period of the electron density oscillation and the plasma density as a function of time between the pump and probe pulses. The solid and dotted line show the expected plasma period and density from the gas density measurement, respectively.

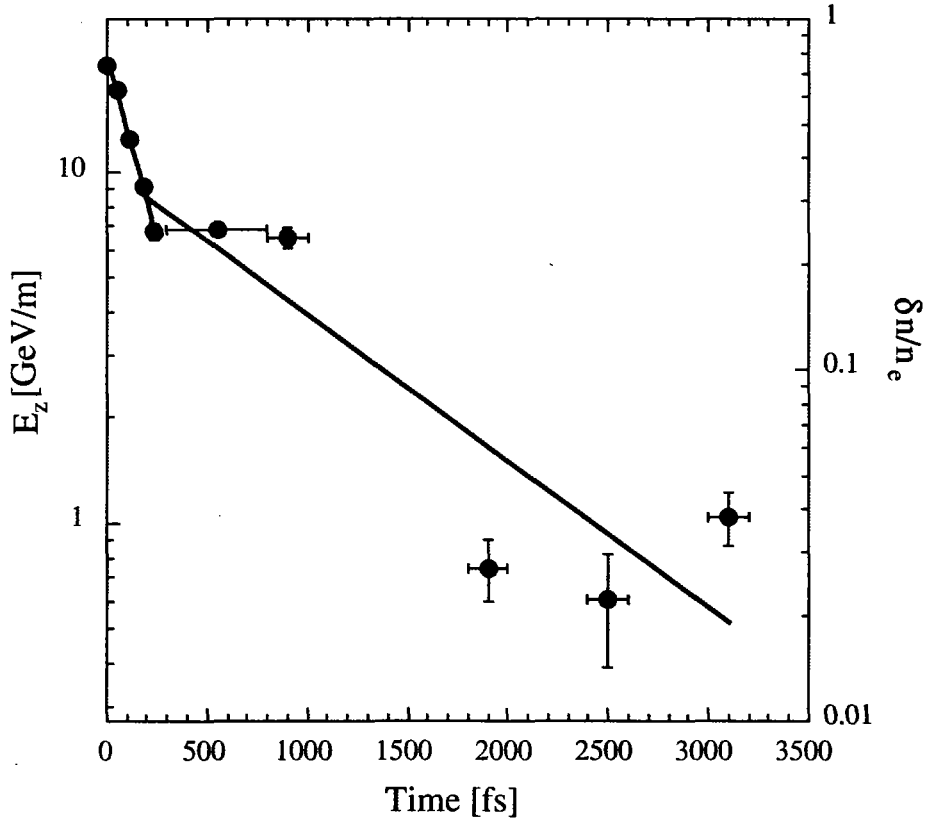

Figure 4.14: The amplitude of the electron density oscillation and the amplitude of the longitudinal wakefield as a function of the time between the pump and probe pulses. The solid lines are exponential fits to the data with a damping time of $1.7T_p$ and $8T_p$.

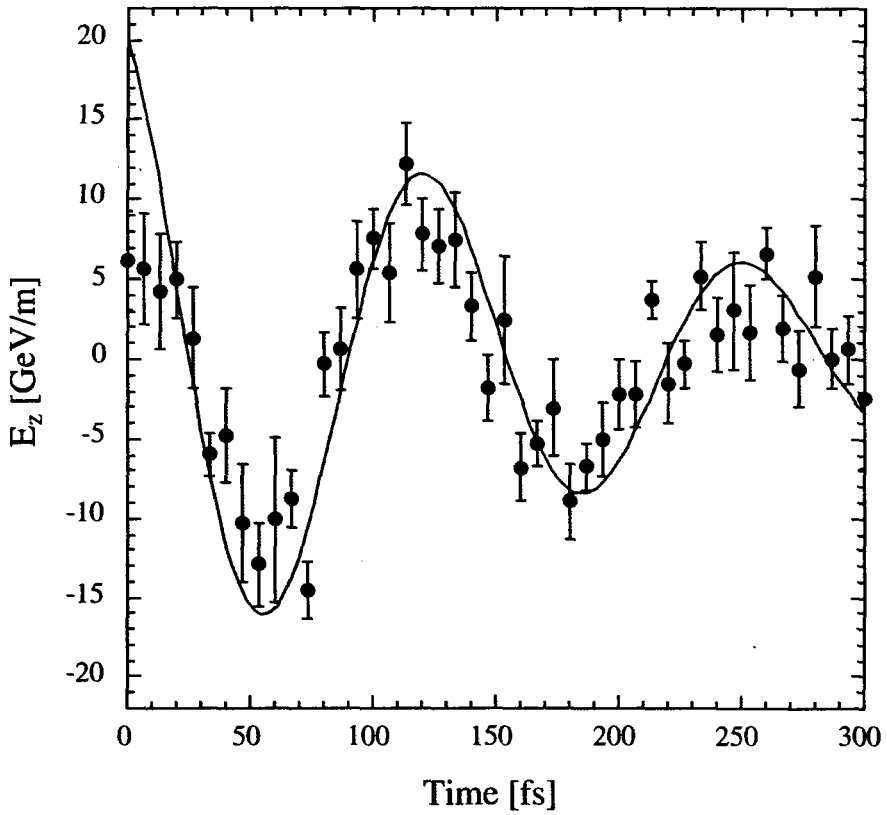

Figure 4.15: The amplitude of the longitudinal wakefield obtained from the plasma electron density oscillation and the sensitivity factor. A 20 GV/m wakefield has been observed.

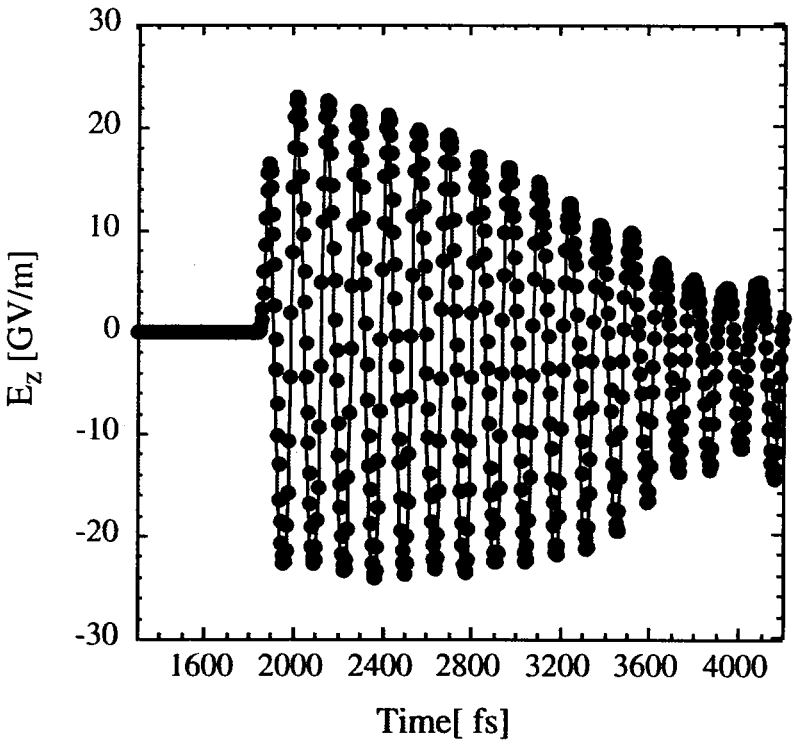

(a)

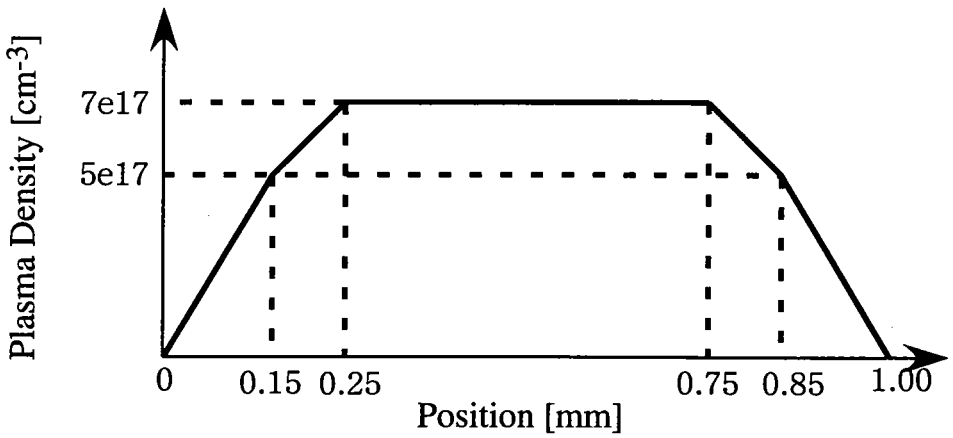

(b)

Figure 4.16: (a)The simulated result of the longitudinal wakefield as a function of time by the PIC code for the laser strength parameter a_0 of 1. (b) The plasma density distribution.

5. Acceleration of Electron Beams in Laser-produced-plasma

We present the numerical simulation of high quality electron beam acceleration based on the anomalous blueshift effect and FDI technique. The trapped phase space of the wakefield, where the accelerating and focusing forces are exerted on particles, extends a quarter of the plasma wavelength in longitudinal space and half of the laser spot size in transverse space, which are typically less than 100 fs temporally and 10 μm radially, respectively.

Presently there are three major schemes: nonlinear wave-breaking injection[35], transverse optical injection[36], and colliding pulse optical injection[37][38]. No proof-of-principle experiment for these schemes has been yet performed because of experimental difficulties. Nonlinear wave-breaking injection uses one pump laser pulse. Figure 5.1(a) shows a schematic of transverse optical injection. Transverse optical injection uses two laser pulses; one pump pulse and one injection pulse. The two pulses cross at a focal point. Figure 5.1(b) shows a schematic of colliding pulse optical injection. Three laser pulses consisting of a pump pulse for wakefield excitation and two injection pulses for trapping the electrons in plasma make up a colliding optical injector.

For colliding pulse optical injection into a wakefield excited by the pump pulse, a frequency difference between the two injection pulses is needed. We can produce the frequency shifted pulse using the anomalous blueshift effect. The three pulses propagate through plasma collinearly. We demonstrate the optical injection scheme using 1D Particle-in-Cell (PIC) simulations[58] (see appendix A).

5.1 Motion of Electrons in a Plasma Wave

The motion of electrons in a plasma wave can be represented by a phase-space diagram as shown in Fig. 5.2(a). The horizontal axis shows the longitudinal speed-of-light-frame $\zeta = z - v_p t$. Electrons inside the bounded region, known as separatrix, are "trapped" by the plasma wave and carried along at the same wavelength as the plasma wave. Electrons above and below this bounded region are "untrapped". Electrons in plasma are below the separatrix due to the low energy. When an electron is below the separatrix initially, it gains and loses energy quickly due to the slow electron velocity, the electron moves in the opposite direction of the plasma wave, and never has an energy higher than that corresponding to the phase velocity of the plasma wave. On the other hand, when an electron is inside the separatrix, it can move to the top of the separatrix and gain significant energy. This is the process of electron acceleration in a plasma wave. As a result, the bottom and top of the separatrix determine the minimum trapping threshold γ_{min} and the maximum electron energy γ_{max} attainable, respectively, for a given plasma wave amplitude. They are given by[59]

$$\gamma_{min} = \gamma_p(1 + \gamma_p\Delta\phi) - \gamma_p\beta_p[(1 + \gamma_p\Delta\phi)^2 - 1]^{1/2}, \tag{5.1}$$

$$\gamma_{max} = \gamma_p(1 + \gamma_p\Delta\phi) + \gamma_p\beta_p[(1 + \gamma_p\Delta\phi)^2 - 1]^{1/2}, \tag{5.2}$$

where

$$\Delta\phi = 2\beta_p[(1 + \epsilon^2/2)^2 - 1]^{1/2}, \tag{5.3}$$

$\epsilon = E_{max}/E_0$ is given by the plasma-wave amplitude, and E_0 is the non-relativistic cold wave-breaking limit in Eq. (2.17). The normalized energy γ is defined

$$\gamma = \frac{E_{total}}{m_e c^2} = \frac{1}{\sqrt{1 - \beta^2}}, \tag{5.4}$$

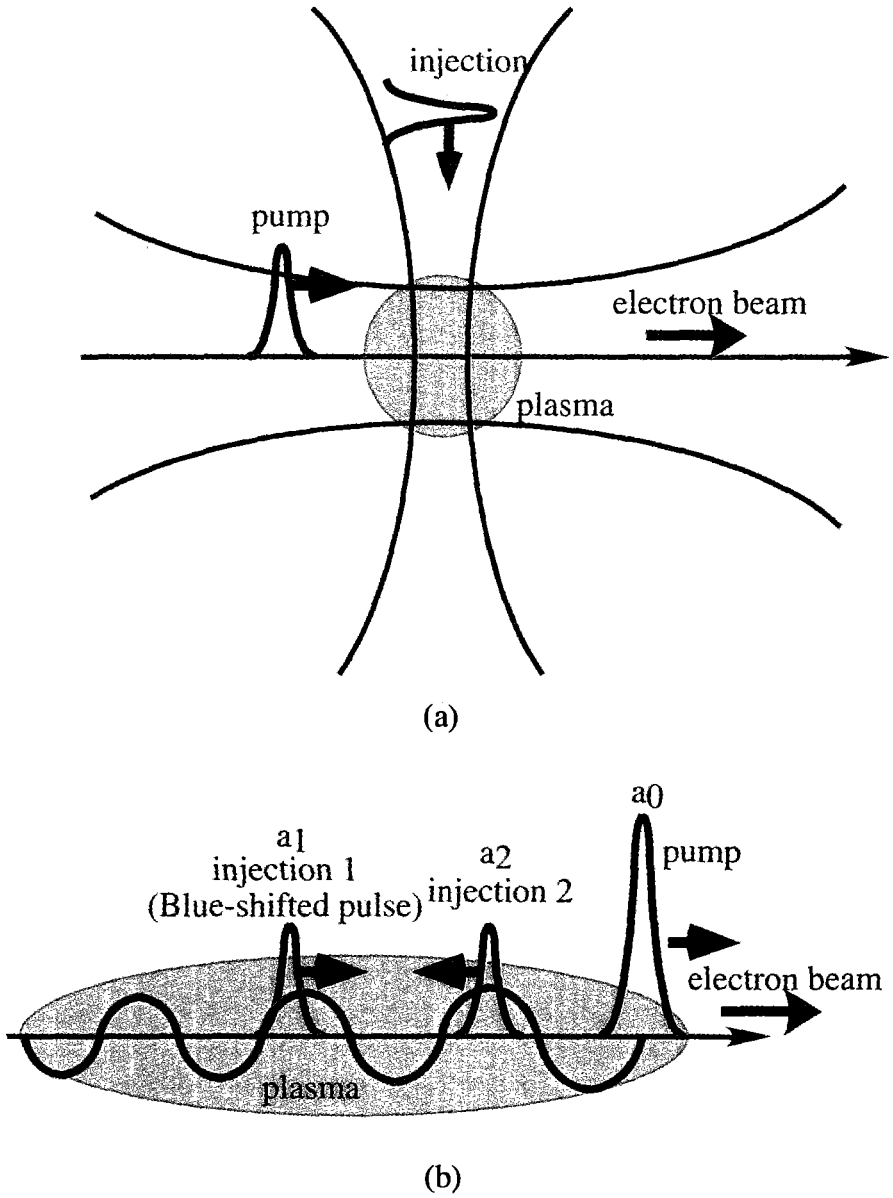

Figure 5.1: (a) A schematic of transverse optical injection. A radial wakefield due to the injection pulse injects electrons into a longitudinal wakefield due to the pump pulse. (b) A schematic of colliding pulse optical injection. The laser pulse of injection 1 is an anomalous blue-shifted pulse.

where E_{total} is the total energy of an electron and β is the normalized velocity of an electron. The normalized velocity β is given by

$$\beta = \frac{v_e}{c}, \tag{5.5}$$

where v_e is the electron velocity. γ_p is the normalized energy of the plasma-wave phase velocity, and $\beta_p = v_p/c$ is the normalized phase velocity. The actual trapping threshold for each electron depends on its position (phase) in the plasma wave at injection. The maximum electron energy attainable in a plasma wave increases with the plasma-wave amplitude limited by wave breaking. The wave-breaking limit is defined by the point at which the plasma wave traps the bulk of electrons that constitute the plasma wave itself and thus self-destructs. In a cold plasma, the maximum plasma-wave amplitude is given by[60]

$$E_{max} = E_0\sqrt{2(\gamma_p - 1)}, \tag{5.6}$$

and the maximum electron energy is

$$\gamma_{max} = 4\gamma_p^3 - 3\gamma_p. \tag{5.7}$$

For a higher plasma temperature, the wave-breaking limit is lowered, due to trapping of hot bulk electrons at a lower plasma-wave amplitude. For a plasma wave with an amplitude below the wave-breaking limit, it can trap hot electrons that are at the tail of a Maxwellian distribution of a thermal plasma, or that are preheated to exceed the trapping threshold by other mechanisms, or that are injected externally. In this case, these trapped electrons are accelerated and thus take energy away from the plasma wave, resulting in damping of the plasma wave. This is referred to as electron beam loading or nonlinear Landau damping. In fact, untrapped electrons can also gain energy (as seen in Fig. 5.2(a)) and damp the wave.

5.2 Principle of Colliding Pulse Optical Injection

In Fig. 5.1(b), an intense pump pulse denoted by subscript 0, a forward going injection pulse denoted by subscript 1, and a backward going injection pulse denoted by subscript 2. The frequency, wave number, and normalized intensity are denoted by ω_i, k_i, and a_i $(i = 0, 1, 2)$, respectively. Furthermore, $\omega_1 = \omega_0 + \Delta\omega$ $(\Delta\omega \geq 0)$, $\omega_2 = \omega_0$, and $\omega_0 \gg \Delta\omega \gg \omega_p$ are assumed such that $k_1 \simeq k_0$ and $k_2 = -k_0$. The pump pulse generates a fast wakefield. When the injection pulses collide, they generate a slow ponderomotive beat wave with a phase velocity v_p. The phase velocity v_p is given by

$$v_p = \frac{\omega_1 - \omega_2}{k_1 - k_2} = \frac{\Delta\omega}{2k_0}. \tag{5.8}$$

During the time in which the two injection pulses overlap, a two-stage acceleration process can occur; i.e., the slow beat wave injects plasma electrons into the fast wakefield in Fig. 5.2(b).

The problems for the experiment of the optical injection are the timing between the pump pulse and the injection pulses, and the frequency difference of the injection pulses. The wakefield excited in the gas-jet has an ultra-high gradient with good coherency and can be used for particle accelerators (see chapter 4). In the optical injection schemes, provided that the probe pulses are replaced with the injection pulses, the FDI system to measure the wakefield will be modified into the optical injection system for the laser wakefield. In order to make a frequency difference $\Delta\omega$ between two injection pulses, the anomalous blue-shifted pulse is used as a forward going injection pulse (see chapter 3).

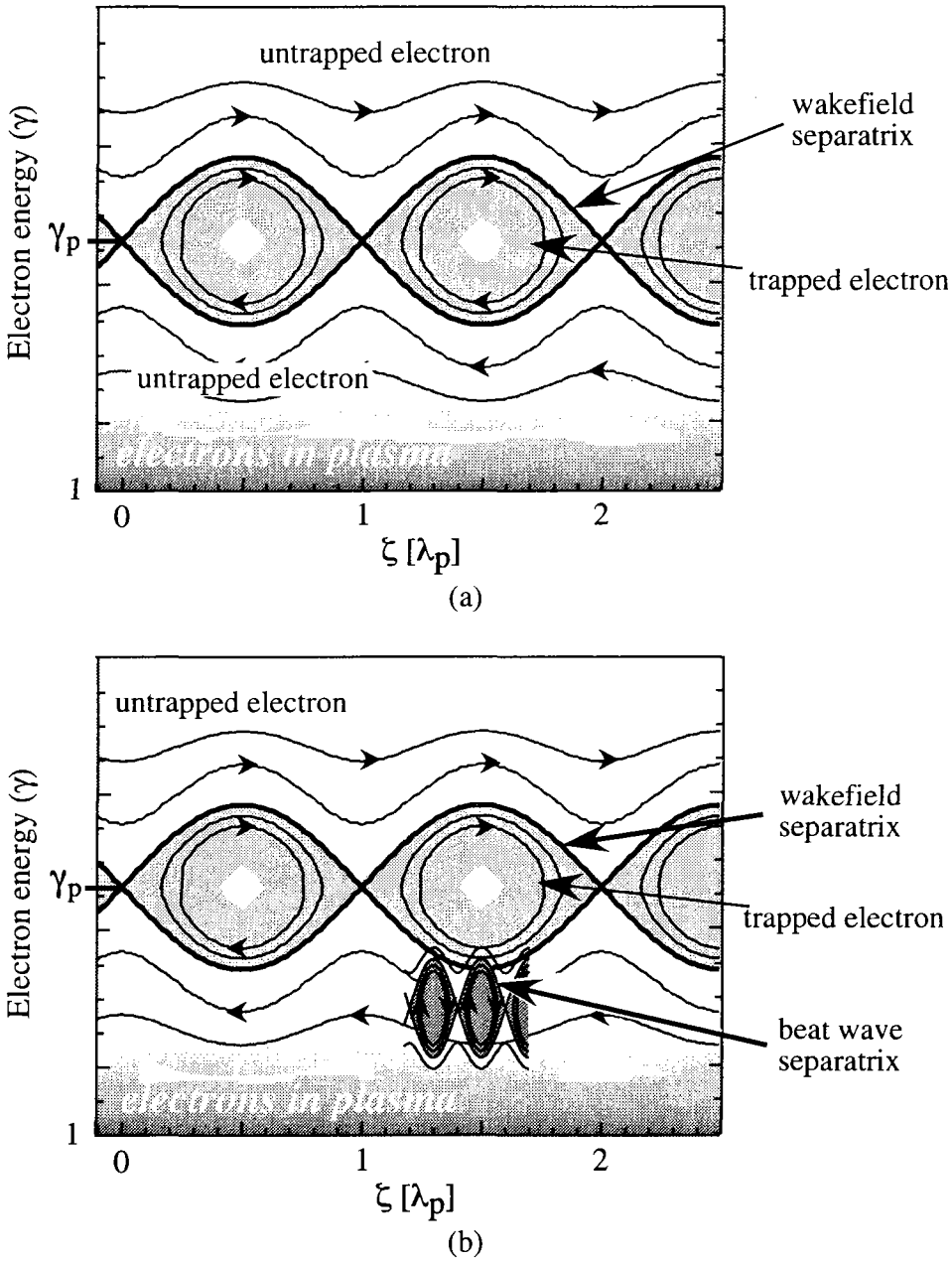

Figure 5.2: Phase-space trajectories for electrons in a plasma wave excited by (a) single laser pulse and (b) a pump pulse with two injection pulses. The horizontal axis shows the longitudinal speed-of-light-frame $\zeta = z - v_p t$ in unit of the plasma wavelength λ_p. Electrons above and below the separatrix are untrapped, while electrons within the separatrix are trapped by the wave. The motion of the electrons relative to the wave is indicated by the arrows.

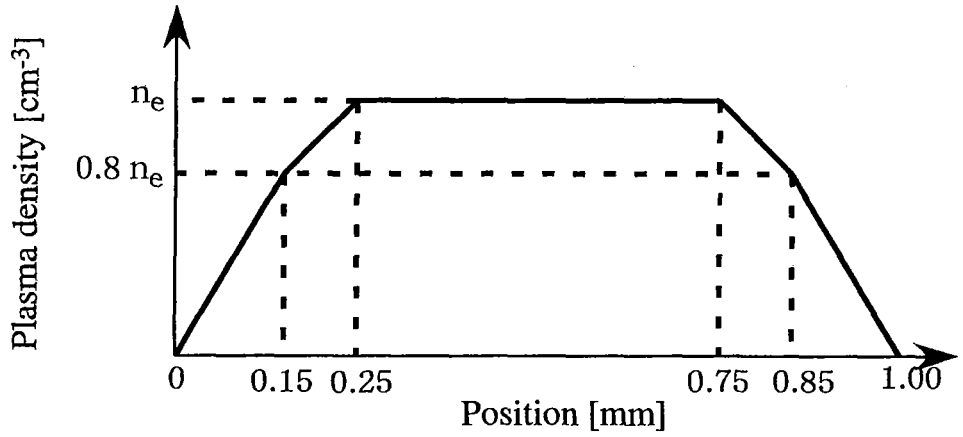

Figure 5.3: Plasma density distribution assumes for simulation of the optical injection.

5.3 Simulation Results of Optical Injection by an Intense Laser Pulse

5.3.1 Simulation Results of the Wave-breaking Optical Injection Scheme

We make a numerical simulation of the optical injection scheme for the plasma density distribution shown in Fig. 5.3 using a PIC code[58]. Figure 5.4 shows the results of the optical injection simulation for $n_e = 7 \times 10^{17}$ cm^{-3} as a function of a_0. In order to generate the electrons by the single pulse optical injection, the pump intensity a_0 should be larger than 1.5. The energy spread $\Delta E/E_{max}$ of accelerated electrons results in 100%, where E_{max} is the maximum energy of electrons. This scheme has disadvantage for generating a high quality electron beam with narrow energy spread.

5.3.2 Simulation Results of the Colliding Pulse Optical Injection Scheme

We performed a simulation of the colliding pulse optical injection scheme for $a_0 = 1$. We assume that the frequency upshift of the forward going injection pulse $\Delta\omega/\omega_0$ is set to be 6% from the anomalous blueshift experimental data in chapter 3. Figure 5.5 shows the results of the simulation at $n_e = 7 \times 10^{17}$ cm^{-3} for $a_0 = 1.0$ as a function of $a_1 = a_2$. These results indicate that electrons can be inject into the wakefield at the strength parameter larger than 0.3.

The accelerated energy and the energy spread are shown in Fig. 5.6 as a function of the plasma density. The accelerated energy increases with the plasma density. Nevertheless, the energy spread is the smallest at $n_e = 7 \times 10^{17}$ cm^{-3}.

The electron distribution in a phase space and the energy spectrum for $a_0 = 1.0$ and $a_1 = a_2 = 0.3$ at $n_e = 7 \times 10^{17}$ cm^{-3} are shown in Figs. 5.7(a) and (b), respectively. A part of electrons in plasma is trapped and accelerated in the wakefield excited by the pump pulse. The pulse shape and the energy spectrum of the accelerated electron beam are shown in Figs. 5.8(a) and (b), respectively. The accelerated electron beam has the pulse width of 7.7 fs (rms), the peak energy of 7.5 MeV with the energy spread of 3% (rms) from these figures. Assuming the electron beam radius of 15 μm, the accelerated electron charge becomes 26 pC corresponding to the peak current of the electron beam of 1.3 kA. It could be difficult to generate such an ultrashort intense electron beam by means of the conventional RF accelerators.

Figure 5.9 shows the distribution of the transverse normalized velocities β_t of the accelerated

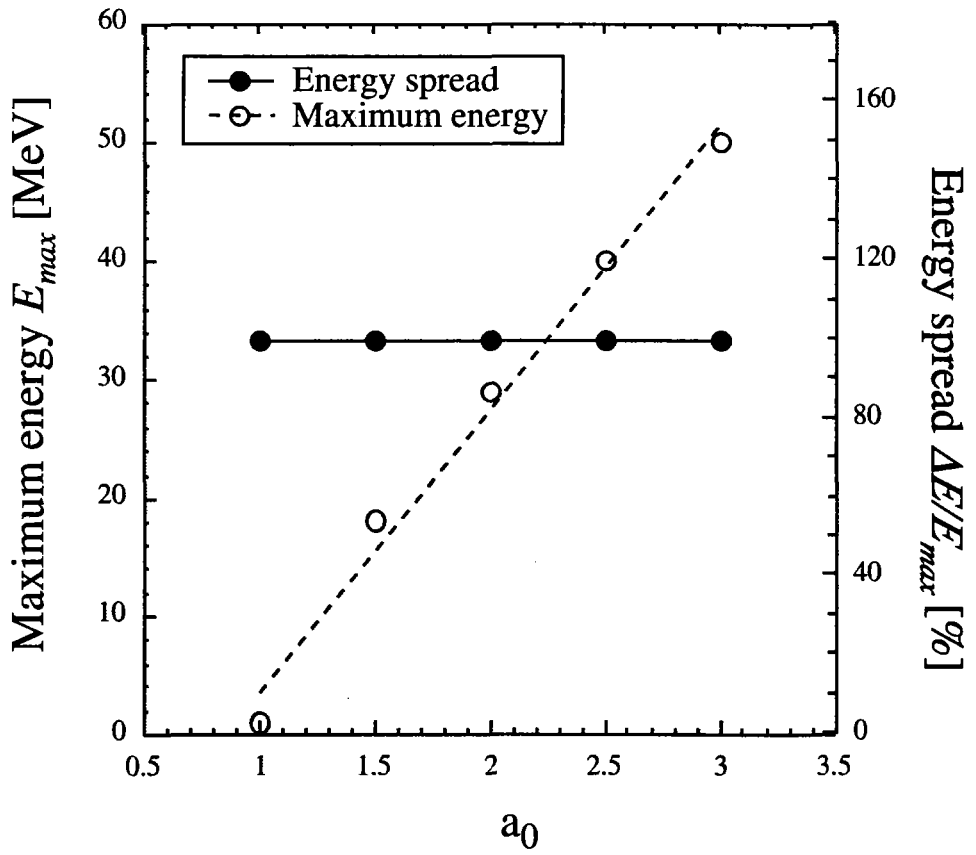

Figure 5.4: Results of the wave-breaking optical injection simulation for $n_e = 7 \times 10^{17}$ cm^{-3}. The horizontal axis shows the pump strength parameter a_0. The open circles and dotted line show the maximum energy E_{max}, and the closed circles and the solid line show the energy spread $\Delta E/E_{max}$.

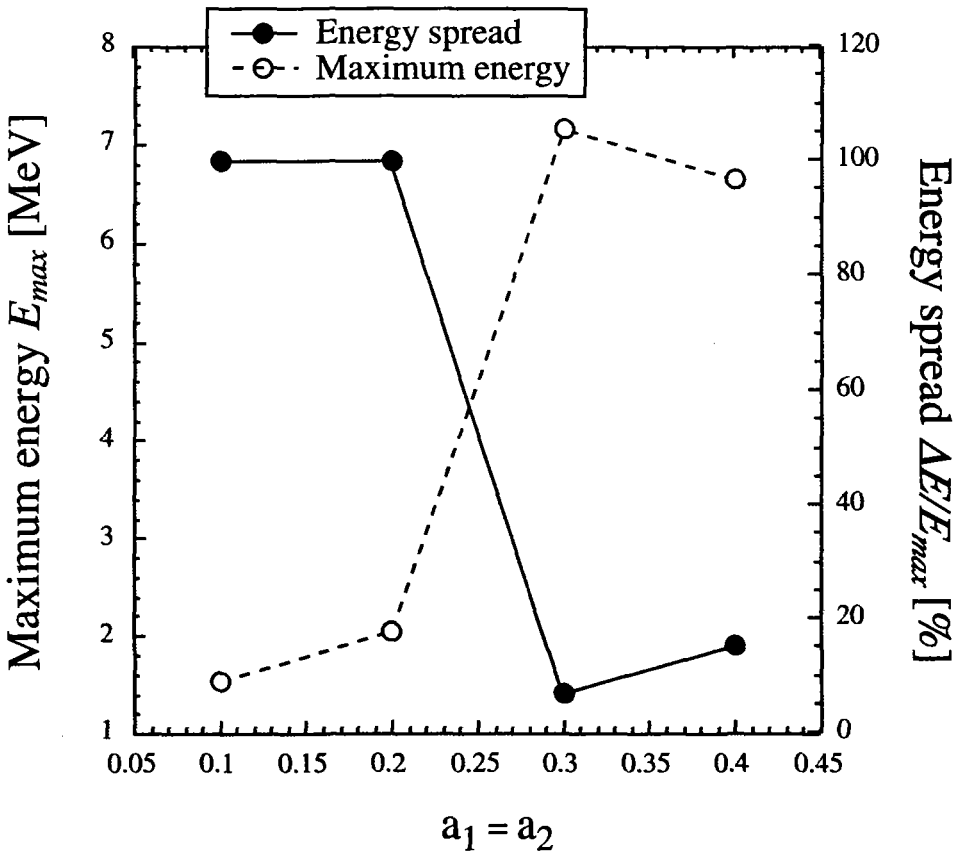

Figure 5.5: Results of the colliding pulse optical injection simulation for $a_0 = 1.0$ at $n_e = 7 \times 10^{17}$ cm^{-3}. The horizontal axis shows $a_1 = a_2$. The open circles and the dotted line show the maximum energy E_{max}, and the closed circles and the solid line show the energy spread $\Delta E/E_{max}$.

electrons. We can obtain an emittance of the electron beam from $\beta_t = 0.0064$. The un-normalized emittance ε_x of the electron beam is approximately equal to

$$\varepsilon_x = \pi r_b \beta_t, \tag{5.9}$$

where r_b is the electron beam radius. The normalized emittance ε_{nx} is

$$\varepsilon_{nx} = \gamma\beta\varepsilon_x, \tag{5.10}$$

where β is the longitudinal normalized velocity. For the electron energy of 7.5 MeV γ and β are approximately equal to 14.7 and 1, respectively. Assuming the electron beam radius, $r_b = 15$ μm, the normalized emittance of the accelerated electrons becomes 1 π mm mrad (rms). This emittance is comparable to that of best quality beam produced by the conventional RF accelerator technology such as a photocathode RF-gun[34][61].

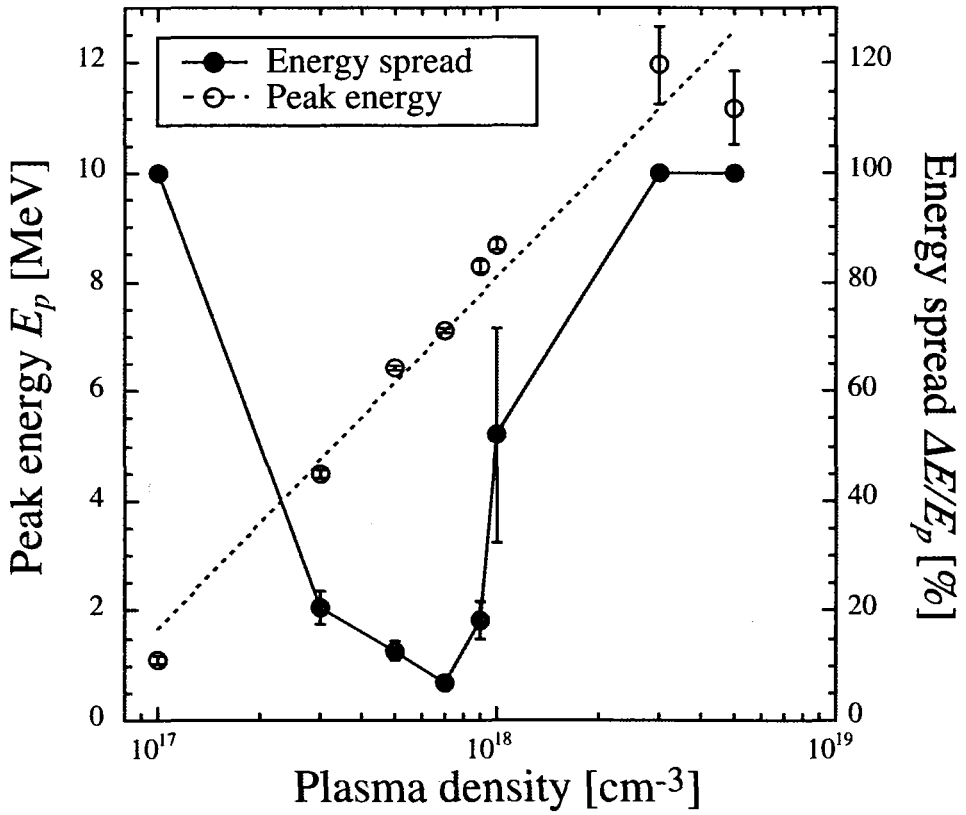

Figure 5.6: Results of the colliding pulse optical injection depends on n_e. The horizontal axis shows n_e in unit of cm^{-3}. The open circles and the dotted line show the peak energy E_p, and the closed circles and the solid line show the energy spread $\Delta E/E_p$.

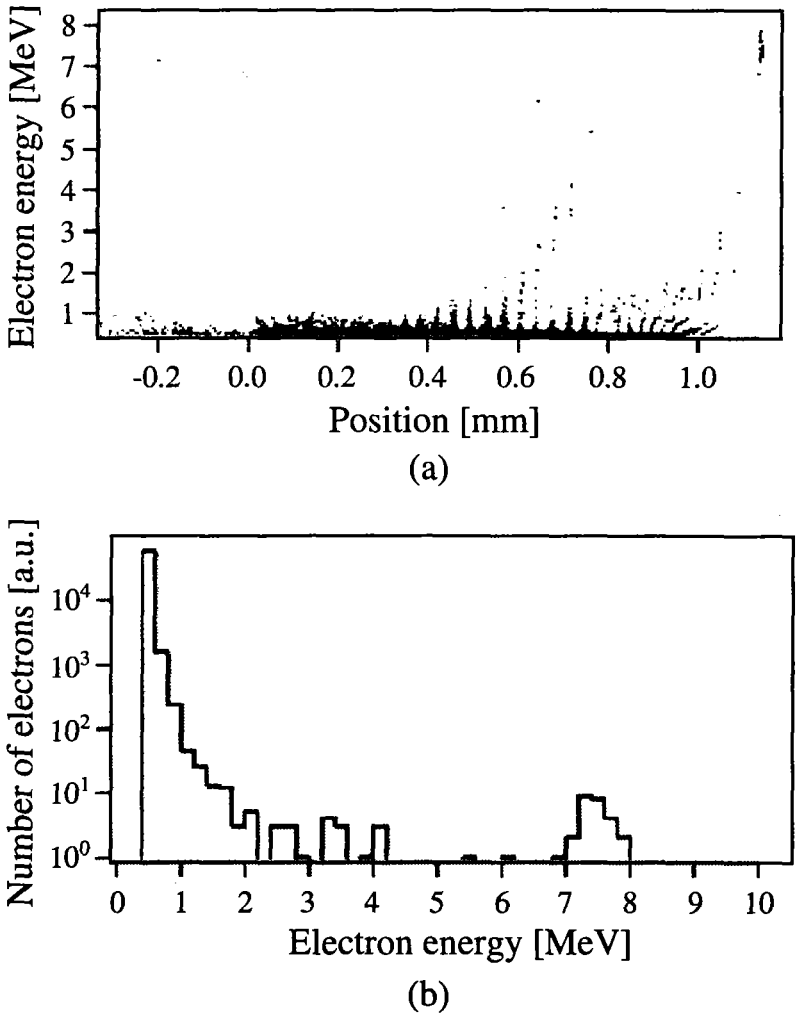

Figure 5.7: (a) The electron energy in phase space and (b) the energy spctrum of the colliding pulse optical injection simulation for $a_0 = 1.0$ and $a_1 = a_2 = 0.3$ at $n_e = 7 \times 10^{17}$ cm^{-3}.

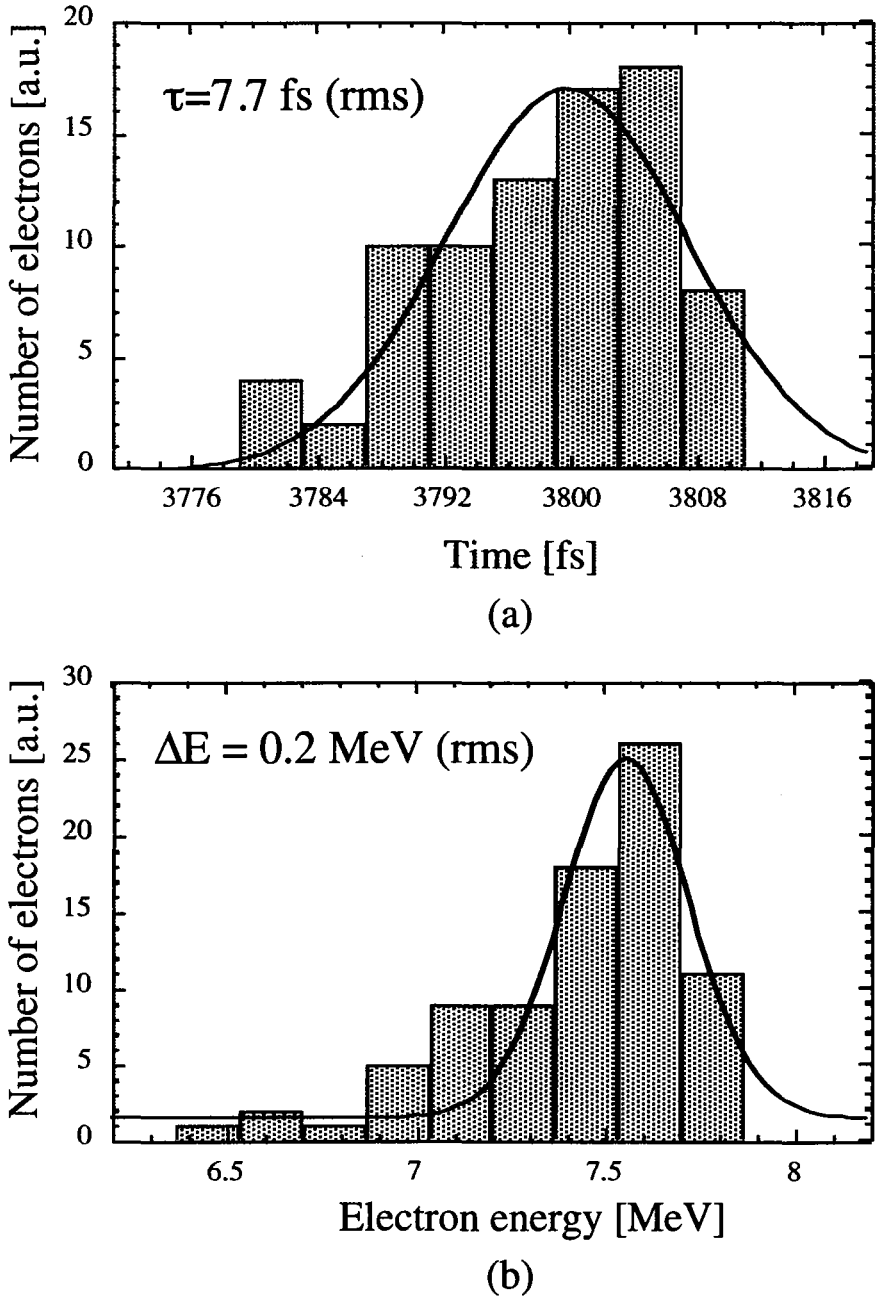

Figure 5.8: (a) The pulse shape and (b) the energy spectrum of the accelerated electrons for $a_0 = 1.0$ and $a_1 = a_2 = 0.3$ at $n_e = 7 \times 10^{17}$ cm^{-3}.

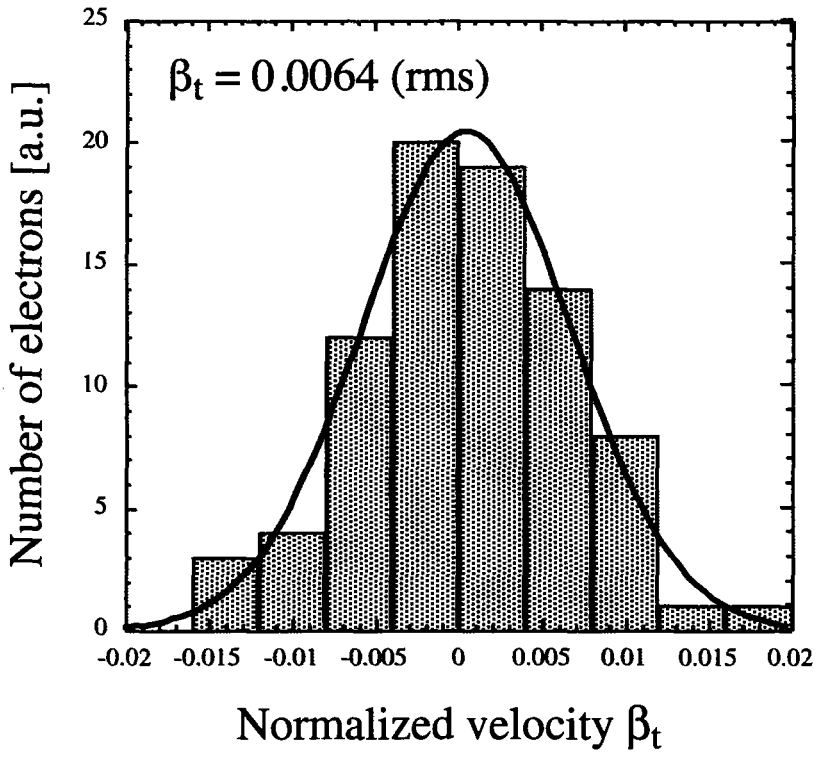

Figure 5.9: The distribution of the transverse normalized velocity β_t of the accelerated electrons for $a_0 = 1.0$ and $a_1 = a_2 = 0.3$ at $n_e = 7 \times 10^{17}$ cm^{-3}.

6. Conclusions

We have investigated the extraordinary nonlinear phenomena manifested via interactions of ultrashort laser pulses with gas and plasma; optical field ionization, ionization induced self-focusing and filamentation, an anomalous spectral shift and a large amplitude wakefield excitation. This study reveals that these phenomena occur in a consecutive strong field process through mutually correlated mechanism generated above a certain threshold intensity and that they can be controlled with femtosecond optical pulse technique in order to generate a relativistic bright electron beam with high quality in a laboratory table-top scale.

As a result of particular observations of nonlinear optical phenomena in strong field, we found the anomalous blueshift that shows a coherent frequency upshift of the whole laser pulse to a fixed frequency independent of the plasma density and the laser power. We clarify that this phenomenon results from a complex mechanism of the ultrafast optical field ionization and filamentation to cause acceleration of the whole laser photons due to a steep gradient of the refractive index change from neutral gas to plasma.

In the wakefield measurement, we have made the first direct observation of 20 GeV/m of coherent ultrahigh gradient wakefields excited by an intense ultrashort laser pulse in a gas-jet plasma. The experimental results agree with the 1D PIC simulation results and the linear theory. In the numerical simulations based on the results of these measurements, we verify generation of a relativistic electron beam accelerated by laser wakefields to be optically controlled with two colliding injection pulses of which one pulse can utilize a frequency up-shifted pulse due to the anomalous blueshift effect.

This synthetic study on laser wakefield excitation illuminates physical mechanisms of complex ultrafast nonlinear phenomena generated by interaction of ultraintense laser pulses with plasma and gives prospects of next generation particle accelerators for applications to a wide range of sciences; such as material science, nuclear science, high energy physics, chemical science, biological science, and medical science.

Acknowledgements

The work which went behind this dissertation was supported by a number of individuals. Those listed here are not nearly all. First and foremost, I would like to thank my wife Tomoko for her patience, assistance, and guidance over the past three years.

This work was supported by the Japan Atomic Energy Research Institute (JAERI) Advanced Photon Research Center (APRC). I would like to thank the members of the Laser Acceleration Research Group in APRC : Masaki Kando, Shinichi Masuda, Shuji Kondo, Shuhei Kanazawa, Takashi Yakoyama, and Toru Matoba. I would also like to thank the previous members of the Laser Acceleration Research Group in APRC : Hideki Dewa, Tomonao Hosokai, Fumio Sakai, and Hyeoung Ahn. Especially, I am very greatful to Masaki Kando. He supported every experiment and data analysis.

I would also like to thank the members of the experiment in this dissertation for their support : Takatsugu Oketa, Keisuke Nagashima, Hiroyuki Daido, Noboru Hasegawa, Kohta Sukegawa, Masayuki Suzuki, Kazuhito Yasuike, and Mamiko Nishiuchi.

I would also like to thank the previous and present superiors at JAERI-Kansai APRC : Hideo Ohno, Yoshiaki Kato, and Takashi Arisawa.

I would like to send special thanks to James K. Koga. He supported the data analysis. He checked my doctoral dissertation and paper.

Finally I would like to thank my boss Kazuhisa Nakajima. His guidance and motivation made this work possible. He checked every experiment, data analysis, and this dissertation.

Hideyuki Kotaki

References

[1] D. Strickland and G. Mourou, Opt. Commun., **56**, 219 (1985).

[2] C. P. J. Barty, T. Guo, C. Le Blanc, F. Raksi, C. Rose-Petruck, J. Squier, K. R. Wilson, V. V. Yakovlev, and K. Yamakawa, Opt. Lett., **21**, 668 (1996).

[3] K. Yamakawa, M. Aoyama, S. Matsuoka, T. Kase, Y. Akahane, and H. Takuma, Opt. Lett., **23**, 1468 (1998).

[4] K. Yamakawa and C. P. J. Barty, IEEE J. Select. Topics Quantum Electron., **6**, 658 (2000).

[5] L. V. Keldysh, Zh. Eksp. Teor. Fiz. **47**, 1945 (1964) [Sov. Phys. JETP **20**, 1307 (1965)].

[6] M. V. Ammosov, N. B. Delone, and V. P. Krainov, Zh. Eksp. Teor. Fiz. **91**, 2008 (1986), [Sov. Phys. JETP **64**, 1191 (1986)].

[7] E. Esarey, G. Joyce, and P. Sprangle, Phys. Rev. A **44**, 3908 (1991).

[8] S. C. .Wilks, J. M. Dawson, W. B. Mori, T. Katsouleas, and M. E. Jones, Phys. Rev. Lett. **62**,2600 (1989).

[9] B. M. Penetrante, J. N. Bardsley, W. M. Wood, C. W. Siders, and M. C. Downer, J. Opt. Soc. Am. B **9**, 2032 (1992).

[10] S. C. Rae, and K. Burnett, Phys. Rev. A **46**, 1084 (1992).

[11] W. M. Wood, G. B. Focht, and M. C. Downer, Opt. Lett. **13**, 984 (1988).

[12] S. P. LeBlanc, R. Sauerbrey, S. C. Rae, and K. Burnett, J. Opt. Soc. Am. B **10**, 1801 (1993).

[13] C. W. Siders, N. C. Turner III, M. C. Downer, A. Babine, A. Stepanov, and A. M. Sergeev, J. Opt. Soc. Am. B **13**, 330 (1996).

[14] J. K. Koga, N. Naumova, M. Kando, L. N. Tsintsadze, K. Nakajima, S. V. Bulanov, H. Dewa, H. Kotaki, and T. Tajima, Phys. Plasmas **7**, 5223 (2000).

[15] P. Sprangle, E. Esarey, and A. Ting, Phys. Rev. A **41**, 4463 (1990).

[16] A. L'Huillier, P. Balcou, S. Candel, K. J. Schafer, and K. C. Kulander, Phys. Rev. A **46**, 2778 (1992).

[17] J. J. Macklin, J. D. Kmetec, and C. L. Gordon III, Phy. Rev. Lett. **70**, 766 (1996).

[18] J. D. Kmetec, and C. L. Gordon III, J. J. Macklin, B. E. Lemoff, G. S. Brown, and S. E. Harris, Phy. Rev. Lett. **68**, 1527 (1992).

[19] Z. Jiang, J. C. Kieffer, J. P. Matte, M. Chaker, O. Peyrusse, D. Gilles, G. Korn, A. Maksimchuk, S. Coe, and G. Mourou, Phys. Plasmas **2**, 1702 (1995).

[20] J. Workman, A. Maksimchuk, X. Liu, U. Ellenberger, J. S. Coe, C.-Y. Chien, and D. Umstadter, Phys. Rev. Lett. **75**, 2324 (1995).

[21] S. J. Moon and D. C. Eder, Phys. Rev. A **57**, 1391 (1998).

[22] P. Amendt, D. C. Eder, and S. C. Wilks, Phys. Rev. Lett. **66**, 2589 (1991).

[23] Y. Nagata, K. Midorikawa, S. Kubodera, M. Obara, H. Tashiro, and K. Toyoda, Phys. Rev. Lett. **71**, 3774 (1993).

[24] B. E. Lemoff, G. Y. Yin, C. L. Gordon III, C. P. J. Barty, and S. E. Harris, Phys. Rev. Lett. **74**, 1574 (1995).

[25] T. Tajima and J. M. Dawson, Phy. Rev. Lett. **43**, 267 (1979).

[26] K. Nakajima, D. Fisher, T. Kawakubo, H. Nakanishi, A. Ogata, Y. Kato, Y. Kitagawa, R. Kodama, K. Mima, H. Shiraga, K. Suzuki, K. Yamakawa, T. Zhang, Y. Sakawa, T. Shoji, Y. Nishida, N. Yugami, M. Downer, and T. Tajima, Phy. Rev. Lett. **74**, 4428 (1995).

[27] D. Umstadter, S. -Y. Chen, A. Maksimchuk, G. Mourou, and R. Wanger, Science **273**, 472 (1996).

[28] D. Gordon, K. C. Tzeng, C. E. Clayton, A. E. Dangor, V. Malka, K. A. Marsh, A. Modena, W. B. Mori, P. Muggli, Z. Najmudin, D. Neely, C. Danson, and C. Joshi, Phy. Rev. Lett. **80**, 2133 (1998).

[29] A. Modena, Z. Najmudin, A. E. Dangor, C. E. Clayton, K. A. Marsh C. Joshi, V. Malka, C. B. Darrow, and C. Danson, IEEE Trans. Plasma Sci., **24**, 289 (1996).

[30] C. I. Moore, A. Ting, K. Krushelnick, E. Esarey, R. F. Hubbard, B. Hafizi, H. R. Burris, C. Manka, and P. Sprangle, Phy. Rev. Lett. **79**, 3909 (1997).

[31] K. Nakajima, Nucl. Instr. and Meth. in Phys. Res. **A410**, 514 (1998).

[32] T. E. Cowan, A. W. Hunt, T. W. Phillips, S. C. Wilks, M. D. Perry, C. Brown, W. Fountain, S. Hatchett, J. Johnson, M. H. Key, T. Parnell, D. M. Pennington, R. A. Snavely, and Y. Takahashi, Phy. Rev. Lett **84**, 903 (2000).

[33] M. Kando, H. Ahn, H. Dewa, H. Kotaki, T. Ueda, M. Uesaka, T. Watanabe, H. Nakanishi, A. Ogata and K. Nakajima, Jpn. J. Appl. Phys. **38**, 967 (1999); H. Dewa, H. Ahn, H. Harano, M. Kando, K. Kinoshita, S. Kondoh, H. Kotaki, K. Nakajima, H. Nakanishi, A. Ogata, H. Sakai, M. Uesaka, T. Ueda, T. Watanabe, K. Yoshii, Nucl. Instr. and Meth. in Phys. Res. A **410**, 357 (1998).

[34] K. Nakajima, Nucl. Instr. and Meth. in Phys. Res. **A455**, 140 (2000).

[35] S. Bulanov, N. Naumova, F. Pegoraro, and J. Sakai, Phys. Rev. E **58**, R5257 (1998).

[36] D. Umstadter, J. K. Kim, and E. Dodd, Phy. Rev. Lett. **76**, 2073 (1996).

[37] E. Esarey, R. F. Hubbard, W. P. Leemans, A. Ting, and P. Sprangle, Phy. Rev. Lett. **79**, 2682 (1997).

[38] C. B. Schroeder, P. B. Lee, J. S. Wurtela, E. Esarey, and W. P. Leemans, Phy. Rev. E **59**, 6037 (1999).

[39] S. Semushin, and V. Malka, Rev. Sci. Instrum. **72**, 2961 (2001).

[40] Y. Fukui, V. Kumar, W. Craddock, and P. Bolton, SLAC E150 Plasma Lens Note 99-03, May (1999).

[41] J. G. Pronko, D. Kohler, I. V. Chapman, T. T. Bardin, P. C. Filbert, and J. D. Hawley, Rev. Sci. Instrum. **64**, 1744 (1993).

[42] O. Abraham, J. H. Binn, B. G. DeBoer, and G. D. Stein, Phys. Fluids **24**, 1017 (1981).

[43] E. Tokunaga, A. Terasaki, and T. Kobayashi, Opt. Lett. **17**, 1131 (1992).

[44] C. W. Siders, S. P. Le Blanc, D. Fisher, T. Tajima, and M. C. Downer, Phys. Rev. Lett. **76**,3570 (1996); C. W. Siders, S. P. Le Blanc, A. Babine, A. Stepanov, A. Sergeev, T. Tajima, and M. C. Downer, IEEE Trans. Plasma Sci. **24**, 301 (1996).

[45] J. R. Marquès, J. P. Geindre, F. Amiranoff, P. Audebert, J. C. Gauthier, A. Antonetti, and G. Grillon, Phys. Rev. Lett. **76**,3566 (1996); J. R. Marquès, F. Dorchies, P. Audebert, J. P. Geindre, F. Amiranoff, J. C. Gauthier, G. Hammoniaux, A. Antonetti, P. Chessa, P. Mori, and T. M. Antonsen Jr., Phys. Rev. Lett. **78**,3463 (1997); J. R. Marquès, F. Dorchies, F. Amiranoff, P. Audebert, J. C. Gauthier, J. P. Geindre, A. Antonetti, T. M. Antonsen Jr., P. Chessa, and P. Mori, Phys. Plasmas **5**, 1162 (1998).

[46] E. Takahashi, H. Honda, E. Miura, N. Yugami, Y. Nishida, and K. Kondo, J. Phys. Soc. Jpn. **69**, 3266 (2000); E. Takahashi, H. Honda, E. Miura, N. Yugami, Y. Nishida, K. Katsura, and K. Kondo, Phys. Rev. E **62**, 7247 (2000).

[47] H. Kotaki, M. Kando, T. Oketa, S. Masuda, J. K. Koga, S. Kondo, S. Kanazawa, T. Yokoyama, T. Matoba, and K. Nakajima, Phys. Plasmas **9**, 1392 (2002).

[48] P. Agostini, F. Fabre, G. Mainfray, G. Petite, and N. K. Rahman, Phys. Rev. Lett. **42**, 1127 (1979).

[49] S. Augst, D. Strickland, D. D. Meyerhofer, S. L. Chin, and J. H. Eberly, Phys. Rev. Lett. **63**, 2212 (1989).

[50] X. F. Li, A. L'Huillier, M. Ferray, L. A. Lompré, and G. Mainfray, Phys. Rev. A **39**, 5751 (1989).

[51] Y. Shimoji, A. T. Fay, R. S. F. Chang, and N. Djeu, J. Opt. Soc. Am. **6**, 1994 (1989).

[52] V. I. Bespalov and V. I. Talanov, JETP Lett. **3**, 471 (1966).

[53] R. W. Boyd, *NonlinearOptics* (Academic, San Diego, 1992).

[54] N. C. Kothari and T. Kobayashi, Phys. Rev. Lett. **50**, 160 (1983).

[55] M. Mlejnek, M. Kolesik, J. V. Moloney, and E. M. Wright, Phys. Rev. Lett. **83**, 2938 (1999).

[56] R. Rankin, C. E. Capjack, N. H. Burnett, and P. B. Corkum, Opt. Lett. **16**, 835 (1991).

[57] M. Kando, The doctoral dissertation, Kyoto University, Chapter 5.4 (1998)

[58] S. Masuda, T. Katsouleas, and A. Ogata, Nucl. Inst. and Meth. A **455**, 172 (2000)

[59] E. Esarey and M. Pilloff, Phys. Plasmas **2**, 1432 (1995).

[60] A. I. Akheizer and R. V. Polovin, Sov. Phys. JETP **3**, 696 (1956).

[61] X. J. Wang, M. Babzien, K. Batchelor, I. Ben-Zvi, R. Malone, I. Pogorelsky, X. Qui, J. Sheehan, J. Sharitka, and T. Srinivasan-Rao, Nucl. Instr. and Meth. A **375** (1996) 82; X. J. Wang, X. Qiu, and I. Ben-Zvi, Phys. Rev. E **54**, 3121 (1996).

Appendix A Thomson Scattering

If a plane wave $\mathbf{E}(\mathbf{x},t)$ is incident on a free particle of charge e and mass m, the particle will be accelerated. The acceleration is provided by the incident plane wave. If its propagation vector $\mathbf{k}_0$, and its polarization vector $\boldsymbol{\epsilon}_0$, the electric field can be written

$$\mathbf{E}(\mathbf{x},t) = \boldsymbol{\epsilon}_0 E_0 \exp(i\mathbf{k}_0\mathbf{x} - i\omega t). \tag{A.1}$$

Then, from the force equation for nonrelativistic motion, we have the acceleration,

$$\dot{\mathbf{v}}(t) = \boldsymbol{\epsilon}_0 \frac{e}{m} E_0 \exp(i\mathbf{k}_0\mathbf{x} - i\omega t). \tag{A.2}$$

The differential scattering cross section is[1]

$$\frac{d\sigma}{d\Omega} = \left(\frac{e^2}{mc^2}\right)^2 |\boldsymbol{\epsilon}^* \cdot \boldsymbol{\epsilon}_0|^2, \tag{A.3}$$

where $\boldsymbol{\epsilon}$ is a polarization state. The scattering geometry with a choice of polarization vectors for the outgoing wave is shown in Fig. A.1. The polarization vector $\boldsymbol{\epsilon}_1$ is in the plane containing $\mathbf{n}$ and $\mathbf{k}_0$; $\boldsymbol{\epsilon}_2$ is perpendicular to it. In terms of unit vectors parallel to the coordinate axes, $\boldsymbol{\epsilon}_1$ and $\boldsymbol{\epsilon}_2$ are

$$\boldsymbol{\epsilon}_1 = \cos\theta(\mathbf{e}_x \cos\phi + \mathbf{e}_y \sin\phi) - \mathbf{e}_z \sin\theta, \tag{A.4}$$

$$\boldsymbol{\epsilon}_2 = -\mathbf{e}_x \sin\phi + \mathbf{e}_y \cos\phi. \tag{A.5}$$

For a linearly polarized wave with polarization parallel to the x axis incident, the angular distribution summed over final polarization is $(\cos^2\theta\cos^2\phi + \sin^2\phi)$, and the scattering cross section is rewritten

$$\left|\frac{d\sigma}{d\Omega}\right|_{\epsilon_0 \| x} = \left(\frac{e^2}{mc^2}\right)^2 (\cos^2\theta\cos^2\phi + \sin^2\phi). \tag{A.6}$$

When the direction $\mathbf{n}$ is parallel to the x axis, the scattering cross section becomes zero. For polarization parallel to the y axis it is

$$\left|\frac{d\sigma}{d\Omega}\right|_{\epsilon_0 \| y} = \left(\frac{e^2}{mc^2}\right)^2 (\cos^2\theta\sin^2\phi + \cos^2\phi). \tag{A.7}$$

For unpolarized incident radiation we can obtain the scattering cross section by integrating Eqs. (A.6) or (A.7) as a function of ϕ

$$\frac{d\sigma}{d\Omega} = \left(\frac{e^2}{mc^2}\right)^2 \frac{1+\cos^2\theta}{2}. \tag{A.8}$$

The total scattering cross section, Thomson cross section, is

$$\sigma_T = \frac{8\pi}{3}\left(\frac{e^2}{mc^2}\right)^2. \tag{A.9}$$

The Thomson cross section is equal to 0.665×10^{-24} cm^2 for electrons. The unit of length, $e^2/mc^2 = 2.82\times10^{-13}$ cm, is called the *classical electron radius*, since a classical distribution of charge totaling the electron charge must have a radius of this order if its electrostatic self-energy is to equal the electron mass.

[1] J. D. Jackson, *ClassicalElectrodynamics* (John Wiley & Sons, Inc., New York, 1962).

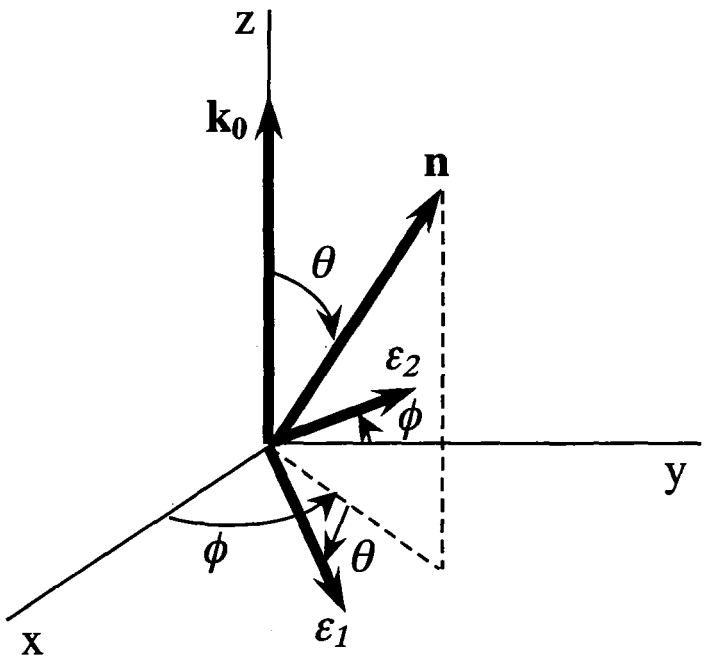

Figure A.1: The scattering geometry. The polarization vector ϵ_1 is in the plane containing $\mathbf{n}$ and $\mathbf{k}_0$, and ϵ_2 is perpendicular to it.

Appendix B Particle-in-Cell Simulation

B.1 Basic Equation

We solve Maxwell's equations for the electric field $\mathbf{E} \equiv (E_x, E_y, E_z)$ and the magnetic field $\mathbf{B} \equiv (B_x, B_y, B_z)$

$$\nabla \times B = \mu_0 \mathbf{J} + \frac{1}{c^2}\frac{\partial \mathbf{E}}{\partial t}, \tag{B.1}$$

$$\nabla \times E = -\frac{\partial \mathbf{B}}{\partial t}, \tag{B.2}$$

where $\mathbf{J} \equiv (J_x, J_y, J_z)$, c and μ_0 are the current density, the speed of light and the magnetic permeability, respectively. We assume a one-dimensional system taken along the x-axis. The electric field E_x should satisfy the initial condition given by Poisson's equation

$$\frac{\partial E_x}{\partial x} = \frac{\rho}{\epsilon_0}, \tag{B.3}$$

where ρ and ϵ_0 are the charge density and the electric permittivity, respectively. It is noted that Poisson's equation is solved only for the initial condition. It is satisfied automatically, if Eq. (B.1) is solved correctly in time based on the current density $\mathbf{J}$ satisfying the continuity equation of the charge density ρ. The magnetic field B_x should satisfy the initial condition given by

$$\frac{\partial B_x}{\partial x} = 0. \tag{B.4}$$

This condition means that B_x is constant in space and time, because there is no term for B_x in Eqs. (B.1) and (B.2).

The current density $\mathbf{J}$ and the charge density ρ are computed from the motion of a large number of particles. The equations of motion for particles with a charge q and a mass m is

$$\frac{dv}{dt} = \frac{q}{m}(\mathbf{E} + \mathbf{v} \times \mathbf{B}), \tag{B.5}$$

$$\frac{dx}{dt} = v_x, \tag{B.6}$$

The basic equations described above are written in the form of the MKS unit system. In a simulation, however, values of the permittivity ϵ_0 and permeability μ_0 can be defined arbitrarity, as far as they satisfy the relation

$$\epsilon_0 \mu_0 = \frac{1}{c^2}. \tag{B.7}$$

For simplicity, we adopt the following definition

$$\epsilon_0 = 1, \tag{B.8}$$

$$\mu_0 = \frac{1}{c^2}. \tag{B.9}$$

The $\mathbf{E}$, $\mathbf{B}$ and $\mathbf{J}$ are defined at the spatial grid points, while particles can take arbitrary positions. The $\mathbf{E}$ and $\mathbf{B}$ in Eq. (B.5) are interpolated from those at the adjacent grid points.

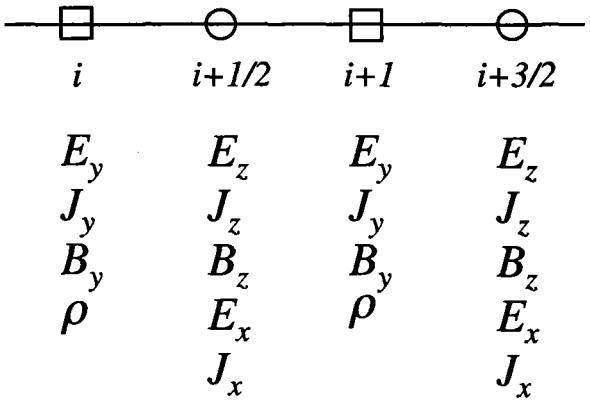

Figure B.1: Grid assignment.

B.2 Grid Assignment

We define full-integer grids at $i\Delta x$ ($i = 1, 2, 3, ..., N_x$) and half-integer grids at $(i + 1/2)\Delta x$. The E_y, B_y, J_y and ρ are defined at the full-integer grids, and E_x, E_z, B_z, J_x, J_z at the half-integer grids as shown in Fig. B.1. This assignment of the electric and magnetic fields **E** and **B** realizes centered difference forms for the spatial derivatives in Maxwell's equations. The components J_x, J_y. J_z of the current density must be assigned to the same grids of E_x, E_y, E_z, respectively, because **J** contributes directly to the time integration of **E** as in Eq. (B.1).

B.3 Time Step Chart

The quantities of the field and particles are advanced in time based on the sequence shown in Fig. B.2. We define a full-integer time $n\Delta t$ and a half-integer time $(n+1/2)\Delta t$ with a time step Δt. Basically, the electric field **E** at the full-integer time and the magnetic field **B** at the half-integer time are integrated in time by the leap-frog method. However, the magnetic field **B** is advanced twice by a half time step $\Delta t/2$ to obtain intermediate values for the particle pushing fields at the full-integer time. The particle positions x at the full-integer time and velocities v at the half-integer time are also advanced by the leap-frog method. The positions are advanced twice with a half time step $\Delta t/2$ to obtain intermediate values for computation of the current density **J** at the half-integer time. The current density **J** is computed from the positions and velocities of particles.

B.4 Courant Condition

In solving Maxwell's equations by the centered difference scheme in space and by the leap-frog method in time, the grid spacing Δx and the time step Δt should satisfy the following inequality, which is called the Courant condition,

$$\Delta x > c\Delta t. \tag{B.10}$$

The condition easily derived from the numerical dispersion relation of the light more. Let us see the numerical effect in solving a differential equation by a centered-difference equation. We assume a quantity $A(x,t)$ has a wave structure with a wavenumber k and a frequency ω as

$$A(x,t) = A_0 \exp(ikx - i\omega t). \tag{B.11}$$

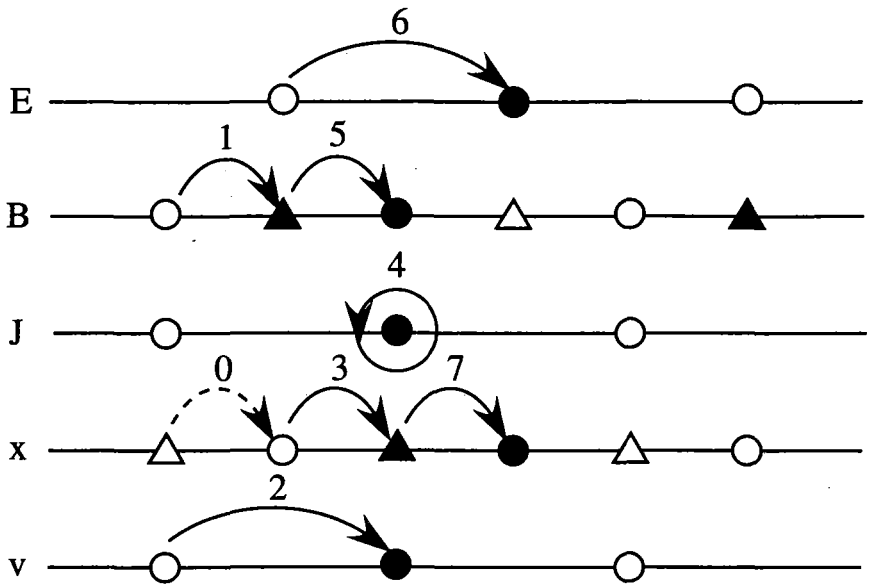

Figure B.2: Time step chart.

We compute the derivative by a centered-difference equation as

$$\begin{aligned}\frac{\delta A}{\delta x} &= \frac{A(x_0+\Delta x/2,t)-A(x_0-\Delta x/2,t)}{\Delta x} \\ &= \frac{\exp(ik\Delta x/2)-\exp(-ik\Delta x/2)}{\Delta x}A(x_0,t) \\ &= i\frac{\sin(k\Delta x/2)}{\Delta x/2}A(x_0,t). \end{aligned} \tag{B.12}$$

Comparing the $\Delta A/\Delta x$ withe the spatial derivative $\partial A/\partial x$, we find that the wavenumber k is replaced by K represented by

$$K = \frac{\sin(k\Delta x/2)}{\Delta x/2}, \tag{B.13}$$

in converting the differential equations to the difference equation. In the same manner, we find that the frequency ω is replaced by Ω defined as

$$\Omega = \frac{\sin(\omega\Delta t/2)}{\Delta t/2}. \tag{B.14}$$

The dispersion relation of the light mode is obtained by neglecting the current density $\mathbf{J}$ and assuming the electromagnetic wave with a frequency ω and the wavenumber k as

$$\omega^2 = c^2k^2. \tag{B.15}$$

Replacing k and ω with $K$and Ω, we have the numerical dispersion relation for the light wave

$$\Omega^2 = c^2K^2. \tag{B.16}$$

For the maximum wavenumber $k_{max} = \pi/\Delta x$, we have

$$\sin^2(\omega\Delta t) = \left(\frac{c\Delta t}{\Delta x}\right)^2. \tag{B.17}$$

If $c\Delta t/\Delta x > 1$, the ω becomes complex, given rise to a numerical instability. If $c\Delta t/\Delta x > 1$, then the system is marginally stable. Therefore, we have the Courant condition.

国際単位系 (SI) と換算表

表 1　SI基本単位および補助単位

量	名称	記号
長さ	メートル	m
質量	キログラム	kg
時間	秒	s
電流	アンペア	A
熱力学温度	ケルビン	K
物質量	モル	mol
光度	カンデラ	cd
平面角	ラジアン	rad
立体角	ステラジアン	sr

表 2　SIと併用される単位

名称	記号
分，時，日	min，h，d
度，分，秒	°，′，″
リットル	l，L
トン	t
電子ボルト	eV
原子質量単位	u

1 eV = 1.60218 × 10^{-19} J

1 u = 1.66054 × 10^{-27} kg

表 5　SI接頭語

倍数	接頭語	記号
10^{18}	エクサ	E
10^{15}	ペタ	P
10^{12}	テラ	T
10^{9}	ギガ	G
10^{6}	メガ	M
10^{3}	キロ	k
10^{2}	ヘクト	h
10^{1}	デカ	da
10^{-1}	デシ	d
10^{-2}	センチ	c
10^{-3}	ミリ	m
10^{-6}	マイクロ	μ
10^{-9}	ナノ	n
10^{-12}	ピコ	p
10^{-15}	フェムト	f
10^{-18}	アト	a

表 3　固有の名称をもつSI組立単位

量	名称	記号	他のSI単位による表現
周波数	ヘルツ	Hz	s^{-1}
力	ニュートン	N	$m \cdot kg/s^2$
圧力，応力	パスカル	Pa	N/m^2
エネルギー，仕事，熱量	ジュール	J	N·m
工率，放射束	ワット	W	J/s
電気量，電荷	クーロン	C	A·s
電位，電圧，起電力	ボルト	V	W/A
静電容量	ファラド	F	C/V
電気抵抗	オーム	Ω	V/A
コンダクタンス	ジーメンス	S	A/V
磁束	ウェーバ	Wb	V·s
磁束密度	テスラ	T	Wb/m^2
インダクタンス	ヘンリー	H	Wb/A
セルシウス温度	セルシウス度	℃	
光束	ルーメン	lm	cd·sr
照度	ルクス	lx	lm/m^2
放射能	ベクレル	Bq	s^{-1}
吸収線量	グレイ	Gy	J/kg
線量当量	シーベルト	Sv	J/kg

表 4　SIと共に暫定的に維持される単位

名称	記号
オングストローム	Å
バーン	b
バール	bar
ガル	Gal
キュリー	Ci
レントゲン	R
ラド	rad
レム	rem

1 Å = 0.1 nm = 10^{-10} m

1 b = 100 fm^2 = 10^{-28} m^2

1 bar = 0.1 MPa = 10^5 Pa

1 Gal = 1 cm/s^2 = 10^{-2} m/s^2

1 Ci = 3.7 × 10^{10} Bq

1 R = 2.58 × 10^{-4} C/kg

1 rad = 1 cGy = 10^{-2} Gy

1 rem = 1 cSv = 10^{-2} Sv

（注）

1. 表1－5は「国際単位系」第5版，国際度量衡局 1985年刊行による。ただし，1 eVおよび1 uの値はCODATAの1986年推奨値によった。
2. 表4には海里，ノット，アール，ヘクタールも含まれているが日常の単位なのでここでは省略した。
3. barは，JISでは流体の圧力を表わす場合に限り表2のカテゴリーに分類されている。
4. EC閣僚理事会指令ではbar，barnおよび「血圧の単位」mmHgを表2のカテゴリーに入れている。

換算表

力	N(=10^5dyn)	kgf	lbf
	1	0.101972	0.224809
	9.80665	1	2.20462
	4.44822	0.453592	1

粘度　1 Pa·s(N·s/m^2) = 10 P(ポアズ)(g/(cm·s))

動粘度　1 m^2/s = 10^4 St(ストークス)(cm^2/s)

圧力	MPa(=10 bar)	kgf/cm^2	atm	mmHg(Torr)	lbf/in^2(psi)
	1	10.1972	9.86923	7.50062 × 10^3	145.038
	0.0980665	1	0.967841	735.559	14.2233
	0.101325	1.03323	1	760	14.6959
	1.33322 × 10^{-4}	1.35951 × 10^{-3}	1.31579 × 10^{-3}	1	1.93368 × 10^{-2}
	6.89476 × 10^{-3}	7.03070 × 10^{-2}	6.80460 × 10^{-2}	51.7149	1

エネルギー・仕事・熱量	J(=10^7 erg)	kgf·m	kW·h	cal(計量法)	Btu	ft·lbf	eV
	1	0.101972	2.77778 × 10^{-7}	0.238889	9.47813 × 10^{-4}	0.737562	6.24150 × 10^{18}
	9.80665	1	2.72407 × 10^{-6}	2.34270	9.29487 × 10^{-3}	7.23301	6.12082 × 10^{19}
	3.6 × 10^6	3.67098 × 10^5	1	8.59999 × 10^5	3412.13	2.65522 × 10^6	2.24694 × 10^{25}
	4.18605	0.426858	1.16279 × 10^{-6}	1	3.96759 × 10^{-3}	3.08747	2.61272 × 10^{19}
	1055.06	107.586	2.93072 × 10^{-4}	252.042	1	778.172	6.58515 × 10^{21}
	1.35582	0.138255	3.76616 × 10^{-7}	0.323890	1.28506 × 10^{-3}	1	8.46233 × 10^{18}
	1.60218 × 10^{-19}	1.63377 × 10^{-20}	4.45050 × 10^{-26}	3.82743 × 10^{-20}	1.51857 × 10^{-22}	1.18171 × 10^{-19}	1

1 cal = 4.18605 J（計量法）

= 4.184 J　（熱化学）

= 4.1855 J　（15 °C）

= 4.1868 J（国際蒸気表）

仕事率　1 PS（仏馬力）

= 75 kgf·m/s

= 735.499 W

放射能	Bq	Ci
	1	2.70270 × 10^{-11}
	3.7 × 10^{10}	1

吸収線量	Gy	rad
	1	100
	0.01	1

照射線量	C/kg	R
	1	3876
	2.58 × 10^{-4}	1

線量当量	Sv	rem
	1	100
	0.01	1

（86年12月26日現在）

Study of Ultra-high Gradient Wakefield Excitation by Intense Ultrashort Laser Pulses in Plasma